Title
Design, Fabrication, and Evaluation of Superhydrophobic (SHPo) Surfaces for Drag Reduction in Turbulent Boundary Layer Flows

Author
Xu, Muchen

Publication Date
2016

Peer reviewed|Thesis/dissertation

UNIVERSITY OF CALIFORNIA

Los Angeles

Design, Fabrication, and Evaluation of Superhydrophobic (SHPo) Surfaces for Drag Reduction in Turbulent Boundary Layer Flows

A dissertation submitted in partial satisfaction of the

requirements for the degree Doctor of Philosophy

in Mechanical Engineering

by

Muchen Xu

2017

ABSTRACT OF THE DISSERTATION

Design, Fabrication, and Evaluation of Superhydrophobic (SHPo) Surfaces

for Drag Reduction in Turbulent Boundary Layer Flows

by

Muchen Xu

Doctor of Philosophy in Mechanical Engineering

University of California, Los Angeles, 2017

Professor Chang-Jin Kim, Chair

Sustaining a gas layer on them in liquid, superhydrophobic (SHPo) surfaces have attracted enormous attention due to the possibility of reducing friction drag in numerous flow applications. Although many SHPo surfaces proved to reduce drag significantly (e.g., > 10%) in microchannel flows and certain SHPo surfaces proved to have an unprecedentedly large slip length (e.g., > 100 microns), a significant drag reduction is still elusive in turbulent flows that reflect most applications, such as watercraft in marine environment. Recognizing the gas layer (called plastron) as the key and studying its robustness under water of varying depths, we first conclude that the SHPo surfaces capable of a significant drag reduction cannot maintain the plastron indefinitely if submerged deeper than a few centimeters. By developing a high-resolution shear sensor for

centimeters-size sample surfaces and using silicon SHPo surfaces that keep plastron more robust than others, we obtain up to ~25% drag reduction in turbulent boundary layer flows at Reynolds numbers up to $1.1x10^7$. Obtained at a high-speed water tunnel and a high-speed tow tank, the results also indicate that the drag reduces more with increasing Reynolds number, corroborating the numerical studies in the literature. Moreover, we develop and conduct SHPo drag experiments using a real boat in marine conditions for the first time, achieving ~20% drag reduction. Finally, a scalable fabrication process is developed for scale-up manufacturing of both passive and semi-active SHPo surfaces. For the semi-active SHPo surfaces, i.e., SHPo surfaces with self-regulating gas restoration capability, we propose and demonstrate a gas generation mechanism that does not require any external power input.

The dissertation of Muchen Xu is approved.

J. John Kim

Laurent G. Pilon

Jenn-Ming Yang

Chang-Jin Kim, Committee Chair

University of California, Los Angeles

2017

Dedicated to my family and the memory of my grandmother

For their unconditional love

TABLE OF CONTENTS

LIST OF FIGURES

LIST OF TABLES

ACKNOWLEDGEMENT

First and foremost, I would like to express my deepest gratitude to Prof. Chang-Jin “CJ” Kim, my Ph.D. advisor, for his guidance, patience and encouragement throughout my Ph.D. journey. He saw my potential at the very beginning and brought out the best in me throughout these years. As a researcher, he has always been inspiring me with his passion, curiosity and critical thinking. Extending forefront of human knowledge and developing products with impact in real world, it has been enjoyable doing research with him.

I would like to extend my appreciation to Prof. John Kim who provided professional insights and answered numerous fluid mechanics questions throughout my Ph.D. study I am also sincerely grateful to Prof. Laurent Pilon for his valuable comments and keen advice for my research. I would like to thank Prof. Jenn-Ming Yang for his kindness to be on my committee and his suggestions on my work. I am deeply indebted to UCLA-CSST program and Prof. Ren Sun for bringing me to UCLA for 2010 summer research program.

I wouldn`t have finished the flow test experiments without the kind support of people from different institutions across the country. I am truly thankful to Prof. Chang-Hwan Choi at Stevens Institute of Technology for his suggestions and insights that helped me find light in the difficulties. I would like to thank Mr. Michael DeLorme, Mr. Uihoon Chung, Dr. Dong Song and other staff at Davidson Lab at Stevens Institute of Technology for all their help during the towing tank test. My gratitude also goes to Prof. Michael Schultz and Dr. Julio Barros for their kind assistance in the water tunnel test at United States Naval Academy. I really appreciate the help from Mr. Byron Pfeifer, Mr. Erinn McMahan and UCLA Aquatic Center for making the boat test possible. I thank the staff at UCLA Nanolab who provided me assistance for micro-fabrication.

I would also like to acknowledge my colleagues at UCLA for valuable advices, kind assistance and productive discussion along the journey. I am indebted to Prof. Guangyi Sun and Dr. Tingyi Liu who taught me how to do research from the beginning and helped me on all kinds of issues in both research and life. I thank Dr. Supin Chen, Mr. James Jenkins, Ms. Coco Huang, Dr. Janet Hur, Dr. Wook Choi, Prof. Hyungmin Park and Dr. Hyunwook Park for their help in research and everyday life. I thank Dr. Ke Ding, Dr. Ying Li and Dr. Wei-Yang Sun for our study times and fruitful discussion in the first year. I really enjoy working with Mr. Jia Li, Ms. Gintare Kerezyte, Ms. Jeong-Won Lee, Mr. Ryan Freeman, Mr. Ning Yu, Mr. Qi Wu, Prof. Hao Tong and Prof. Jiangzhong Qiu, naming just a few.

I am eternally grateful to my dear friends Mr. Yajia Yang and Ms. Qibei Wu for all these years we spent together and all the kind supports from them: they have always been the first ones I called when I was in trouble. I would also like to appreciate all my friends who I shared great time with and support me in these years: Mr. Hao Wu, Mr. Yao Wang, Dr. Fan Xiao, naming just a few.

I owe my sincere and eternal thankfulness for my family and their unconditional love. Words cannot express the gratitude I have for my world`s greatest parents who love me more than anything else. My earnest thankfulness goes to my parents-in-law who love and support me like their own. I also dedicate this dissertation to the memory of my grandmother whose role has been and will always be immense in my life. Finally, and most importantly, I would like to thank my wife and my best friend Yuting. Her unwavering love and support have been and will always be the bedrock of my life. Being with her, every moment is joyful.

VITA

2011	B.S. Mechanical Engineering (1st in class) Xi`an Jiaotong University, Xi`an, China
2013	M.S. Mechanical Engineering University of California, Los Angeles, USA
2011-2017	Graduate Student Researcher Teaching Associate Mechanical and Aerospace Engineering Department University of California, Los Angeles, USA

PATENTS

M. Xu and C.-J. Kim, "Device and Method for Gas Maintenance in Microstructures on a Submerged Surface," International Patent WO/2016/011271, 2015.

M. Xu and C.-J. Kim, "Method for manufacturing re-entrant microstructures," International Patent WO/2016/122959, 2016.

C.-J. Kim and M. Xu, "A low-profile flow shear sensing unit," United States Provisional Patent No. 62/258,344, 2016.

PUBLICATIONS AND PRESENTATIONS

M. Xu, G. Sun, and C.-J. Kim, "Infinite Lifetime of Underwater Superhydrophobic States," *Physical Review Letters*, vol. 113, 136103, 2014.

M. Xu, G. Sun, and C.-J. Kim, "Wetting dynamics study of underwater superhydrophobic surfaces through direct meniscus visualization," *Proceedings of the IEEE International Conference on Micro Electro Mechanical Systems*, January 2014, San Francisco, CA, pp. 668-671.

M. Xu and C.-J. Kim, "Longevity of underwater superhydrophobic surfaces for drag reduction," *Bulletin of the American Physical Society*, Vol. 59, No. 20, Abstract ID: BAPS.2014.DFD.H8.1; *67th Annual Meeting of the APS Division of Fluid Dynamics*, San Francisco, CA, November 2014.

M. Xu and C.-J. Kim, "High-resolution compact shear stress sensor for direct measurement of skin friction in fluid flow," *Bulletin of the American Physical Society*, Vol. 60, No. 21, Abstract ID: BAPS.2015.DFD.E26.2; *68th Annual Meeting of the APS Division of Fluid Dynamics*, Boston, MA, November 2015.

Chapter 1 Introduction

1.1 Backgrounds

Mother nature has always been the greatest magician showing numerous "magic" phenomena, inspiring human beings to uncover the "tricks". When people saw water rolling off the lotus leaf effortlessly [1], diving bell spider living completely submerged for their whole lives [2], and water striders strolling on the water surface like on the ground [3], they started to wonder what are the "tricks" behind all these magics. The mechanisms behind these amazing natural "magics" have begun to be understood recently, and the one thing behind them is called superhydrophobic (SHPo) surface. It is a masterful way for the nature to manipulate air-water meniscus at small scale so pockets of air could be trapped stably in between solid and liquid. With this air layer, called plastron, all the above magics have come true.

1.1.1 Definition of SHPo Surface

As early as 1805, Thomas Young has defined the contact angle θ (Figure 1-1(a)) of a liquid droplet on a solid surface surrounded by a gas:

$$\gamma_{SG} = \gamma_{SL} + \gamma_{LG}\cos\theta \tag{2-1}$$

where γ_{SG} , γ_{SL} and γ_{LG} are the interfacial tension between the solid and gas, the solid and liquid and the liquid and gas, respectively, determined by materials properties. The Young`s equation is generally used to describe the contact angle on flat surface. When the interfacial tension between solid and liquid decreases (i.e., the liquid "likes" the solid), the contact angle decreases and vice versa. Meanwhile, when a droplet is about to slide off on a tilted surface (Figure 1-1(b)), the titling

angle is defined as roll-off angle α, and the different between advancing contact angle θ_a and receding contact angle θ_r is defined as contact angle hysteresis.

However, when it comes to rough surfaces, Young`s equation cannot be directly applied to calculate the contact angle of the droplet, which is defined as apparent contact angle $\theta_{ap}$, as shown on Figure 1-1(c)(d). But Young`s equation still applies locally at the triple contact point where gas-liquid meniscus meets solid (Figure 1-1(b)). The local contact angle is also known as intrinsic contact angle which is determined by Equation (2-1) (i.e., materials properties). The apparent contact angle is usually different from the intrinsic contact angle, depending on the roughness geometry and materials properties. Superhydrophobic (SHPo) surfaces are conventionally defined as the surfaces where the apparent contact angles of a water droplet on it exceed 150° with roll-off angle or contact angle hysteresis less than 10°. To achieve this high apparent contact angle and low roll-off angle, SHPo surface must be a rough surface that is locally hydrophobic.

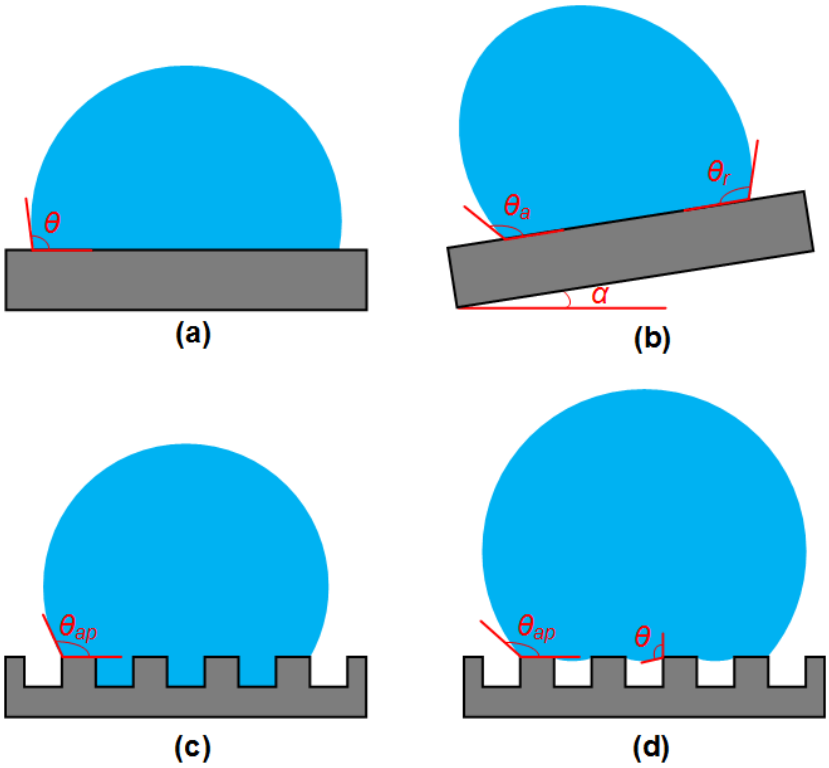

Figure 1-1 Schematics of droplet on different surfaces. (a) Droplet on flat surface with Young`s angle θ. (b) Droplet on a tilted surface with roll-off angle α, advancing contact angle θ_a and receding contact angle θ_r. (c,d) Droplet on rough surfaces with apparent contact angle θ_{ap}.

Two classic models, Wenzel [4] and Cassie [5] model, have systematically studied the apparent contact angle on surfaces with different roughness and surface properties. The Wenzel model (Figure 1-1(c)) describes the case when the roughness is filled with liquid, and the Cassie model (Figure 1-1(d)) describes the case when the roughness is filled with gas.

For Wenzel model, the apparent contact angle is [4]:

$$\cos\theta_{ap,w} = r\cos\theta \tag{2-2}$$

where r is the roughness (actual surface area versus projected surface area). The Wenzel model predicts that the roughness amplifies a surface wettability by making a hydrophilic surface more hydrophilic and hydrophobic surface more hydrophobic.

For Cassie-Baxter model, the apparent contact angle can be described as [5]:

$$\cos\theta_{ap,c} = \Phi_S \cos\theta - (1-\Phi_S) \tag{2-3}$$

where Φ_S is an area fraction of liquid-solid interface. The Cassie-Baxter model predicts that a surface becomes more hydrophobic as the contact area between the liquid and solid (i.e., solid fraction) decreases regardless of the intrinsic contact angle on the surface.

For different surfaces with different roughness dimension and surface property, either Cassie or Wenzel state can be thermodynamically more stable. The critical intrinsic contact angle is [6]:

$$\cos\theta_C = \frac{1-\Phi_S}{r-\Phi_S} \tag{2-4}$$

When the intrinsic contact angle is larger than the critical contact angle, Cassie state is more favorable, and when the intrinsic contact angle is smaller than the critical contact angle, Wenzel state is more favorable. In reality, Cassie and Wenzel state can coexist on the same surface [7], i.e., one state can exist even when the other state is more stable [7] because both of the states can be locally stable with an energy barrier between them. When not disturbed enough to overcome the barrier, the system could stay in the meta-stable state. Assuming the Wenzel state has a lower energy, more stable, than the Cassie state, Figure 1-2 shows the schematic view of Gibbs free energy of the two states along with the impalement configuration [8]. Cassie-to-Wenzel state transition (i.e., wetting transition) is usually caused by pressure [9]. When external pressure

overcomes the supporting force by surface tension on the top of the roughness, wetting transition occurs. On the other hand, Wenzel-to-Cassie state transition (i.e., de-wetting transition) would need external energy input like vibration [10] or electrical current pulse [11].

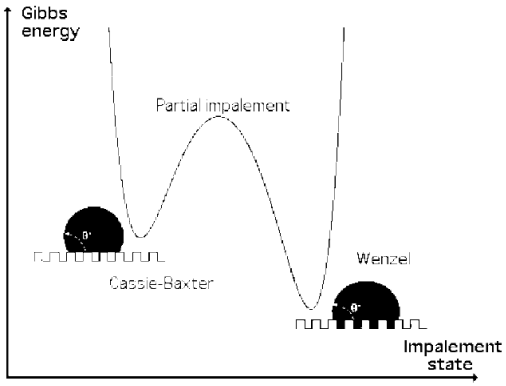

Figure 1-2 Schematic view of the Gibbs free energy of the Cassie-Baxter and Wenzel states. [8]

The superhydrophobicity generally refer to Cassie state in which the gas can be retained and droplet can roll off easily. To use superhydrophobicity, impalement of the liquid into the surface roughness (i.e., wetting transition) should be prevented. However, when the SHPo surface is fully immersed underwater, the wetting transition mechanisms are quite different from droplet on SHPo surface. Firstly, the pressure of the isolated air pockets can change by the pressure of the surrounding liquid. Second, the mass exchange (i.e., diffusion) between the isolated air pockets and the surrounding water should be considered. Third, Wenzel to Cassie state transition is more difficult since gas need to be created in between the roughness. Fourth, vapor pressure of water in the air pocket needs to be considered, too. The wetting dynamics of underwater SHPo surface is studied rigorously in Chapter 2.

1.1.2 Examples of SHPo Surfaces in Nature

Many creatures in nature have utilized the SHPo surfaces much earlier than human did. There are two categories of applications in nature: one is droplets-related application and the other is underwater application. While the first application is mainly for self-cleaning [12] or sliding [3], the second application is usually for underwater breathing based on the air capturing properties of SHPo surface [13, 14].

For the droplets-related application, the most famous example is the so-called “Lotus Effect” of lotus leaves, where water droplets can roll off the leaves and pick dirty particles with them. As shown in the scanning electron microscopy (SEM) picture in Figure 1-3(a) [12], microscale bumps are covered with microepicuticular wax crystalloids on a lotus leaf. Since the wax is hydrophobic, the water droplets only contact the top tip of all these bump, greatly reducing solid-liquid contacting area and adhesion. This SHPo surface structure leads to the water-repellent and self-cleaning property of the lotus leaves. A liquid drop only redistributes dirt particles while it slides down a surface on a smooth surface, while a liquid drop picks up dirt particles and removes them while it rolls off the surface on a SHPo surface [12]. Evolution of such features is advantageous to the lotus especially because it usually grows in an environment close to water and mud. Dryness and cleanness of a lotus leaf is desirable for the gas exchange needed for photosynthesis and protection against pathogen attack.

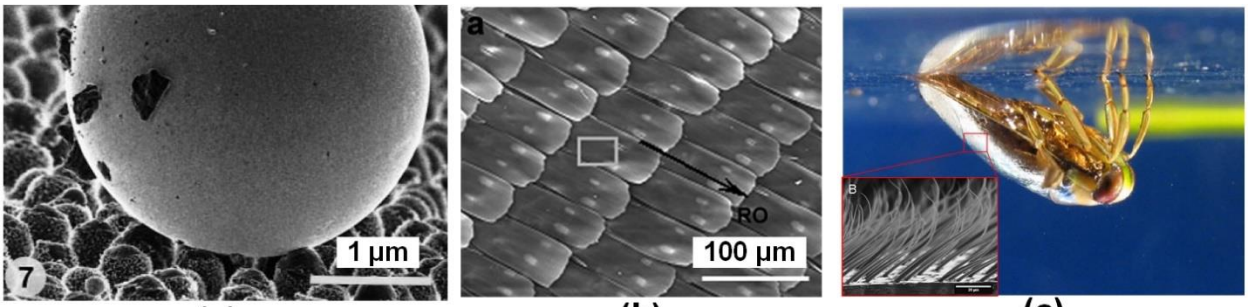

(a) (b) (c)

Figure 1-3 Examples of SHPo surface in nature. (a) Mercury droplet on Lotus leaf [12]. (b) Wings of butterfly [15]. (c) Backswimmer with microscale hair on its back [16].

Most SHPo surfaces in nature are for droplet-related applications with the gas retained on the SHPo surface connected to atmosphere, like the wing of butterfly [15] (Figure 1-3(b)). There are some, although rare, natural applications of underwater SHPo surfaces [2, 13, 14, 17, 18]. For example, the family of backswimmers *Notonectidae* are able to exchange oxygen between their hemoglobin and plastron to breath [13, 14] with the help of micro/nano hairs on its back (Figure 1-3(c)). The aquatic spider Argyroneta aquatica can carry air to a "diving bell" consisting of a 1-3 mL air bubble enmeshed within a tightly woven web [18]. Penguins dive to ocean depths with air bubbles trapped between their feathers to reduce drag [17]. However, since the air trapped in SHPo surface are metastable [19] and tends to diffuse into water at high immersion depth [20], most of the underwater SHPo surfaces in nature live at very shallow water [13, 14, 18] or for short time [17]. For more details regarding different natural SHPo surfaces, please refer to recent review papers [21, 22].

1.2 SHPo Surfaces for Drag Reduction

Friction is often undesirable in applications related to flow. It contributes to 60-70% of the total drag on a cargo ship and 80% on a tanker [23]. Shipping alone consumed 280 million metric tons of oil in 2001 [24], ~7.5% on the global oil consumption that year [25]. In 2012, shipping accounted for ~2.6% of global CO_2 emissions and expected to reach ~17% by 2050 [26]. It also accounted for ~13% and ~15% global SOx and NOx emissions [27], which are particularly hazardous for human`s heath. So even a mild drag reduction has a global impact for energy saving and greenhouse gas reduction.

When people saw water droplets rolling off the SHPo surface easily with very small friction, they started to wonder if similar reduction for friction can also happen if water flows pass the surface. However, on this subject, there is little help from nature with very few examples [17] to learn from. Watanabe *et al.* [28] was one of the earliest experimental studies on this subject, and they obtained 22% drag reduction in laminar flow, although the reported reduction is likely an over-estimation[29]. Since then, this subject has attracted enormous interest, leading to great advances in understanding of SHPo surface drag reduction mechanism and demonstration of drag reduction in both laminar and turbulent flows in different experiment conditions. However, after decades of research, there is still no successful demonstration of drag reduction in practical turbulent flows. Much work still needs to be done to achieve that goal.

1.2.1 Amount of Drag Reductions in Different Flow Conditions

When fluid flows over solid boundary, shear stress will occur on that boundary. The shear stress for a Newtonian fluid with constant viscosity is proportional to the velocity gradient:

$$\tau(\vec{u}) = \mu \nabla \vec{u} \tag{2-5}$$

where μ is the dynamic viscosity. The flow speed at the solid-fluid boundary is negligibly small and generally regarded as zero, referred as no-slip condition (Figure 1-4(a)). But at some height from the boundary the flow speed must equal to that of the fluid. This flow velocity change leads to velocity gradient at the boundary and shear stress, known as skin frictional drag. However, if the fluid flows over gas boundary (Figure 1-4(b)), the speed at the boundary won`t be zero, known as slip. Slip is quantified as slip length *b*, which is defined as an extrapolated distance relative to the wall where the tangential velocity component vanishes [29], as shown in Figure 1-4. For liquid flows over a solid surface covered with a uniform gas layer, as shown in Figure 1-4(b), assume the

dynamic viscosity of liquid and gas are given by μ_{liquid} and μ_{gas} and the gas layer thickness is h, then the slip length is:

$$b = h(\mu_{liquid} / \mu_{gas} - 1) \tag{2-6}$$

However, this scenario is only imaginary since the gas film is thermodynamically unstable. If fluid flows over SHPo surface. which traps gas in between surface roughness as shown in Figure 1-4(c), the slip length cannot be as high as that on uniform gas layer with same thickness, since there must be liquid-solid boundary which introduce no-slip condition. Nevertheless, the slip enhancement was found still significant compared with smooth solid surfaces in both laminar and turbulent flows. Most importantly, the gas-liquid interface can be stable on the rough source unlike that on a solid surface covered with a uniform gas layer (Figure 1-4).

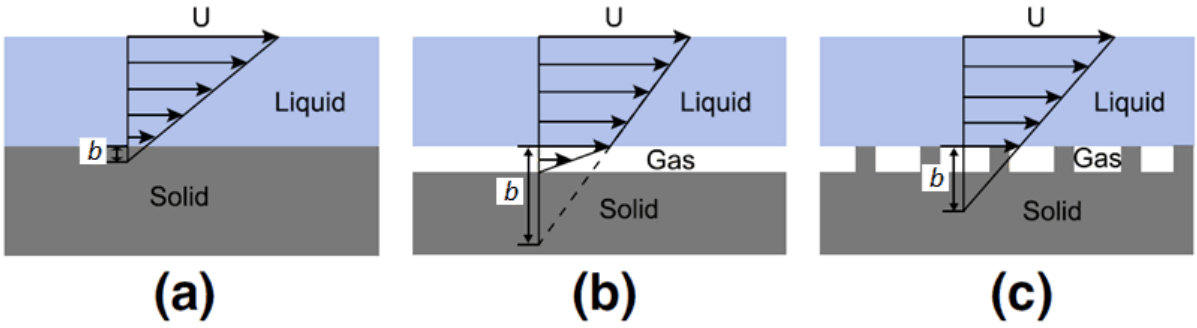

Figure 1-4 Liquid flow over a solid surface with a slip quantified as slip length (*b*). (a) Liquid flows over a hydrophobic solid surface with a negligibly small (tens of nanometers) slip length. (b) If hypothetically there exists a gas layer between a liquid and a solid, a liquid would flow with a large effective slip length because the gas has a much lower viscosity than the liquid. (c) When a composite interface with solid and gas is formed on a structured surface, a liquid may flow with an effective slip length approaching that of (b). [29]

SHPo surface drag reduction in laminar flows has already been reasonably understood [29, 30]. Drag reduction only depends on effective slip length, independent of flow conditions (e.g., Re). Slip length mainly depends on surface structural parameters. Analytical models, numerical simulations and experiments have agreed well on relationship between structural parameters on slip length for simple patterns [31-35] such as grates, posts and holes. According to these studies, for a given pattern type, the structural pitch (i.e., structure periodicity) and the gas fraction are the two most important parameters to determine slip length [29].

Compared with laminar flow, turbulence proposed many new challenges for SHPo surfaces. Complicated flow structures, such as streaks, eddies and vortices, can form in turbulent flows [36] and interact with SHPo surface structures. While the numerical studies generally predicted drag reduction of SHPo surface in turbulent flows, the experimental studies have shown large discrepancies. Depending on the microstructure geometry of the SHPo surface and the flow condition tested under, some experiments obtained a reduced drag by as much as ~75% [37] while some obtained an increased drag [38]. The relationship between drag reduction and surface geometry or flow condition is still an open topic for turbulent flows. Generally, drag reduction has been demonstrated at low Reynolds number range ($Re_\tau < 1000$ or $Re_x < 10^6$) but rarely seen at high Reynolds number range. The studies on SHPo surface in turbulent flow will be reviewed in detail in Chapter 4.

1.2.2 Gas Layer Stability on SHPo Surface

Despite occasional reports of high drag reduction in some experiments, wetting transition from Wenzel state to Cassie state is one of the main technological challenges for realistic applications of SHPo surfaces [39]. For SHPo surfaces that can reduce drag, the diffusion of trapped gas on

SHPo surfaces will inevitably cause the wetting transition at a usual immersion depth for commercial applications [20]. Moreover, the environmental factors, include marine fouling, external pressure change or physical damage, would also cause wetting transition. Many works have been done to make the SHPo surface more robust against wetting transition. One way is to introduce so-called hierarchical structure with two length scales: a large scale governing the effective wetting properties of the surface, and a much smaller scale that prevents the final stage of impregnation [40] by increasing the critical transition pressure. Another method would involve a back-pressurization of the underlying gas layer, notwithstanding subtle geometric properties of the pressurized Cassie state with pressure induced menisci curvature impacting both static and dynamic responses of the interface [41, 42]. However, none of these methods can prevent the SHPo surface from wetting transition underwater due to gas diffusion. To fundamentally solve this problem, recent studies [43, 44] introduced an active gas restoration mechanism on SHPo surface, as shown in Figure 1-5. After the SHPo surface gets wetted (Wenzel state), the gas restoration will be triggered and Wenzel-to-Cassie transition will happen. Since the gas restoration process starts by itself only when and where SHPo surface is wetted and stops by itself when and where SHPo surface is dewetted, it is called a "semi-active" surface to note its "self-regulating" nature of power consumption. The semi-active SHPo surface differs from the active surfaces, which consume power constantly to provide a gas shroud or bubbles or release a polymer.

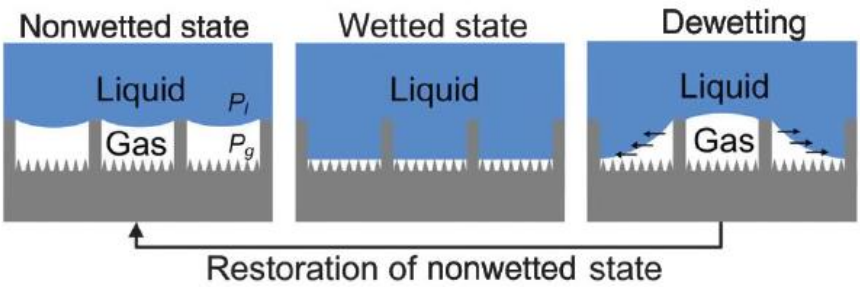

Figure 1-5 Dewetting process on SHPo surfaces using semi-active gas restoration process. [43]

1.2.3 Mass Production of Economical SHPo Surfaces

Based on the surface micro/nano structures, the SHPo surface can be divided into two categories: random structures and ordered structures. Random structure SHPo surface can be fabricated using a wide range of fabrication techniques, like colloidal assembly [45, 46], electrochemical deposition [47] or etching [48], nanofilament [49], and so-gel process [50]. There have been commercial products that can be applied by two-step spraying process (NeverWet, Rust-Oleum Inc.). Most of the random structure SHPo surfaces are compatible for mass manufacturing. However, as shown in recent turbulent drag reduction tests [51], random structure SHPo surfaces has its fundamental limitations in reducing drag at high Reynolds numbers, especially in open water.

Compared with random structure SHPo surfaces, SHPo surfaces with ordered structure, especially grating structures aligned in streamwise direction, have unambiguously shown drag reducing capability [51]. However, most of the ordered structures were fabricated in cleanroom environment using silicon-processing technologies [35, 37, 43, 52]. It is unlikely to use such fabrication process for realistic large-scale application. There have been some studies making SHPo surfaces using imprinting process [53, 54], which is compatible for mass manufacturing. But most of the resulting microstructures require an additional hydrophobic coating, which is unreliable in long-term application and prone to peeling off in harsh marine environment. We decide to develop mass manufacturing technologies using inherently hydrophobic materials.

1.3 Scope of The Research

We focus on addressing the three issues proposed above for SHPo surface drag reduction in realistic turbulent flow conditions. Chapter 2 studies the stability of gas layer on underwater SHPo surfaces with a rigor. We establish the theoretical model for wetting dynamics of underwater SHPo surface and verify the model experimentally. For the first time, we observe gas layer with infinite lifetime on artificial SHPo surfaces, reproducing the astonishing capability of backswimmer insect in nature. However, our results also show that the SHPo surface capable of drag reduction under realistic conditions (e.g., high immersion depth, environment change) will inevitably get wetted in a relatively short time (i.e., minutes to hours). Although this result breaks the fantasy that one can develop a SHPo surface robust to wetting transition for realistic application, it showed the importance of active dewetting mechanisms. In Chapter 3, to conduct flow test in different large flow facilities (e.g., towing tank, water tunnel, boat), we develop a high-resolution shear stress sensor that is compact, low profile, reliable, and robust. Different SHPo surfaces can be repeatedly attached and detached from the sensor for shear stress measurement. With its low profile and robustness, the sensor can fit into different facilities and be tested under different environments. Chapter 4 discusses the drag reduction tests of different SHPo surfaces in turbulent boundary layer (TBL) flows at large Reynolds number (10^6-10^7), i.e., in flows that resemble the hull of marine vessels, using the shear sensor developed in Chapter 2. Beside confirming drag reduction capability, the experiments studies the Reynolds number effect of SHPo drag reduction in turbulent flows, which has been predicted in numerical studies and small flow systems but not confirmed yet in large flow systems. Moreover, we conducted the first field test of SHPo surface on real marine vessel at high speeds and demonstrated drag reduction. Lastly, Chapter 5 discusses the design and fabrication of a new semi-active SHPo surface that does not use any external power for gas restoration. A hot-embossing process to fabrication such surfaces is developed to be scalable

for mass production for the passive and semi-active SHPo surfaces. Although the size of the molded SHPo surface is currently limited due to the availability of the equipment, the developed fabrication is essentially a one-step hot embossing process scalable for commercial large-area hot embossing facilities for mass production. Chapter 6 summarizes the dissertation and suggests future research directions.

1.4 References

[1] A. Lafuma and D. Quere, "Superhydrophobic states," *Nature Materials,* vol. 2, pp. 457-460, 2003.

[2] D. Neumann and A. Kureck, "Composite structure of silken threads and a proteinaceous hydrogel which form the diving bell wall of the water spider Agyroneta aquatica," *SpringerPlus,* vol. 2, 1, 2013.

[3] F. Shi, J. Niu, J. Liu, F. Liu, Z. Wang, X. Q. Feng, *et al.*, "Towards understanding why a superhydrophobic coating is needed by water striders," *Advanced Materials,* vol. 19, pp. 2257-2261, 2007.

[4] R. N. Wenzel, "Resistance of solid surfaces to wetting by water," *Industrial and Engineering Chemistry,* vol. 28, pp. 988-994, 1936.

[5] A. B. D. Cassie and S. Baxter, "Large Contact Angles of Plant and Animal Surfaces," *Nature,* vol. 155, pp. 21-22, 1945.

[6] D. Quéré, "Non-sticking drops," *Reports on Progress in Physics,* vol. 68, 2495, 2005.

[7] M. Nosonovsky and B. Bhushan, "Hierarchical roughness makes superhydrophobic states stable," *Microelectronic Engineering,* vol. 84, pp. 382-386, 2007.

[8] P. Brunet, F. Lapierre, V. Thomy, Y. Coffinier, and R. Boukherroub, "Extreme resistance of superhydrophobic surfaces to impalement: reversible electrowetting related to the impacting/bouncing drop test," *Langmuir,* vol. 24, pp. 11203-11208, 2008.

[9] Q. S. Zheng, Y. Yu, and Z. H. Zhao, "Effects of hydraulic pressure on the stability and transition of wetting modes of superhydrophobic surfaces," *Langmuir,* vol. 21, pp. 12207-12212, 2005.

[10] J. B. Boreyko and C. H. Chen, "Restoring Superhydrophobicity of Lotus Leaves with Vibration-Induced Dewetting," *Physical Review Letters,* vol. 103, 2009.

[11] T. Krupenkin and J. A. Taylor, "Reverse electrowetting as a new approach to high-power energy harvesting," *Nat Commun,* vol. 2, 448, 2011.

[12] W. Barthlott and C. Neinhuis, "Purity of the sacred lotus, or escape from contamination in biological surfaces," *Planta,* vol. 202, pp. 1-8, 1997.

[13] P. G. D. Matthews and R. S. Seymour, "Diving insects boost their buoyancy bubbles," *Nature,* vol. 441, pp. 171-171, 2006.

[14] M. Flynn and J. W. Bush, "Underwater breathing: the mechanics of plastron respiration," *Journal of Fluid Mechanics,* vol. 608, pp. 275-296, 2008.

[15] Y. M. Zheng, X. F. Gao, and L. Jiang, "Directional adhesion of superhydrophobic butterfly wings," *Soft Matter,* vol. 3, pp. 178-182, 2007.

[16] P. Ditsche-Kuru, E. S. Schneider, J. E. Melskotte, M. Brede, A. Leder, and W. Barthlott, "Superhydrophobic surfaces of the water bug Notonecta glauca: a model for friction reduction and air retention," *Beilstein Journal of Nanotechnology,* vol. 2, pp. 137-144, 2011.

[17] J. Davenport, R. N. Hughes, M. Shorten, and P. S. Larsen, "Drag reduction by air release promotes fast ascent in jumping emperor penguins—a novel hypothesis," *Marine Ecology Progress Series,* vol. 430, pp. 171-182, 2011.

[18] D. Schutz and M. Taborsky, "Adaptations to an aquatic life may be responsible for the reversed sexual size dimorphism in the water spider, Argyroneta aquatica," *Evolutionary Ecology Research,* vol. 5, pp. 105-117, 2003.

[19] R. Poetes, K. Holtzmann, K. Franze, and U. Steiner, "Metastable Underwater Superhydrophobicity," *Physical Review Letters,* vol. 105, 166104, 2010.

[20] M. Xu, G. Sun, and C.-J. Kim, "Infinite Lifetime of Underwater Superhydrophobic States," *Physical Review Letters,* vol. 113, 136103, 2014.

[21] H. K. Webb, R. J. Crawford, and E. P. Ivanova, "Wettability of natural superhydrophobic surfaces," *Advances in colloid and interface science,* vol. 210, pp. 58-64, 2014.

[22] B. Bhushan and Y. C. Jung, "Natural and biomimetic artificial surfaces for superhydrophobicity, self-cleaning, low adhesion, and drag reduction," *Progress in Materials Science,* vol. 56, pp. 1-108, 2011.

[23] K. Fukuda, J. Tokunaga, T. Nobunaga, T. Nakatani, T. Iwasaki, and Y. Kunitake, "Frictional drag reduction with air lubricant over a super-water-repellent surface," *Journal of Marine Science and Technology,* vol. 5, pp. 123-130, 2000.

[24] V. Eyring, H. Köhler, J. Van Aardenne, and A. Lauer, "Emissions from international shipping: 1. The last 50 years," *Journal of Geophysical Research: Atmospheres,* vol. 110, 2005.

[25] BP statistical reivew of world energy [Online]. Available: http://www.bp.com/en/global/corporate/energy-economics/statistical-review-of-world-energy/downloads.html

[26] F. HENRY. (2015). *Building Greener Ships, to Keep the Sea From Rising*. Available: http://www.nytimes.com/2015/12/08/science/carbon-emissions-shipping-container-ships.html?_r=0

[27] K. Wallis and R. Khasawneh. (2016). *Shippers brace for new rules to cut deadly sulfur emissions*. Available: http://www.reuters.com/article/us-shipping-regulation-imo-idUSKCN1240KF

[28] K. Watanabe, K. Ohkido, and H. Mizunuma, "Drag reduction in flow through square and rectangular ducts with highly water repellent walls," *ASME-PUBLICATIONS-FED*, vol. 237, pp. 115-120, 1996.

[29] C. Lee, C.-H. Choi, and C.-J. Kim, "Superhydrophobic drag reduction in laminar flows: a critical review," *Experiments in Fluids*, vol. 57, 176, 2016.

[30] J. P. Rothstein, "Slip on Superhydrophobic Surfaces," *Annual Review of Fluid Mechanics*, vol. 42, pp. 89-109, 2010.

[31] E. Lauga and H. A. Stone, "Effective slip in pressure-driven Stokes flow," *Journal of Fluid Mechanics*, vol. 489, pp. 55-77, 2003.

[32] C. Ybert, C. Barentin, C. Cottin-Bizonne, P. Joseph, and L. Bocquet, "Achieving large slip with superhydrophobic surfaces: Scaling laws for generic geometries," *Physics of Fluids*, vol. 19, 2007.

[33] A. M. J. Davis and E. Lauga, "Hydrodynamic friction of fakir-like superhydrophobic surfaces," *Journal of Fluid Mechanics*, vol. 661, pp. 402-411, 2010.

[34] A. M. J. Davis and E. Lauga, "The friction of a mesh-like super-hydrophobic surface," *Physics of Fluids*, vol. 21, 113101, 2009.

[35] C. Lee, C.-H. Choi, and C.-J. Kim, "Structured surfaces for a giant liquid slip," *Physical Review Letters*, vol. 101, 64501, 2008.

[36] A. Yoshizawa, "Statistical-Theory for Compressible Turbulent Shear Flows, with the Application to Subgrid Modeling," *Physics of Fluids*, vol. 29, pp. 2152-2164, 1986.

[37] H. Park, G. Sun, and C.-J. Kim, "Superhydrophobic turbulent drag reduction as a function of surface grating parameters," *Journal of Fluid Mechanics*, vol. 747, pp. 722-734, 2014.

[38] E. Aljallis, M. A. Sarshar, R. Datla, V. Sikka, A. Jones, and C. H. Choi, "Experimental study of skin friction drag reduction on superhydrophobic flat plates in high Reynolds number boundary layer flow," *Physics of Fluids*, vol. 25, 2013.

[39] L. Bocquet and E. Lauga, "A Smooth Future?," *Nature Materials*, vol. 10, pp. 334-337, 2011.

[40] C. Lee and C. J. Kim, "Influence of Surface Hierarchy of Superhydrophobic Surfaces on Liquid Slip," *Langmuir*, vol. 27, pp. 4243-4248, 2011.

[41] A. Steinberger, C. Cottin-Bizonne, P. Kleimann, and E. Charlaix, "High friction on a bubble mattress," *Nature Materials*, vol. 6, pp. 665-668, 2007.

[42] A. M. J. Davis and E. Lauga, "Geometric transition in friction for flow over a bubble mattress," *Physics of Fluids*, vol. 21, 2009.

[43] C. Lee and C.-J. Kim, "Underwater Restoration and Retention of Gases on Superhydrophobic Surfaces for Drag Reduction," *Physical Review Letters,* vol. 106, 14502, 2011.

[44] C. Lee and C.-J. Kim, "Wetting and Active Dewetting Processes of Hierarchically Constructed Superhydrophobic Surfaces Fully Immersed in Water," *Journal of Microelectromechanical Systems,* vol. 21, pp. 712-720, 2012.

[45] Y. Horiuchi, K. Fujiwara, T. Kamegawa, K. Mori, and H. Yamashita, "An efficient method for the creation of a superhydrophobic surface: ethylene polymerization over self-assembled colloidal silica nanoparticles incorporating single-site Cr-oxide catalysts," *Journal of Materials Chemistry,* 2011.

[46] J. Y. Shiu, C. W. Kuo, P. Chen, and C. Y. Mou, "Fabrication of tunable superhydrophobic surfaces by nanosphere lithography," *Chemistry of materials,* vol. 16, pp. 561-564, 2004.

[47] S. T. Wang, Y. L. Song, and L. Jiang, "Microscale and nanoscale hierarchical structured mesh films with superhydrophobic and superoleophilic properties induced by long-chain fatty acids," *Nanotechnology,* vol. 18, 2007.

[48] H. Costa and I. Hutchings, "Development of a maskless electrochemical texturing method," *Journal of Materials Processing Technology,* vol. 209, pp. 3869-3878, 2009.

[49] N. A. Malvadkar, M. J. Hancock, K. Sekeroglu, W. J. Dressick, and M. C. Demirel, "An engineered anisotropic nanofilm with unidirectional wetting properties," *Nat Mater,* vol. 9, pp. 1023-1028, 2010.

[50] Z. B. Huang, Y. Zhu, J. H. Zhang, and G. F. Yin, "Stable biomimetic superhydrophobicity and magnetization film with Cu-ferrite nanorods," *Journal of Physical Chemistry C,* vol. 111, pp. 6821-6825, 2007.

[51] K. B. Golovin, J. W. Gose, M. Perlin, S. L. Ceccio, and A. Tuteja, "Bioinspired surfaces for turbulent drag reduction," *Phil. Trans. R. Soc. A,* vol. 374, 20160189, 2016.

[52] C.-H. Choi and C.-J. Kim, "Large slip of aqueous liquid flow over a nanoengineered superhydrophobic surface," *Physical Review Letters,* vol. 96, 066001, 2006.

[53] G. Jin and G. Kim, "Pressure/Electric-Field-Assisted Micro/Nanocasting Method for Replicating a Lotus Leaf," *Langmuir,* vol. 27, pp. 828-834, 2011.

[54] M. Sun, C. Luo, L. Xu, H. Ji, Q. Ouyang, D. Yu, *et al.*, "Artificial lotus leaf by nanocasting," *Langmuir The Acs Journal Of Surfaces And Colloids,* vol. 21, pp. 8978-8981, 2005.

Chapter 2 Longevity of Underwater Superhydrophobic States

The materials in this chapter have mostly been published in [1, 2].

2.1 Introduction

Stability of the air layer on superhydrophobic (SHPo) surfaces fully submerged in water is of critical importance because their key anticipated applications, such as drag reduction [3-6] and anti-biofouling [7], are under water. Unfortunately, the air film on the underwater SHPo surface, often called plastron, is fragile [3, 8]. Over time, the air initially trapped on the SHPo surface diffuses away into the surrounding water, collapsing the air-water interface and causing a transition from the dewetted to wetted state [9]. Recent experimental studies showed that the lifetime of the underwater SHPo state is influenced by various environmental parameters [8, 10-12]. However, most of the studies only reported statistical information, such as average wetting time, while more direct knowledge such as air-depletion dynamics or the effect of roughness geometries is needed to design SHPo surface more robust against wetting. While some underwater insects boast a long-term or even indefinite (tested up to 120 days [13]) plastron, all artificial SHPo surfaces retained their plastron much shorter (mostly less than an hour and rarely days [8, 10, 14-16]). To date, no artificial SHPo surface has been demonstrated to retain an air layer indefinitely unless assisted [17].

2.2 Theoretical Model

2.2.1 Gas Diffusion

Let us first analyze how the trapped air is depleted from a hydrophobic trench after being submerged based on previous works [16, 18, 19]. Consider a simple trench with width *w*, length *l*, and depth *h*, as defined in Figure 2-1(a), and the radius of curvature of the air-water interface *R*, as defined in Figure 2-1(b). Since the trench length is much larger (~10 times) than its width, the meniscus was straight along the length of the trench in the middle section over a significant period of time before reaching the bottom, as shown in Figure 2-4(a), supporting the 2D diffusion model as a crude but useful approximation. According to Henry`s law, the partial pressure of a gas equilibrated in water is: $p = k_H c$ , where $k_H$ is Henry`s constant and c is the dissolved gas concentration in water. Right after submerging the sample from atmosphere (p_{atm}) to immersion depth H at hydrostatic pressure p_H, the air in the trench is compressed to $p_{tr,0}$ and the meniscus forms the radius of curvature R_0.

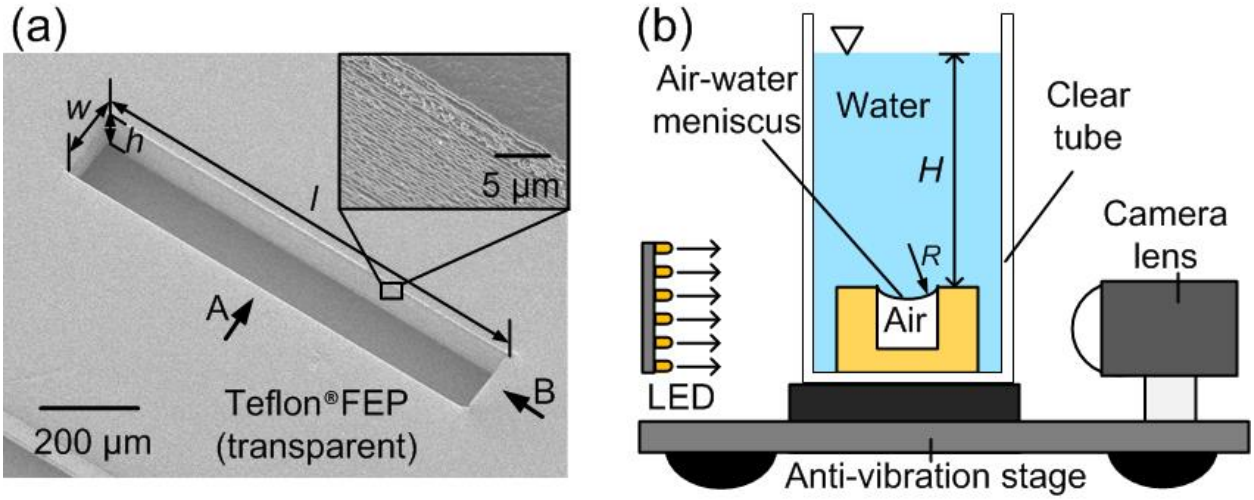

Figure 2-1 The sample and testing setup for SHPo surface wetting dynamics. (a) SEM images of single-trench sample with the microscale trench characterized by length *l*, width *w*, and depth *h*. (b) Schematic illustration of the experimental setup to visualize the air-water meniscus inside the

trench throughout the depletion process. One sample was immersed in water of height in a clear tube and observed from side as indicated by the arrow A in (a).

When the above-prepared Teflon FEP sample is immersed in water, the air at atmospheric pressure is entrapped in the microscopic trench. Assuming the sample surface crosses the free surface of water very slowly so that the trench is closed off with a flat air-water meniscus, we can say at the crossing the trapped air has the pressure of atmosphere p_{atm} and the volume of trench V_{tr} determined by the trench width w, depth h, and length l. As the sample is lowered to depth H, the trapped air is compressed by the hydrostatic pressure p_H to a volume of V_0 at $p_{tr,0}$ at time $t = 0$. If the meniscus is pinned at the top edge of the trench, the compression makes the meniscus bend down into the trench, and the capillary pressure by the air-water interfacial tension σ helps counter the hydrostatic pressure. Assuming the air is ideal gas and compressed isothermally [19], Laplace equation and the ideal gas law lead to:

$$p_{atm} + p_H - p_{tr,0} = \sigma / R_0 \tag{3-1}$$

$$p_{atm} V_{tr} = p_{tr,0} V_0 \tag{3-2}$$

By combining the above two equations, the initial radius of curvature R_0 after submerging the sample to a depth H can be calculated as:

$$R_0 = \frac{s}{p_{atm}(1 - V_{tr} / V_0) + p_H} \tag{3-3}$$

where V_0 can be expressed in terms of V_{tr} and R_0. Since $V_0 \le V_{tr}$ and $R_0 \ge s / p_H$ with the equality for an infinitely deep trench (i.e., $h \to \infty$), this equation indicates that at fresh immersion (i.e., before diffusion starts) the meniscus bends down less on a shallow trench than on a deep trench.

If $p_{tr,0} > k_H c$, air in the trench will start to diffuse out through the meniscus. The volume rate of dissolution (i.e., dissolution rate) of the trapped air into the water is limited by the diffusion of dissolved air in the water, which is related to the temporal and spatial evolvement of concentration field by Fick`s law approximated [19] as:

$$\frac{dV(t)}{dt} = -k_p A(t)[p_{tr}(t) - k_H c] \tag{3-4}$$

where V is the air volume, k_p is the mass transfer coefficient of air across the air-water interface, p_{tr} is the air pressure in the trench, and A is the meniscus area. Combining Equation (3-4) with Laplace equation across the meniscus $p_{atm} + p_H - p_{tr} = \sigma / R$, where σ is the air-water interfacial tension, we get:

$$\frac{dV(t)}{dt} = -k_p A(t)[p_H - \frac{\sigma}{R(t)} + p_{atm} - k_H c] \tag{3-5}$$

In Equation (3-5), The interface diffusion coefficient k_p is affected by the meniscus curvature, as studied in the diffusion-limited drop evaporation theory [20], which assumed quasi-stationary, diffusion-controlled evaporation in still air. Its boundary conditions at the meniscus and infinity were similar to our study. In the theory, the mass transfer rate is:

$$\frac{dm(t)}{dt} = -\frac{kr_0(C/r)\sin\theta_0}{2\sin\theta} \tag{3-6}$$

where θ is the angle of meniscus with respect to the horizontal surface with θ_0 as its initial value, r is the meniscus radius with r_0 as its initial value, and k is a constant. Related to θ, C/r has its empirical polynomial estimated from [20]. The ratio between two mass transfer rates of two different curvatures is:

$$K = (\frac{dm}{dt})_1 / (\frac{dm}{dt})_2 = \frac{C_1 / (r_1 \sin\theta_1)}{C_2 / (r_2 \sin\theta_2)} \tag{3-7}$$

When the meniscus is flat so that θ_1 is 0°, $C_1 / (r_1 \sin q_1) = 2/p \simeq 0.63$ [20]. When the meniscus forms the advancing contact angle on the trench sidewall (θ_{adv} = 130° in this study) so that θ_2 is 40°, $C_2 / (r_2 \sin q_2) \simeq 0.73$, and the ratio K is about 0.86. However, this result is for a spherical droplet. Having about half the value, the curvature of the meniscus on the long trench of this Letter is expected to affect the mass diffusion rate less than the above discussion. To calculate the interface diffusion coefficient k_p, we eventually used the diffusion length, which assumes a constant mass transfer rate and was used in recent work [16]. The interface diffusion coefficient k_p can be estimated using "film theory" for mass transfer across interfaces [21]:

$$k_p = \frac{D}{\delta} \cdot \frac{M}{k_H \rho_{air}} \tag{3-8}$$

Here, δ is the "diffusion length", typically around 0.1 mm for short diffusion time (i.e., ~ 10^3 s) [16, 21]. Other values are obtained from reference [22] measured at 22 ºC: M is the molecular weight of air (i.e., 29 g/mol); ρ_{air} is the density of air (i.e., 0.0012 g/cm^3); D is the diffusion constant of air in water (i.e., 1.75–2.00×10^{-5} cm^2/s); and k_H is Henry`s constant (i.e., 1.21–1.34 atm/mM). Henry`s constant is invariant of hydrostatic pressure, unless the immersion depth is very large (e.g., H_r only increases by 14% at ~1000 m of water depth [23]). By substituting these values in Equation (3-8), k_p is calculated to be around 3×10^{-12} cm/(sec•Pa), which is around the extracted value from Figure 2-4(b) or 2.5×10^{-12} cm/(sec•Pa).

2.2.2 Meniscus Dynamics

Here, we consider only depinning impalement (not sagging [24, 25]) because the trench is much deeper than wide. The wetting process goes through two stages: (i) Stage I involves the contact

line pinned to the top edge of the trench, and (ii) Stage II involves the contact line sliding on the sidewall of the trench.

For the pinned stage of Stage I, R can be numerically calculated with initial condition R_0 and boundary condition R_c. Based on the 2D schematics in the right column named "B (midsection view from end)" of Figure 2-4(a), i.e., assuming an infinitely long trench, the area of the meniscus A and the volume of the trapped air V can be obtained from the trench dimensions and the radius of curvature of the meniscus R as:

$$A = 2R\arcsin(\frac{w}{2R}) \tag{3-9}$$

$$V = wh - [R^2 \arcsin(\frac{w}{2R}) - \frac{w}{2}\sqrt{R^2 - \frac{w^2}{4}}] \tag{3-10}$$

The rate of the air volume change can be expressed as the rate of the meniscus radius change as:

$$\frac{dV(t)}{dt} = \frac{dV(R)}{dR} \cdot \frac{dR(t)}{dt} \tag{3-11}$$

where $dV(R)/dR$ can be obtained from Equation (3-10). After substituting Equation (3-11) into Equation (3-5), the resulting first-order differential equation was solved numerically for R, and the meniscus position s was calculated from

$$s = R - \sqrt{R^2 - (w/2)^2} \tag{3-12}$$

and drawn in Figure 2-4(b) as theoretical curves. Since the depinning occurs when the angle of the meniscus on the sidewall reaches the advancing contact angle θ_{adv} [24], $R_c = -w/2\cos\theta_{adv}$.

For the sliding stage of Stage II, since $R = R_c = \text{constant}$ for the simple trench, the meniscus slides down the vertical sidewall at constant speed $u = d(V/A)/dt$, which can also be obtained from

Equation (3-5). The meniscus movement was estimated from video recordings, assuming a smooth sidewall. The scallops on the sidewalls were too small (~ 500 nm apart) to appear in the optical images (e.g., Figure 2-4(a)) used for the measurement. If diffusion rate $dV(t)/dt$ can decrease to zero during the pinned stage (Stage I), the meniscus will reach a stable state and the air loss will cease. However, once the meniscus depins and proceeds to the sliding stage (Stage II), the meniscus curvature and pressure p_{tr} will not change anymore. Defined as the maximum immersion depth beyond which the air-water meniscus has no stable state, the critical immersion depth H_c is the depth where air diffusion rate decreases to zero at the end of Stage I. By substituting $dV(t)/dt = 0$ and $R = R_c = w/2\cos\theta_{adv}$ into Equation (3-5), we obtain:

$$H_c = -\frac{2\sigma\cos\theta_{adv}}{w\rho g} + \frac{k_H c - P_{atm}}{\rho g} \tag{3-13}$$

where ρ is the density of water and g is the gravitational acceleration. Note that $k_H c - p_{atm}$ is the difference between the pressures of the dissolved air at the immersion depth and the atmospheric air just above the water. If the dissolved air is in full equilibrium with the atmosphere so that $k_H c - p_{atm} = 0$, Equation (3-13) reduces to the well-known relation below [26]:

$$H_c = -\frac{2\sigma\cos\theta_{adv}}{w\rho g} \tag{3-14}$$

Assuming equilibrium, Equation (3-14) simply states that the critical immersion depth is when the hydrostatic pressure at the depth equals the Laplace pressure sustainable by the interface at the trench. In contrast, Equation (3-13) further specifies how the critical immersion depth is affected when the condition diverges from the equilibrium. Because the environmental parameters (e.g., temperature, atmospheric pressure) keep changing in reality, the dissolved air at the immersion

depth is always in the process of equilibrating through diffusion, so $k_H c - p_{atm} \neq 0$ in reality. The above analysis is based on a single component gas but still applies to multiple component gases (e.g., air) since partial volumes and partial pressures can be added.

2.3 Experimental Verification of Theoretical Model

2.3.1 Experiment Sample and Setup

In order to systematically study the effect of geometric parameters of the surface structures for an intended goal, SHPo surfaces made of regular structures would be far more informative than those of random structures that produce only statistical data. Furthermore, for drag-reduction application in particular, SHPo surfaces with parallel trenches [4, 5, 27, 28] have been found to outperform those with random structures [29, 30], making SHPo surfaces with trenches a good candidate to study. Since multiple trenches are in parallel and isolated from each other, a single trench can represent the whole SHPo surface as far as the stability of the trapped air is concerned. The potential over-estimation of the depletion speed on single trench compared with the parallel trenches due to the edge effect [31, 32] is considered minor to our goal. Importantly for our purpose instead, a sample with single trench would allow clear images of one air-water meniscus; in comparison, multiple menisci in multiple trenches would overlap and blur the images.

The single-trench sample was fabricated from Teflon FEP by hot embossing with a silicon mold, as illustrated in Figure 2-2. The mold was fabricated by deep reactive ion etching (DRIE) on a 500 μm-thick silicon wafer using photoresist as etching mask. A thin Teflon FEP sheet (McMaster-Carr Supply Co., Inc.) was pressed into the silicon mold at temperature higher than its glass transition temperature (265 ℃ [33]). After transferring the silicon-FEP-glass onto a cold plate and allowing a cooldown, the Teflon FEP sample was manually demolded from the silicon mold. The

resulting sample is semi-transparent and intrinsically hydrophobic with advancing contact angle on smooth surface ~ 115° [34]. Figure 2-1(a) shows scanning electron microscopy (SEM) images of the single-trench sample. The sidewall of the trench has nanometer-scale roughness, as it was replicated from the "scalloped" surface [35] on the DRIE silicon mold.

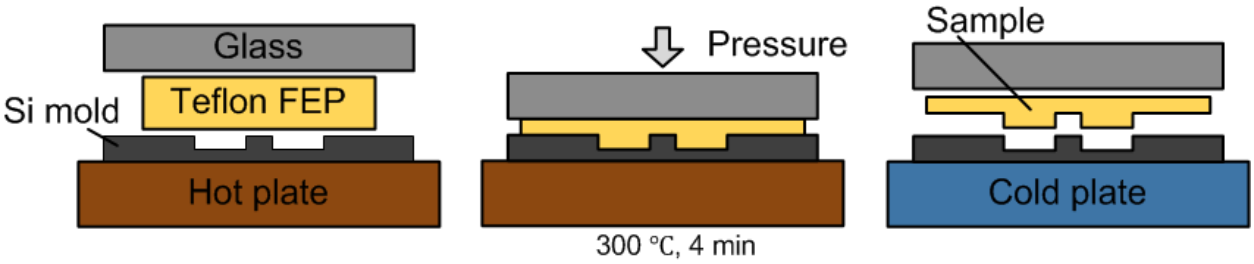

Figure 2-2 Molding process to form an optically clear Teflon FEP single-trench sample.

Silicon mold is ~500 μm thick; glass plate is ~1 mm thick; and Teflon FEP sample is around 10 mm x 5 mm x 0.5 mm.

In order to elucidate the dynamic process of air depletion and trench wetting, a setup was developed to directly visualize the meniscus, as schematically illustrated in Figure 2-1(b). Unlike the confocal microscopy based [8, 16, 24] studies, a cool LED (NuGreen Flexible Neck LED Desk Lamp, Newer Technology) was used as the light source to allow long-term observation without heating.

For large amount of sample testing just for lifetime data, all the samples were tested simultaneously in 19 tubes of varying water levels, using multiple low-cost cameras (Dino-Lite) as shown in Figure 2-3. Two identical samples, i.e., of an identical trench geometry, were placed in a tube to produce two data points for each of all test conditions. Although this setup does not provide the vertical position or shape information of the meniscus shown in Figure 2-1(b), it can still

conclusively determine whether the meniscus touched the bottom of the trench, i.e., reached the lifetime. Since the samples were placed vertically in the tube for the lifetime tests for convenience (e.g., to fit in the narrow bottom of the tube, make the sample handling easier, and ease the adjustment of lighting, etc.), the immersion depth varied along the channel length. However, the channel length (l = 1 mm) was much smaller than the immersion depth (H > 50 mm) so that the length effect was negligible in the lifetime data.

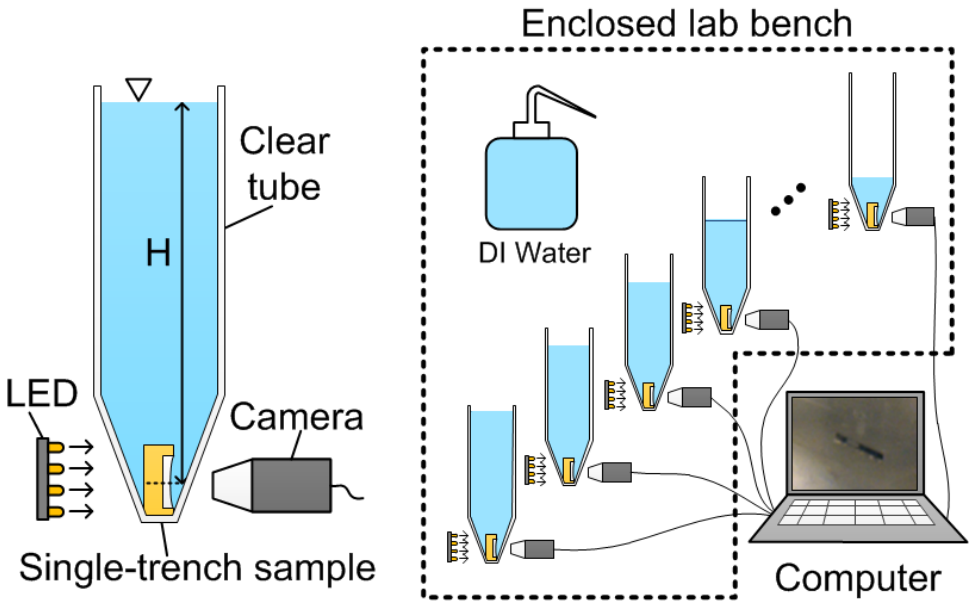

Figure 2-3 Schematic illustration of the experimental setup to monitor the lifetime. Each tube has two identical samples (although only one is drawn for clarity) at the bottom and is filled with water to an assigned height H. By employing multiple cameras, 38 samples were monitored simultaneously for the entire testing period (> 1200 hours). Water loss by evaporation was compensated once a day using the reserve water in a bottle kept in the same bench throughout the experiment.

The meniscus stability in the trench was found to be very sensitive to environment fluctuations, especially if the surrounding water was of a large amount. When various parameters (e.g., pressure, temperature) of the environment change, the corresponding parameters in the water (e.g., the dissolved gas concentration, temperature) change slowly with a time lag. The lagging responses make the states of water at a given moment somewhat different from the states of water in full equilibrium with the surrounding, leading to a deviation from the theoretical model, which was based on full equilibrium. In order to emulate the equilibrium states as close as possible, the experiment was carried out with small-diameter (~1.5 cm) tubes in an enclosed lab bench with no air flow, no agitations, and minimal temperature variations. Deionized water was left in the bench for a minimum of 2 days before using so that the water is fully saturated with surrounding air [15]. The temperature (21.3 ± 0.5 ℃) and relative humidity (53 ± 3 %) in the lab bench were monitored throughout the experiment (> 1200 hours) using a barometer (Wireless Weather Forecaster, SpringField Precision, Inc.). In order to compensate for the water loss by evaporation, which decreases the immersion depth, the tubes were refilled once a day using a water bottle kept in the same bench with the tubes. The variation of the water level in the tube was less than ~ 5 mm throughout the experiment.

2.3.2 Underwater SHPo Surface Wetting Dynamics

As shown in Figure 2-4(a), curved across the width of the trench, the meniscus appears as a dark strip, whose upper border is the two contact lines on the two sidewalls and lower border is the lowest position between the two sidewalls. When the sample was just immersed in water, the meniscus was almost flat and pinned at the top edges of the trench, as shown in the image at t = 0 hr. At t = 0.5 hr, the meniscus bent down as some of the trapped air diffused out, but the meniscus was still pinned to the top edges. As more air diffused out, the meniscus continued to bend down

until finally depinning from the top edges and moving down the sidewall, as shown in the image at t = 4 hr. When the meniscus touched the bottom of the trench, the meniscus split into two and spread rapidly towards the ends to satisfy the local contact angle (~120°) on the bottom surface, turning the contact line along the trench length convex and in compensation making that along the trench width concave. The spreading slowed down as the spreading menisci started to compress the air trapped at the corners, as suggested by the curvature change of the contact line. The trapped air continued to diffuse into the water and disappeared eventually. In this study, we define the "lifetime" of the trapped air in the trench as the time between the moment of immersion and the moment of the meniscus touching the trench bottom. However, this definition should not be considered universal. For SHPo drag reduction, as an example, the time to the meniscus depinning, after which the designed reduction is compromised, may define the lifetime better.

In Figure 2-4(b), the meniscus movement shown in Figure 2-4(a) was quantified for a sample immersed at two different depths. For small immersion depth (i.e., H = 50 mm), the meniscus bent down and stayed relatively stable, remaining in Stage I for many hours. However, for large immersion depth (i.e., H = 165 mm), the meniscus bent down, depinned, moved down, and touched the bottom. The meniscus position decreased faster at the beginning during Stage I but slowed down to a constant speed (i.e., linear trend) during Stage II. The lines are drawn from Equation (3-5) with $k_H c - P_{atm} = 0$, which are consistent with [19], using R_0 and k_p derived and using measured θ_{adv}. In addition to helping us define the lifetime, the results in Figure 2-4 confirm the theoretical model based on two stages of wetting and suggest the existence of stable menisci, i.e., infinite lifetime.

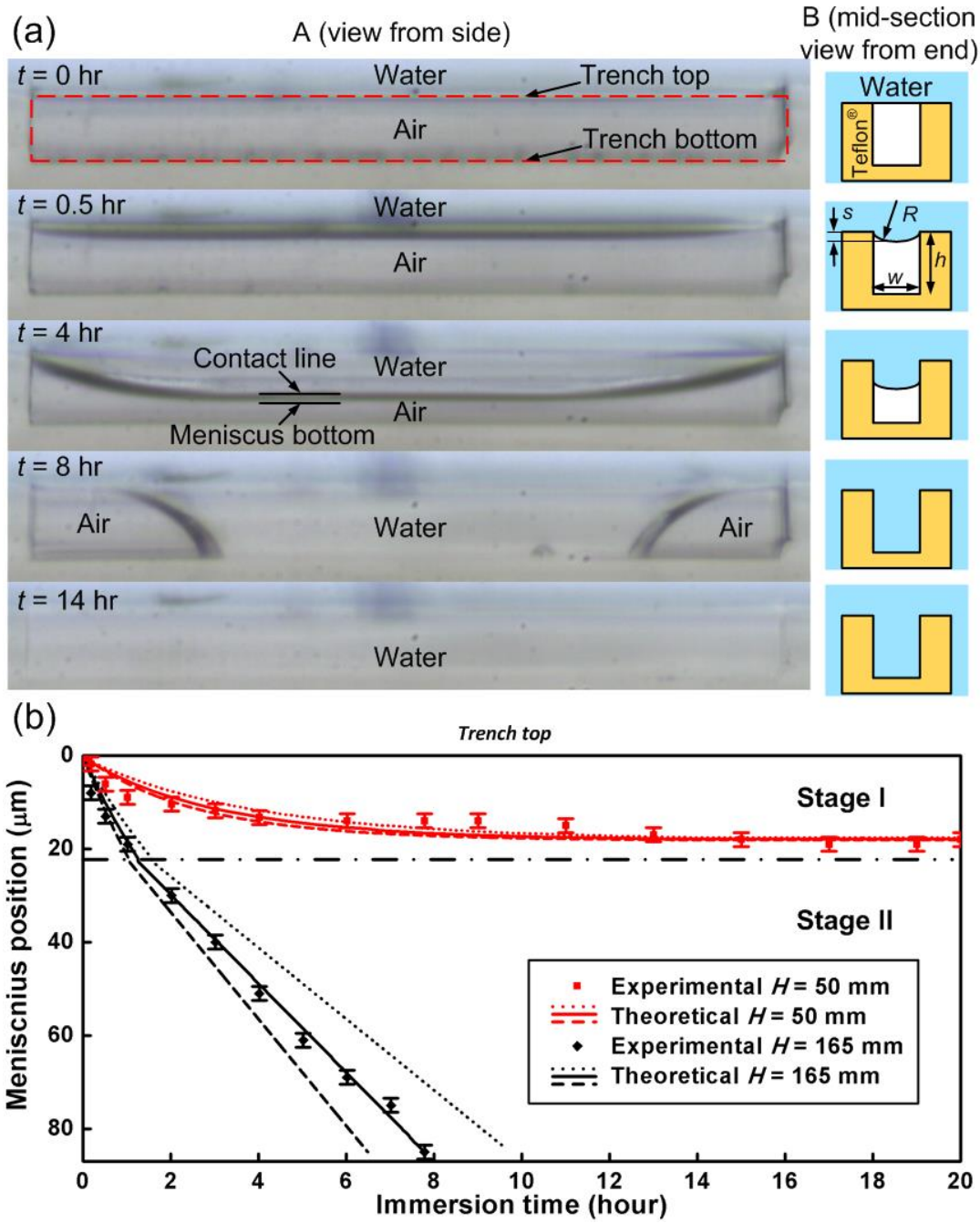

Figure 2-4 Observed air depletion and trench wetting. (a) Air-water meniscus visualized by the setup shown in Figure 2-1(b) with the viewing direction A shown in Figure 2-1(a). Images from top to bottom show meniscus starting to bend, depinning, sliding down, touching trench bottom and fully wetting the trench. Shown on the right are the corresponding cross-sectional schematics

with the viewing direction B. (b) Experimental and theoretical data of meniscus position over time reveal two distinctive stability conditions, determined by the immersion depth *H*. The meniscus position is defined as the distance from the top edge of the trench to the lowest position of meniscus. Experimental data were obtained from continuous microscopy images of the air-water meniscus, as shown in Figure 2-4(a), using samples with w = 147 μm, h = 85 μm, l = 1 mm. Uncertainty of the position measurement (~ 3 μm) is shown in the figure. Calculated for the same trench geometry and immersion depth, the solid line fit the data best with $k_p = 2.5\times10^{-12}$ cm/(sec•Pa), while the dotted lines show the influence of k_p with 2×10^{-12} cm/(sec•Pa) and 3×10^{-12} cm/(sec•Pa), respectively. The dot-dash line denotes the maximum deflection of the meniscus while remaining pinned at the top edge.

The advancing contact angle θ_{adv} on the trench sidewall was determined by observing an air bubble shrinking inside the trench. Figure S3 shows an image right before the bubble depinned from the top edge of the trench. The advancing contact angle was measured to be ~130^o, larger than that on a smooth Teflon FEP surface (~115^o [34]) because of the rough sidewall shown in Figure 2-1(a).

Figure 2-5 Measurement of advancing contact angle on trench sidewall. The advancing contact angle was read using the bubbles shrinking at the two ends of the trench after the meniscus touched the bottom. The picture is the frame when the left bubble's triple contact line at the top edge of the trench was about to depin. The advancing contact angle is estimated to be ~130°. The right bubble had already depinned.

2.3.3 Effect of Surface Geometry and Immersion Depth

If only lifetime data of the air pocket is needed without the depletion dynamics above, the setup can be simplified by placing the sample sideways and observe the trench from above its opening with a low magnification camera, as schematically illustrated in Figure 2-3. Three exemplary images captured from a video clip are shown in Figure 2-6(a). The total reflection of the light from behind the sample made the meniscus in the trench appear darker to the camera, compared with the rest of the sample. These observations were confirmed consistent with the detailed dynamics of Figure 2-4, validating the simplified setup, which allowed us to monitor multiples samples simultaneously and continuously in a controlled environment.

Figure 2-6(b) shows the lifetime of the trapped air of multiple samples tested at varying immersion depth. All samples (10 mm x 5 mm x 0.5 mm Teflon FEP piece) have one trench with the same length (l = 1 mm) and depth (h ~ 85 μm) but three different widths. For all three trench widths the lifetime increased as the immersion depth decreased, which is consistent with Equation (3-13) and previous experimental results [8, 14, 16]. However, when the immersion depth was smaller than a certain value, the trench retained the air pocket for a very long time. We declared the lifetime "infinite" after 1200 hours (50 days) and terminated the recording, but some tests were left to continue with no sign of wetting. For each trench width, the critical immersion depth H_c should be between the last data (i.e., the smallest depth) among those that got wet and the first data (i.e., largest depth) that showed an indefinite lifetime, indicating the uncertainty of measuring instability data. As shown in Figure 2-6(c), the experimentally obtained ranges of H_c matched the theoretical reciprocal curve based on Equation (3-14). As expected, trenches with a smaller width can be submerged deeper without losing the air pocket. Since the environmental fluctuation cannot be

completely eliminated, the experimental data is slightly smaller (i.e., shallower) than the theoretically predicted depth in Figure 2-6(c).

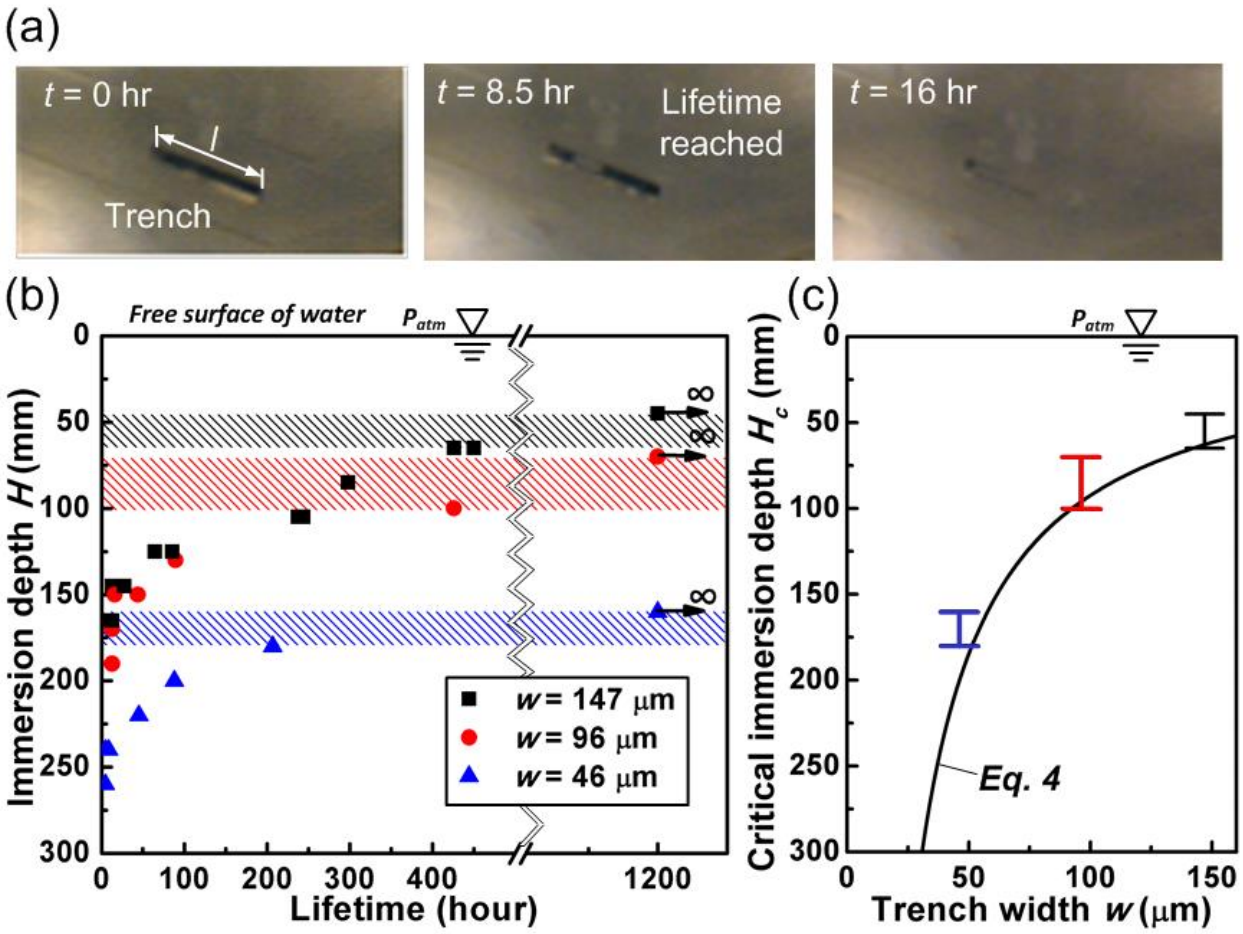

Figure 2-6 Observed lifetime of trapped air. (a) Air-water meniscus seen from above the sample with low-magnification camera. The meniscus appears black. The black strip at t = 0 hr, the broken strip at t = 8.5 hr, and the disappearance of strip at t = 16 hr indicate beginning, touching bottom, and full wetting, respectively, corroborating the observation in Figure 2-4(a). (b) Lifetime of trapped air as a function of immersion depth with trench width of 147 μm (■), 96 μm (●), and 46 μm (▲) as the parameter. The measurement errors of immersion depth (i.e., ± 2.5 mm due to evaporation) and lifetime (i.e., the interval between snapshots) are too small to appear in the given

scales. The symbols with an arrow indicate at least 1200 hours, considered "infinite" in this study. Each of the three colored shades indicates the uncertainty range of critical depth H_c for a given trench width. (c) Critical immersion depth H_c as function of trench width w. The experimental results are from the uncertainty ranges (i.e., the colored shades) in (b). The solid line is the theoretical prediction of Equation (3-14) with 130^o as the advancing contact angle measured on the trench sidewall.

2.3.4 Discussion

To the best of our knowledge, this is the first experimental verification of infinite lifetime of entrapped gas on microstructured surfaces fully submerged in water. Compared with previous tests, we note several aspects critical to our success. (1) The surface should be tested at a smaller depth than the critical immersion depth. However, this basic requirement was not always met before (e.g., [16]). (2) The samples in this Letter had a simple and distinctive geometry and were carefully examined to avoid any defect. Assuming a similar dimensional scale, an ordered structure is favored over random structures [8, 14, 15], because the latter get wetted more easily as discussed in SM. (3) Made entirely of Teflon FEP, the samples in this Letter did not need any hydrophobic coating, which is a typical source of defects for SHPo surfaces. Many used self-assembled monolayer (SAM) [15, 16, 26], which was found to degrade under water over time [36]. (4) The experimental procedure was carefully controlled and environmental fluctuations minimized, as detailed in SM. This extreme care was especially important when the testing depth was close to the theoretical limit.

It would be informative to relate the current results with different surfaces reported in the literature, e.g., schematically drawn for random protrusions of lotus-leaves-like surfaces [8] in Figure 2-7(a)

and parallel microtrichia of underwater insect skins [13, 18] in Figure 2-7(c). Assuming same material (i.e., same contact angle) and similar structure spacing, their morphologies would determine the critical radii of curvature R_c and thus the critical immersion depth H_c. For the random structures of Figure 2-7(a), the sloped sidewalls and non-uniform heights make R_c larger and H_c smaller. On the other hand, for the parallel structures of Figure 2-7(c), the re-entrance of the structures makes R_c smaller and H_c larger, explaining the observation for indefinite plastron. Importantly, the habitat of these underwater insects is much shallower (e.g., H ~ 15 cm [13]) than the H_c value calculated from their surface structures (e.g., H_c > 15 m for ~0.5 μm microtrichia [13], assuming local advancing contact angle of 120°). We speculate that the large safety factor (~100×) helps their plastron resist the large environmental fluctuations present in nature.

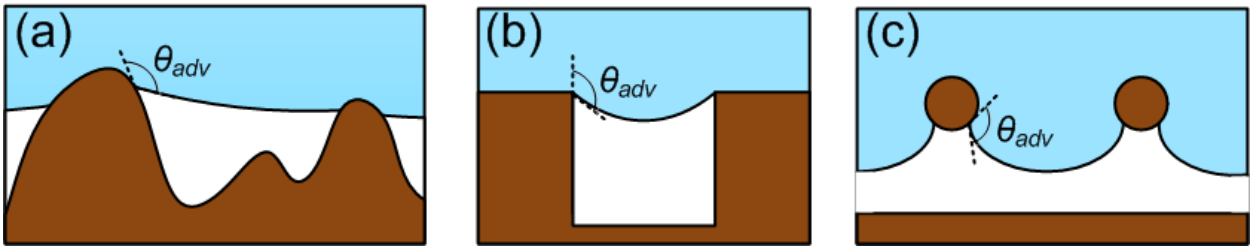

Figure 2-7 Schematic representations of three different SHPo surfaces of same material with different surface topography and corresponding air-water meniscus shape. (a) SHPo surface with random protrusions (e.g., [8]) with slightly convex meniscus can hardly support any hydrostatic pressure unless the spacing is in nanometer scale. (b) Trench structure with reasonable convex meniscus (e.g., this study) can support some hydrostatic pressures with spacing in micrometer scale. (c) Parallel setae with highly convex meniscus (e.g., [13, 18]) and micrometer scale spacing can support more hydrostatic pressure due to their re-entrant shape. In reality, the environmental fluctuations make the air depleted much easier than the theory based on the equilibrium state. As

result, the indefinite retention of the air was observed only when the environmental fluctuation was minimized for (b) (this study) or when the spacing was in nanometer scale for (c) [13, 18].

In summary, we applied a theoretical model to describe the depletion dynamics and re-arranged it to prescribe the stable state of the air trapped in a simple hydrophobic trench under water. Then we verified the model through direct observation of air-water meniscus and experimentally obtained a stable air pocket in the trench. Lifetime of the air pocket was obtained as function of immersion depth with the trench width as a parameter. The infinite lifetime (> 1200 hours) was obtained by minimizing the environmental fluctuations in the experiments. The critical immersion depth, within which the indefinite plastron is possible, was confirmed to depend reciprocally on the trench width. While verifying indefinite plastron can exist as predicted by the theoretical model, this study conversely attests to the delicate fragility of the plastron on SHPo surfaces. To keep a plastron stable under realistic conditions, where environmental parameters would fluctuate significantly, one should use the SHPo surface at a much shallower depth than the theoretical critical immersion depth. Although performed under near thermodynamic equilibrium environment far from realistic conditions, this study nevertheless teaches us (1) that the indefinite SHPo state does exist, (2) how to design SHPo surfaces to retain the air better, and (3) that the indefinite SHPo state would not be possible for many applications unless energetically assisted [17]. In particular for drag reduction, which requires trench width larger than ~20 μm [28], the results indicate long-term (e.g., > days) operations not possible in field conditions unless the immersion is very shallow (e.g., mere centimeters) or the gas is replenished [17].

2.4 References

[1] M. Xu, G. Sun, and C.-J. Kim, "Infinite Lifetime of Underwater Superhydrophobic States," *Physical Review Letters,* vol. 113, 136103, 2014.

[2] M. Xu, G. Sun, and C.-J. Kim, "Wetting dynamics study of underwater superhydrophobic surfaces through direct meniscus visualization," in *Proceedings of the IEEE International Conference on Micro Electro Mechanical Systems*, January 2014, San Francisco, CA, pp. 668-671.

[3] L. Bocquet and E. Lauga, "A Smooth Future?," *Nature Materials,* vol. 10, pp. 334-337, 2011.

[4] C. Lee, C.-H. Choi, and C.-J. Kim, "Structured surfaces for a giant liquid slip," *Physical Review Letters,* vol. 101, 64501, 2008.

[5] R. J. Daniello, N. E. Waterhouse, and J. P. Rothstein, "Drag reduction in turbulent flows over superhydrophobic surfaces," *Physics of Fluids,* vol. 21, 085103, 2009.

[6] E. Karatay, A. S. Haase, C. W. Visser, C. Sun, D. Lohse, P. A. Tsai, *et al.*, "Control of slippage with tunable bubble mattresses," *Proceedings of the National Academy of Sciences of the United States of America,* vol. 110, pp. 8422-8426, 2013.

[7] K. Koch and W. Barthlott, "Superhydrophobic and superhydrophilic plant surfaces: an inspiration for biomimetic materials," *Philosophical Transactions of the Royal Society a-Mathematical Physical and Engineering Sciences,* vol. 367, pp. 1487-1509, 2009.

[8] R. Poetes, K. Holtzmann, K. Franze, and U. Steiner, "Metastable Underwater Superhydrophobicity," *Physical Review Letters,* vol. 105, 166104, 2010.

[9] Y. H. Xue, S. G. Chu, P. Y. Lv, and H. L. Duan, "Importance of Hierarchical Structures in Wetting Stability on Submersed Superhydrophobic Surfaces," *Langmuir,* vol. 28, pp. 9440-9450, 2012.

[10] W.-Y. Sun and C.-J. Kim, "The role of dissolved gas in longevity of Cassie states for immersed superhydrophobic surfaces," in *Proc. IEEE Conf. MEMS*, 2013, Taipei, Taiwan, pp. 397-400.

[11] M. A. Samaha, H. V. Tafreshi, and M. Gad-el-Hak, "Influence of Flow on Longevity of Superhydrophobic Coatings," *Langmuir,* vol. 28, pp. 9759-9766, 2012.

[12] F. O. Ochanda, M. A. Samaha, H. V. Tafreshi, G. C. Tepper, and M. Gad-el-Hak, "Salinity effects on the degree of hydrophobicity and longevity for superhydrophobic fibrous coatings," *Journal of Applied Polymer Science,* vol. 124, pp. 5021-5026, 2012.

[13] A. Balmert, H. Florian Bohn, P. Ditsche‐Kuru, and W. Barthlott, "Dry under water: Comparative morphology and functional aspects of air‐retaining insect surfaces," *Journal of Morphology,* vol. 272, pp. 442-451, 2011.

[14] M. A. Samaha, H. V. Tafreshi, and M. Gad-el-Hak, "Sustainability of superhydrophobicity under pressure," *Physics of Fluids,* vol. 24, 112103, 2012.

[15] M. S. Bobji, S. V. Kumar, A. Asthana, and R. N. Govardhan, "Underwater Sustainability of the "Cassie" State of Wetting," *Langmuir,* vol. 25, pp. 12120-12126, 2009.

[16] P. Lv, Y. Xue, Y. Shi, H. Lin, and H. Duan, "Metastable States and Wetting Transition of Submerged Superhydrophobic Structures," *Physical Review Letters,* vol. 112, 196101, 2014.

[17] C. Lee and C.-J. Kim, "Underwater Restoration and Retention of Gases on Superhydrophobic Surfaces for Drag Reduction," *Physical Review Letters,* vol. 106, 14502, 2011.

[18] M. Flynn and J. W. Bush, "Underwater breathing: the mechanics of plastron respiration," *Journal of Fluid Mechanics,* vol. 608, pp. 275-296, 2008.

[19] B. Emami, A. Hemeda, M. Amrei, A. Luzar, M. Gad-el-Hak, and H. V. Tafreshi, "Predicting longevity of submerged superhydrophobic surfaces with parallel grooves," *Physics of Fluids,* vol. 25, 062108, 2013.

[20] R. Picknett and R. Bexon, "The evaporation of sessile or pendant drops in still air," *Journal of Colloid and Interface Science,* vol. 61, pp. 336-350, 1977.

[21] E. L. Cussler, *Diffusion: mass transfer in fluid systems*: Cambridge university press, 2009.

[22] P. B. Duncan and D. Needham, "Test of the Epstein-Plesset model for gas microparticle dissolution in aqueous media: Effect of surface tension and gas undersaturation in solution," *Langmuir,* vol. 20, pp. 2567-2578, 2004.

[23] T. Enns, P. F. Scholander, and E. D. Bradstreet, "Effect of Hydrostatic Pressure on Gases Dissolved in Water," *The Journal of Physical Chemistry,* vol. 69, pp. 389-91, 1965.

[24] P. Papadopoulos, L. Mammen, X. Deng, D. Vollmer, and H.-J. Butt, "How superhydrophobicity breaks down," *Proceedings of the National Academy of Sciences,* vol. 110, pp. 3254-3258, 2013.

[25] M. Reyssat, J. M. Yeomans, and D. Quere, "Impalement of fakir drops," *Europhys. Lett.,* vol. 81, 26606, 2008.

[26] H. Rathgen and F. Mugele, "Microscopic shape and contact angle measurement at a superhydrophobic surface," *Faraday Discussions,* vol. 146, pp. 49-56, 2010.

[27] B. Woolford, J. Prince, D. Maynes, and B. W. Webb, "Particle image velocimetry characterization of turbulent channel flow with rib patterned superhydrophobic walls," *Physics of Fluids,* vol. 21, 085106, 2009.

[28] H. Park, G. Sun, and C.-J. Kim, "Superhydrophobic turbulent drag reduction as a function of surface grating parameters," *Journal of Fluid Mechanics,* vol. 747, pp. 722-734, 2014.

[29] E. Aljallis, M. A. Sarshar, R. Datla, V. Sikka, A. Jones, and C. H. Choi, "Experimental study of skin friction drag reduction on superhydrophobic flat plates in high Reynolds number boundary layer flow," *Physics of Fluids,* vol. 25, 025103, 2013.

[30] C.-H. Choi and C.-J. Kim, "Large slip of aqueous liquid flow over a nanoengineered superhydrophobic surface," *Physical Review Letters,* vol. 96, 066001, 2006.

[31] F. Scholz, *Electroanalytical methods: guide to experiments and applications*: Springer, 2009.

[32] R. D. Deegan, O. Bakajin, T. F. Dupont, G. Huber, S. R. Nagel, and T. A. Witten, "Capillary Flow as the Cause of Ring Stains from Dried Liquid Drops," *Nature,* vol. 389, pp. 827-828, 1997.

[33] K. N. Ren, W. Dai, J. H. Zhou, J. Su, and H. K. Wu, "Whole-Teflon microfluidic chips," *Proceedings of the National Academy of Sciences of the United States of America,* vol. 108, pp. 8162-8166, 2011.

[34] W. Feast, H. Munro, and R. W. Richards, *Polymer surfaces and interfaces II* vol. 2: Wiley, 1993.

[35] M. J. Madou, *Fundamentals of microfabrication: the science of miniaturization*: CRC press, 2002.

[36] B. Kobrin, J. Chin, and W. Ashurst, "Vapor deposition of composite organic-Inorganic films," in *World Tribology Congress III*, 2005, Washington, D.C., USA, pp. 533-535.

Chapter 3 Shear Stress Sensor Development

3.1 Introduction

3.1.1 Fluid Shear Stress Measurement Methods

Shear stress measurement is a crucial topic in fluid mechanics. It not only provides insights into complex flow phenomena which helps the design of marine vessels or aircraft, but also may serve as a feedback for flow-control [1]. For our study, shear stress measurement is needed to quantify the drag reducing ability of superhydrophobic (SHPo) surfaces under different flow conditions. There are two broad approaches for shear stress measurement: indirect measurement and direct measurement. Indirect measurement obtains the shear stress value by measuring certain properties of the flow (e.g., velocity, pressure, etc.) and convert it into shear stress value. Indirect measurement methods are usually easier to conduct, but often rely on certain theoretical models and associated assumptions, which might be inaccurate if the flow is complex. Well-known indirect shear stress measurement methods include pressure drop [2], thermal sensors [3], micro-pillar sensors [4], laser Doppler velocimetry (LDV) and particle imaging velocimetry (PIV) [5]. On the contrary, direct measurement obtains the momentum transfer, which is the shear force at the wall. It usually includes a floating element flush-mounted into the wall and displaced by the wall-bounded flow. The force is typically obtained by measuring structure deflection (i.e., floating element), bending or twisting capacitively [6, 7], piezoresistively [8, 9], or optically [10, 11]. Direct measurement methods do not require prior knowledge of the flow conditions, which has great advantages in complex flows.

Among the direct measurement methods, micro-electro-mechanical-systems (MEMS)-based shear stress sensors are promising for shear stress measurement because of its compactness, monolithic structure, high sensitivity and accuracy, and high spatial and temporal resolution [12, 13]. However, the size of the floating elements is limited to a few centimeters by the wafer used for MEMS fabrication. Also, changing sizes of the floating element requires new sets of photolithography masks, which are not cheap, making MEMS sensors usually too expensive for small-batch and customized measurement tasks. Moreover, MEMS sensors are usually not robust when subject to water or particle impingement, and are thus constrained by the packaging technique. Finally, MEMS devices usually use silicon for the mechanical structure, which is too brittle for applications in harsh environments, as well as for frequent sample replacement.

Another well-known direct measurement method is single pivot shear stress senor using piezoelectric sensor to characterize the pivot deflection [9, 14, 15]. This type of sensor uses a single pivot structure that deflects under shear force. Piezoelectric sensors are usually used to measure the deflection and quantify the shear force. However, this type of sensor is usually assembled of parts instead of monolithically fabricated. The need to assemble the device increases the chance of floating element misalignment and increases the cost. Due to the nature of piezoelectrical sensing mechanisms, the single-pivot sensor is sensitive to temperature and fluid pressure change and usually needs calibration prior to testing [14]. Since the pivot is perpendicular to the shear plane, the single pivot sensors are usually thick compared with other in-plane sensors, which employ beams deflecting in the same plane as the shear plane. This thick profile is problematic for some applications that require a low profile (e.g., airplane wing, ship hull).

3.1.2 Shear Stress Measurement for SHPo Surfaces in Turbulent Flows

Many different methods have been applied, including both indirect and direct methods, to measure the skin friction on SHPo surfaces. The measurement techniques for the drag on SHPo surface in laminar flow has been well reviewed [16]. The methods include pressure drop measurement, micro-PIV, rheometer and built-in strain gauge. However, in turbulent flow, the measurement is more difficult. Firstly, the turbulent flow is more complicated in nature compared with laminar flow. It includes secondary structures including streaks, eddies and vortices [17]. The interaction between SHPo surface and these structures might also play a role in reducing skin friction drag [18, 19]. The turbulent boundary layer (TBL) is also more complicated with a thin viscous sublayer that is usually only several microns thick. Since indirect methods rely on assumptions and theories of the flow conditions, complicated flow conditions make the measurement more difficult. Secondly, the testing environment is more violent (e.g., larger pressure fluctuation) than laminar flows. This harsh condition is a challenge for the robustness of the sensor. Lastly, many sensing mechanisms require special apparatus, which are often not applicable for large flow facilities. For example, towing tank is one of the most useful flow facilities testing the flow conditions resembling marine vessels. However, since the test is in open water with limited space, shear stress measurement methods such as pressure drop, LDV/PIV, and rheometer are not applicable.

In recent studies on SHPo surface turbulent drag reduction, methods similar to those used in laminar flows measurement were used. Pressure drop measurement has been used to quantify the drag reduction of SHPo surface turbulent drag reduction in small channels [2]. Another indirect measurement method used to measure shear stress on SHPo surface is micro-PIV [20-24]. In these methods, liquid velocity profile is visualized by tracing fluorescent particles dispersed in water. This method not only detects the shear stress at the wall but also provides the velocity profile near SHPo surface to investigate the influence of SHPo surface on flow structures. However, the

measurement of PIV is limited by determination of the wall location and the interaction of the particles with the wall. The accuracy becomes even more substantial for turbulent flows, which have a thinner boundary layer compared with laminar flows. Moreover, some study [22] using micro-PIV found no velocity increase near the wall, indicating no drag reduction. However, the Reynolds shear stress was decreased at the same time, indicating drag reduction. The discrepancy might be caused by limited resolution and uncertainty on air-water meniscus position, especially for SHPo surface with random structures.

As a direct measurement method, commercial rheometer has shown to be a convenient tool when measuring shear stress of SHPo surface [25] including turbulent flows [26-28]. In rheometric measurement, two parts usually rotate relative to each other with one coated with a SHPo surface. Then the shear stress is measured by measuring the torque applied to rotate one part. This relatively simple and straightforward method is limited by the flow condition it can create and measure. The Taylor-Couette flow created in rheometer is essentially different from boundary layer flows of the marine vessels. MEMS sensor with floating plates for direct measurement of SHPo drag reduction has been used successfully in turbulent flows in a small water tunnel [29, 30]. The monolithic shear stress sensor has two floating plates in parallel with one plate fabricated with micro-gratings and coated with Teflon and the other plate left smooth and coated with Teflon. The displacement of the two floating plates was measured optically using high speed camera looking at micro-scales etched onto the back of the sensor. This sensor offered high measurement accuracy and fidelity. However, the silicon micro-beams were fragile [13] and the instrumentation for the optical reading was bulky.

Finally, a widely used method, especially for large flow facility, is piezoelectric deflection senor [14, 31, 32]. In this method, the floating element is connected to the substrate using either a single

pivot [14] or multiple ones [31, 32]. The setups were usually made of metal, which is more robust for high Reynolds number experiments at large flow facilities. However, the lack of accuracy usually requires the samples to be large (e.g., tens of centimeters) [31, 32], making the sample preparation difficult and time-consuming. Even with improved accuracy, the instability against pressure and temperature fluctuation require precise water pressure and temperature control [14].

Table 3-1 Methods used to measure friction drag of SHPo surface in turbulent flows

	Methods	**Pros**	**Cons**
Indirect	Pressure drop	Simple setup	• Only channel flow • Low accuracy
	Particle image velocimetry (PIV)	• TBL flow capability • Visualization of velocity profile	• Bulky & complex • Not in open water • Large uncertainty
	Rheometer	• Simple setup • High accuracy	• Only Taylor-Couette flow
Direct	MEMS floating element (optical)	• High accuracy • TBL flow capability	• Bulky optical setup • Fragile structure • Size limit • Fabrication challenge
	Pivot sensor (piezoelectric)	• High accuracy • TBL flow capability • Robust structure	• Assembly difficulty • Temperature& pressure sensitivity

In this study, we first developed a MEMS floating plate sensor similar to [13] but with improved design and fabrication process. Based on the design of the MEMS shear stress sensor, we further developed a compact whole-metal shear stress sensor. The robust sensor is targeted for measurement in different flow facilities (e.g., small/large water tunnel, towing tank) and field test on boats. Meanwhile, it can also be applied to aerodynamic tests. It has several advantages over the MEMS sensor and single-pivot senor for SHPo surface shear stress measurement:

(1) The sensor is made monolithically out of metal (e.g., aluminum, stainless steel, titanium alloy). The use of metal makes the deflection beams structurally robust and allows repeated attachment and detachment of the surface samples. The monolithic construction decreases the chance of misalignment and reduced the assembly cost.

(2) The sensor uses optical measurement mechanism, which provides an ultra-high accuracy (i.e., up to 2 nm displacement) and robustness against environmental parameters change (e.g., pressure, temperature).

(3) The sensor has a compact size and a low profile to be compatible with different testing facilities (e.g., water tunnel, towing tank, boat, etc.).

(4) The sensor fabrication cost is low compared with MEMS sensors and scalable for mass production. Meanwhile, the fabrication process is also cost-friendly for small quantity and customized needs.

3.2 MEMS Shear Stress Sensor

3.2.1 Motivation

The floating plate MEMS shear stress sensor developed in [13] is one of the first MEMS shear stress sensors that can directly measure drag reduction of SHPo surfaces in turbulent flows. However, the through-wafer etching from both sides makes the fabrication process complicated and increased the chance of microbeams breaking. Also, the relative small area of the floating plate requires thin and delicate beams for enough resolution but also increased the chance of beam breaking during device releasing. We further improved the sensor design to enlarge the shear force measurement area with larger shear force, so thicker beams could be used. Moreover, the

fabrication process was also improved so that only single-side etching is needed, greatly simplifies the fabrication process and reduces the chance of beam breaking.

3.2.2 Sensor Principle and Design

The drag reduction of SHPo surface relative to smooth surface is measured by reading how much the SHPo surface is displaced compared with the smooth surface. The two sides of the floating plate on this sensor were made SHPo and smooth respectively, as shown in Figure 3-1. For both SHPo and smooth surfaces, they were suspended by identical springs and considered to experience the same flow condition. If the two plates displace in different amounts, the difference is solely due to the difference in the skin-friction drag acting on their surfaces. Figure 3-1 schematically illustrates how to measure the shear stress using the proposed shear sensor in the flow test. After finishing measuring the shear stress on one side (e.g., SHPo surface as shown in the figure), the sensor is flipped and the shear stress of the other side is measured to calculate the relative drag reduction. The sensor (2.7 mm × 2.7mm × 0.3 mm) includes one floating plate suspended by folded-flexure beams. The beams are designed to be narrow (50 μm) but thick (300 μm) so the sensor is flexible in the streamwise direction but stiff in all other directions, making it sensitive to the streamwise shear stress but insensitive to forces in spanwise (transverse to the flow) and out-of-plane (vertical to the wall) directions. With flow passing the sensor, the floating plate will displace in streamwise direction. Since air was filled underneath the sensor plate, as shown in Figure 3-1(b), there is no significant shear force from the backside. The drag reduction can be measured by comparing the displacement of the floating plate using both sides, since the displacements are proportional to the shear force with same spring constant. In order to accurately measure the displacement in microscale, micro-rulers are etched onto the sensor frame. The rulers

are fabricated to both sides of the sensor so the displacement can be measured through a transparent window.

To determine the detailed beam dimension, several constraints should be considered: (1) flow condition (2) optical displacement measurement resolution (3) limitation on fabrication. The target flow condition of this sensor is TBL flow with Reynolds number $\mathrm{Re}_x \sim 5\times10^5$ and frictional Reynolds number $\mathrm{Re}_\tau = u_\tau \delta / \nu \sim 650$. This Reynolds number is the highest Reynolds number that can be obtained with our in-house water tunnel. For other flow conditions, new beam dimensions need to be designed. Firstly, for the floating plate size, the floating plate area should be large enough to host multiple near-wall turbulence vortices. These turbulent structures are known to be of nondimensionalized diameter $D^+ = Du_\tau / \nu \sim 100$ and apart from each other $Z^+ = Zu_\tau / \upsilon \sim 30-50$ [33]. Under current flow condition, the diameter $D \sim 1.8$ mm and the distance $Z \sim 0.9$mm. So, the current size (21 mm × 21 mm) can host multiple turbulence vortices. Secondly, for the spring constant design, the total shear force and the optical measurement resolution need to be considered. Under this flow condition, the shear stress on the smooth surface is estimated to be around 3 Pa [34, 35]. So the total shear force is around 1300 μN for smooth surface considering the total area. The optical measurement resolution is about 5 μm. With that resolution, we would like to have the force measurement resolution of ~ 130 μN, 10% of the total force. Therefore, the spring constant is about 130 μN / 5 μm = 25 N/m. Based on this spring constant, the total size of the sensor and the fabrication capability of UCLA Nanoelectronics Research Facility (Nanolab), we designed folded beam that is 50 μm wide, 16 mm long (but folded into two 8 mm sections) and 300 μm thick.

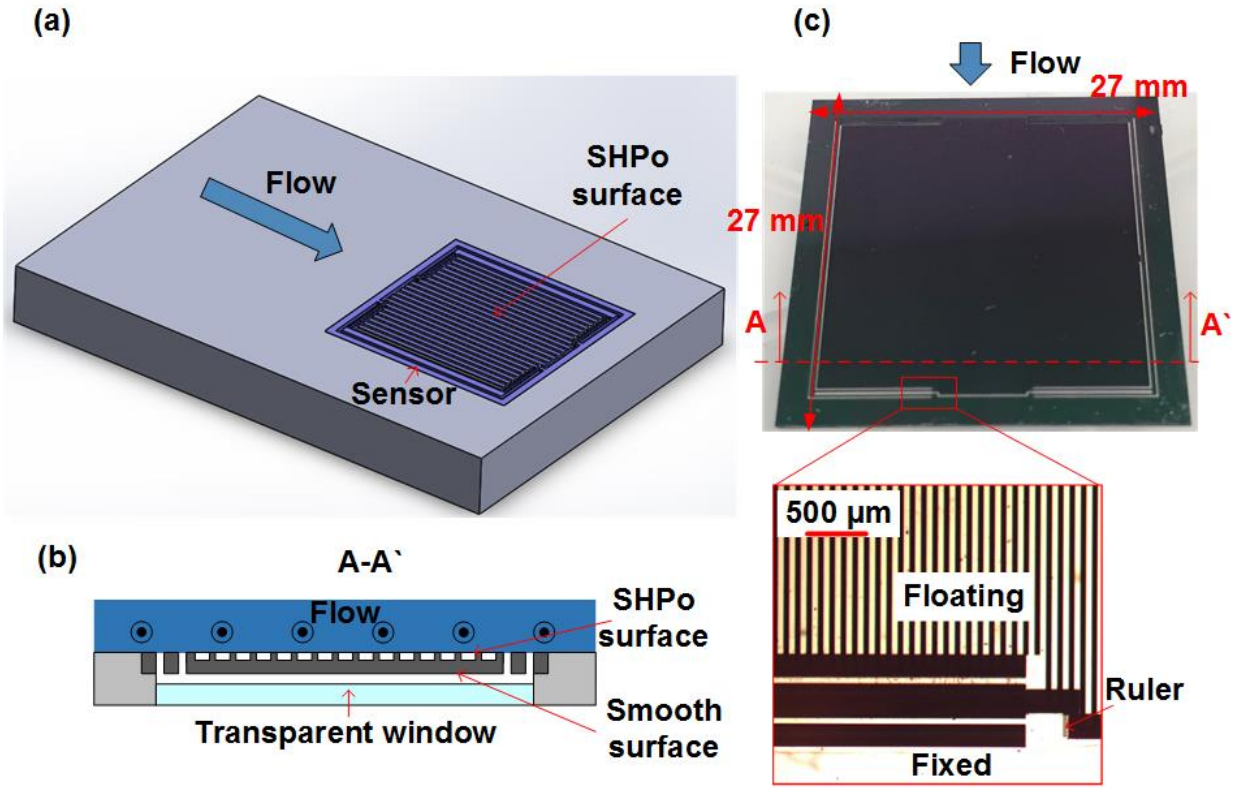

Figure 3-1 Schematic drawing of the MEMS shear stress sensor in flow test. (a) 3D view with sensor flush-mounted on the wall for flow test. (b) Cross section view of the sensor assembly (c) Picture of the sensor, beams and ruler. For this sensor, the shear on the smooth surface is obtained by flipping the silicon die to expose the bottom (smooth) surface to the flow.

3.2.3 Sensor Fabrication

3.2.3.1 Sensor Etching

This shear stress sensor was monolithically fabricated from on silicon wafer using one-side through-wafer deep reactive ion etching (DRIE), as illustrated in Figure 3-2. A double-sided polished 300 µm silicon wafer is used. Firstly, the ruler on backside is defined by a 5 min RIE etching (Technics RIE, SF6, 100 mTorr, 300 W) with a ~1.5 µm-thick photoresist AZ5214 as the etching mask. The etching depth was measured to be ~750 nm, which can vary as long as the ruler

is visible under microscope. The photoresist mask and any polymer residual from the RIE process were then removed by O_2 plasma (300 mTorr at 300 W) for 3 mins, followed by a Pirahna cleaning (98 wt.% H_2SO_4 : 30 wt.% H_2O_2 = 4:1) for 10 mins and BOE (Buffered oxide etch) cleaning for 5 mins. Secondly, the 300 µm wafer was flipped over and a ~1.6 µm silicon dioxide was deposited on the front side using PECVD. The SHPo grating oxide mask were then defined by a 4.5 min RIE etching with a ~1.5 µm-thick photoresist AZ5214 as the etching mask. The photoresist mask and any polymer residual from the RIE process were then removed using the same process as the first step. Then, the suspended beams as well as the front ruler was defined by a 35 min DRIE etching (Unaxis Versaline Series FDRIE III) with a 7.5 µm-thick photoresist AZ4620 as the etching mask. The etching depth was time-controlled and measured to be 250±5 µm, followed by the same cleaning process as previous step to remove the photoresist mask and any polymer residual from the DRIE process. Individual sensor was then diced off the wafer (four sensors per wafer) and was mounted on a 500 µm thick carrier wafer using cool grease (Tech Spray Heatsink Compound) as an adhesive layer. Another DRIE process was performed to define the floating plate and beam, as well as to create ~50 µm tall micro-gratings for the SHPo surfaces. This second DRIE step require careful etching time control near completion to minimize over-etching. After etching through, the device along with the carrier wafer were immersed in Baker ALEG 350 solution at 100 °C for 2 hrs to strip off the photoresist and DRIE-induced polymer residues, disperse the cool grease, and thus release the device from the carrier wafer. After sensor cleaning, it was dip coated by 0.2 wt.% Teflon AF1600 and baked at 165 °C for 15 mins and 330 °C for 30 mins to make the smooth side hydrophobic and the etched side SHPo.

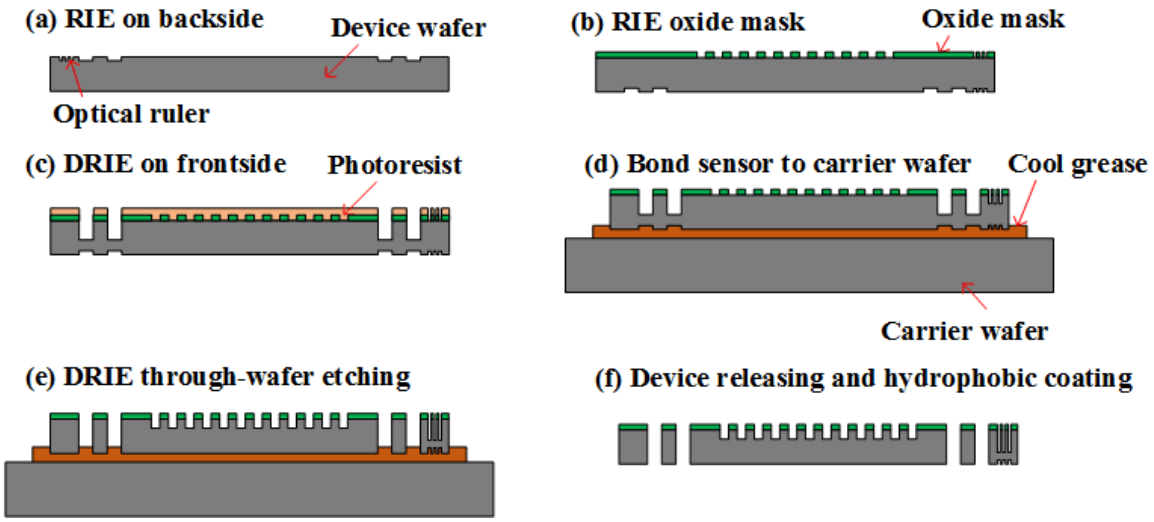

Figure 3-2 Fabrication of the MEMS shear sensor. (a) RIE on backside defines the optical ruler (b) The device wafer is flipped and oxide mask is defined. (c) DRIE etching the beam structure (d) Bond the device wafer to carrier wafer. (e) DRIE etching through the beam structure and define the grating structure. (f) Device releasing.

In [13], one problem with DRIE of flexure beams was the undercut of the beam during DRIE leading to nonuniform beam. The beam width may vary by over 10 µm with total width of 15 µm [13]. The beams were then very easy to break during the releasing or testing stage at the "bottleneck" part, which is only several microns. Also, the two sets of beams supporting two floating plate might be different due to DRIE etching nonuniformity. A dummy structure to reduce undercut was used in [13] to reduce beam undercut. However, the size and placement of dummy structure varies with different processing equipment, geometric details of the sensor and other process variations. In this updated design, since the beam are 50 µm wide, the 10 µm undercut won`t lead to beak breakage. Also, both smooth and SHPo surface share exactly the same beam, the beam nonuniformity won`t cause any measurement error.

Another problem regarding the fabrication process in [13] was the second DRIE process. Firstly, the etching time needed to be very precisely controlled or the beam will be etched from the top. Secondly, the air trapped in the structure etched in the first DRIE from the other side may get heated up and pop the sensor from the carrier wafer. However, in this updated design, since structures were etched only from one side, a little over-etching won`t significantly change the beam. Also, there are no voids between the sensor and the carrier beam so the cool grease could conduct heat very well during DRIE.

3.2.3.2 Device Releasing

As discussed in [13], the releasing process of the device is one of the most critical steps in the whole process. Due to the delicate 15 μm-wide beam, viscous and heavy solvent (Baker ALEG series) and liquid surface tension, the beams are very easy to break during releasing. With the updated design, firstly, since thicker beams are used, the beams are much robust than those in [13]. Moreover, we found most of the beams in [13] broke at the very last step when it was pulled out of water and the large surface tension of water usually caused the beam to "stick" onto the sensor frame. To solve this problem and increase yield, we added another step of acetone bath. After the ALEG and water bath, the sensor was transferred to an acetone bath while still immersed in water in a small container. Then the container was taken out of the acetone bath with the sensor immersed in acetone. The acetone evaporated and left a dry sensor sample. With this method, mechanical shock and vibrationwere minimized. Moreover, the low surface tension of acetone solved the "sticking" problem so the beams were much less likely to break.

3.2.4 Sensor Characterization and Verification

The water tunnel and sensor holder used for this sensor were the same as the setup described in [30], as shown in Figure 3-3. The water tunnel has a test section of 610 mm × 50 mm × 50 mm in the streamwise, vertical and spanwise directions, respectively. The flow condition at the sensor location TBL flow with frictional Reynolds number $\mathrm{Re}_\tau = u_\tau \delta / \nu \sim 650$, which roughly corresponds to $\mathrm{Re}_x \sim 5\times10^5$, an increase from [30]. The sensor was mounted onto a sensor holder and made flush to the top inner wall of the water tunnel. A high-speed camera (Vision Research Phantom V7.2) together with a light source and a microscopic lens (×20) was used to record the displacement relative to the ruler at 500 frames per second (f.p.s). The recorded displacements were analyzed to obtain the time-average displacement with ImageJ software. Both the SHPo surface side and the smooth side of the floating plate were tested at the same flow speed.

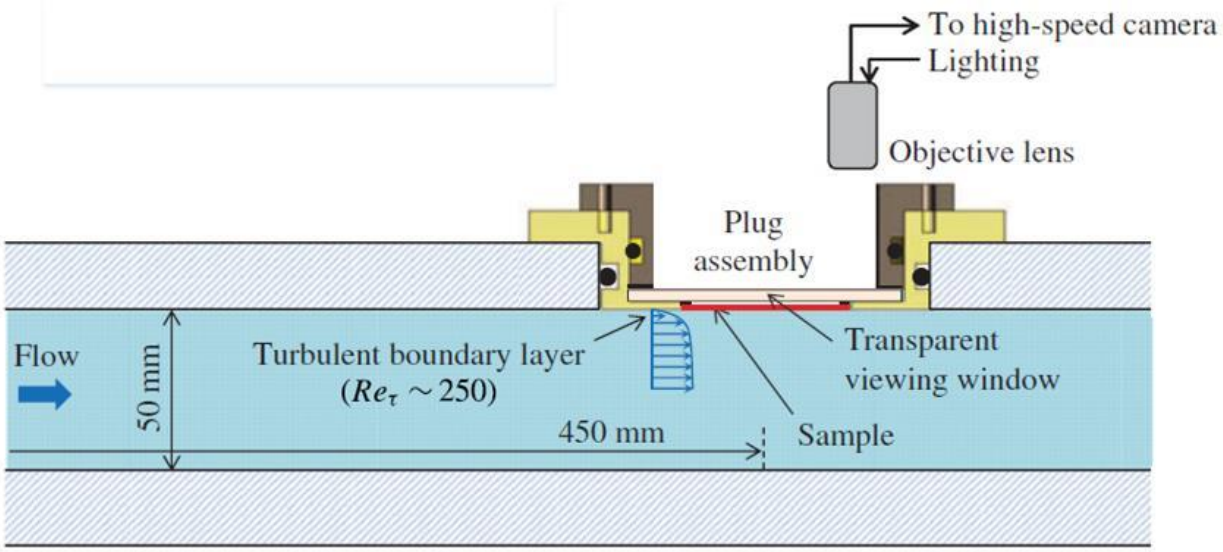

Figure 3-3 Cross section view of the low-speed water tunnel and the testing setup. [30]

Figure 3-4(a) shows the temporal variation of displacement measured for SHPo surface and smooth surface and Figure 3-4 (b) shows the drag ratio compared to previous tests. As shown in the figure, the SHPo surface of 100 μm pitch and 50 % gas fraction shows a distinctively smaller

displacement that the smooth surface. After averaging the displacement data for bother surface, the drag reduction is calculated to be ~48%. This sensor successfully confirmed the drag reduction effect of SHPo surfaces in TBL flows and the drag decreased as Reynolds number increased when comparing to result in [30]. Moreover, the improved design and simplified fabrication process compared with direct shear stress sensors used in [13, 30] made it easier to fabricate multiple sensors with different beam designs to measure the SHPo surface drag reduction in multiple flow conditions.

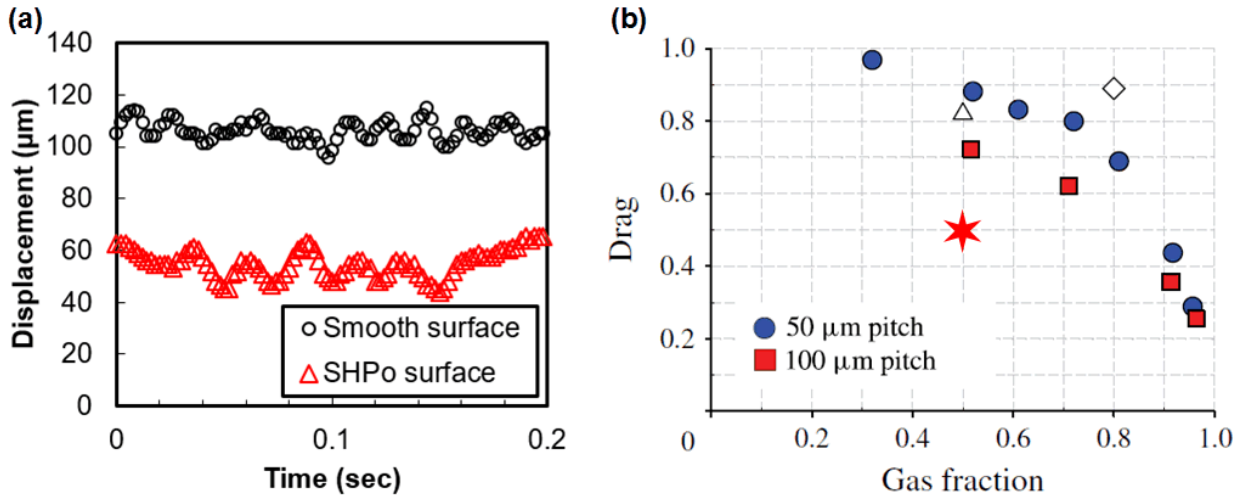

Figure 3-4 Drag reduction results using MEMS shear sensor. (a) Displacement of both SHPo and smooth surface of current sensor at $Re_\tau \sim 650$. (b) Drag ratio of current test (✶, 100 μm pitch) compared to previous tests: ■ and ●, $Re_\tau \sim 250$ [30]; △, 60 μm pitch, $Re_\tau \sim 180$ [2]; ◇, 40 μm pitch, $Re_\tau \sim 100$ [24].

3.3 Monolithic Metal Shear Stress Sensor

3.3.1 Motivation

Even though the updated design and fabrication process of the MEMS shear sensor made it more attractive for SHPo surface drag reduction measurement, it still retained several limitations when applied to open water with high Reynolds number, which is the application environment of the SHPo surface for drag reduction:

(1) Size limitation: To better quantify the drag reduction effect of SHPo or other surfaces, large area is preferred since the boundary layer changes when the flow just meets the SHPo surface and needs certain distance to reach a stable state [36-38]. Also, the eventual application is to cover the entire underwater part of the marine vessel with SHPo surfaces. However, for silicon-based MEMS shear sensors, the sensor size is restricted by the size of the wafer processed by lithography and DRIE etching. Moreover, the wafer thickness limits the beam height, which is important to prevent displacement vertical to sensor surface that will introduce a measurement error.

(2) Packaging limitation: The MEMS shear sensor in [13,28] and here used a bulky high speed camera and objective lens system, which makes the sensor system too bulky for ship hull or towing plate test. Moreover, the limitation on the optical resolution with the high-speed camera (~ 5 μm) requires large displacement of the floating plate to ensure measurement accuracy. However, the large gap leads to more disturbance to the boundary layer of the flow.

(3) Incapability to attach samples: Due to the material property of silicon material and the thin beam used in MEMS sensor, it was very hard to attach and detach sample surfaces on and from the floating plate without breaking the beams. One sensor with certain beam design could be used for only certain flow conditions with one type of SHPo surfaces. In order to

test new type of SHPo surface or under new flow conditions, a new device needed to be fabricated using a new photomask, both of which are costly and time consuming.

To overcome the above shortcomings and allow testing large area SHPo surface in open water (e.g., towing tank, boat in the ocean), a novel direct shear sensor is designed and developed. The new sensor has the following characteristics:

(1) Flexible in size. Since the sensor is fabricated out of a metal plate, instead of silicon wafer, using wire electrical discharge machining (EDM), the size of the floating plate is not limited. It could be large or small depending on the application.

(2) Low profile. The sensor uses an optical method to measure floating plate displacement, making it robust against pressure or temperature change. However, different from the MEMS sensor discussed above, it uses a diffraction-based optical encoder that is compact and low profile (only 6 mm tall) and can reach high resolution up to 2 nm. With no need of the objective lens or the high-speed camera, the sensor system could be designed to be compact and low profile so it can be incorporated into plates or ship hull for open water test.

(3) Capability to attach samples. Using metal for the beams with much higher spring constant, the beams are much more robust mechanically than the silicon beams used in the MEMS shear sensor discussed above. So different kinds of customized samples could be attached onto the floating plate repeatedly to measure the shear stress.

(4) High Resolution and robustness. With the optical encoder have resolution up to 2 nm, the novel shear stress sensor could still detect small shear force with relatively larger beam spring constant compared with previous MEMS sensors. The large spring constant makes the sensor more robust.

(5) Low cost. The novel manufacturing process developed for this shear stress sensor greatly reduced the cost for customized sensors, as well as processed the potential for mass manufacturing.

Although the novel shear stress sensor is designed for measuring shear stress on SHPo surface, it can also be used the measure the shear stress on other surfaces under difference environments and flow conditions. Comparison to other commercial shear stress sensors will be further discussed in the Summary section.

3.3.2 Sensor Principle and Design

3.3.2.1 Sensing Principle

As shown in Figure 3-5, the shear sensor has one or two floating element suspended by folded beams, similar as the MEMS shear senor discussed before [29]except it is made monolithically from a metal plate (e.g., aluminum alloy, titanium alloy). For non-uniform flow field, single plate sensor (Figure 3-5(a)) was used and tested twice with smooth surface and SHPo surface with the same flow speed [14, 32]. The measurement is accurate as long as the flow conditions are controlled well for both tests. For uniform flow field like water tunnel, a dual plate design (Figure 3-5(b)) was used similar to [13, 30]. The two plates are designed to be the same except with different surfaces attached onto them. The beams suspending the plates are designed to be identical and both spring constants will be calibrated after manufacturing. The two plates are also expected to experience the same flow condition if the flow field is relatively uniform since the measurement takes place at the same time.

Figure 3-5 (a)(d) schematically illustrates the structure of the shear stress sensor. The sensor includes a floating plate suspended by folded-flexure beams. The size of the floating plate and the

beams are flexible based on the SHPo and smooth sample size. The testing samples are fixed onto the floating plates using screws. A cover plate is also fixed onto the sensor to ensure the flushness of the top surface of the sample to the rest of the surfaces, which is critical to minimize measurement error [14, 39]. Also, the gap between cover plate and the sample surfaces are minimized using feeler gauge to further reduce measurement error. Furthermore, the beams are fabricated with high aspect ratio to ensure that the sensor is flexible in streamwise direction but rigid in all other directions. As a result, the sensor is only sensitive to shear force in the streamwise (parallel to flow) direction and insensitive to forces in both the spanwise (traverse to flow) and out-of-plane (vertical from the wall) directions.

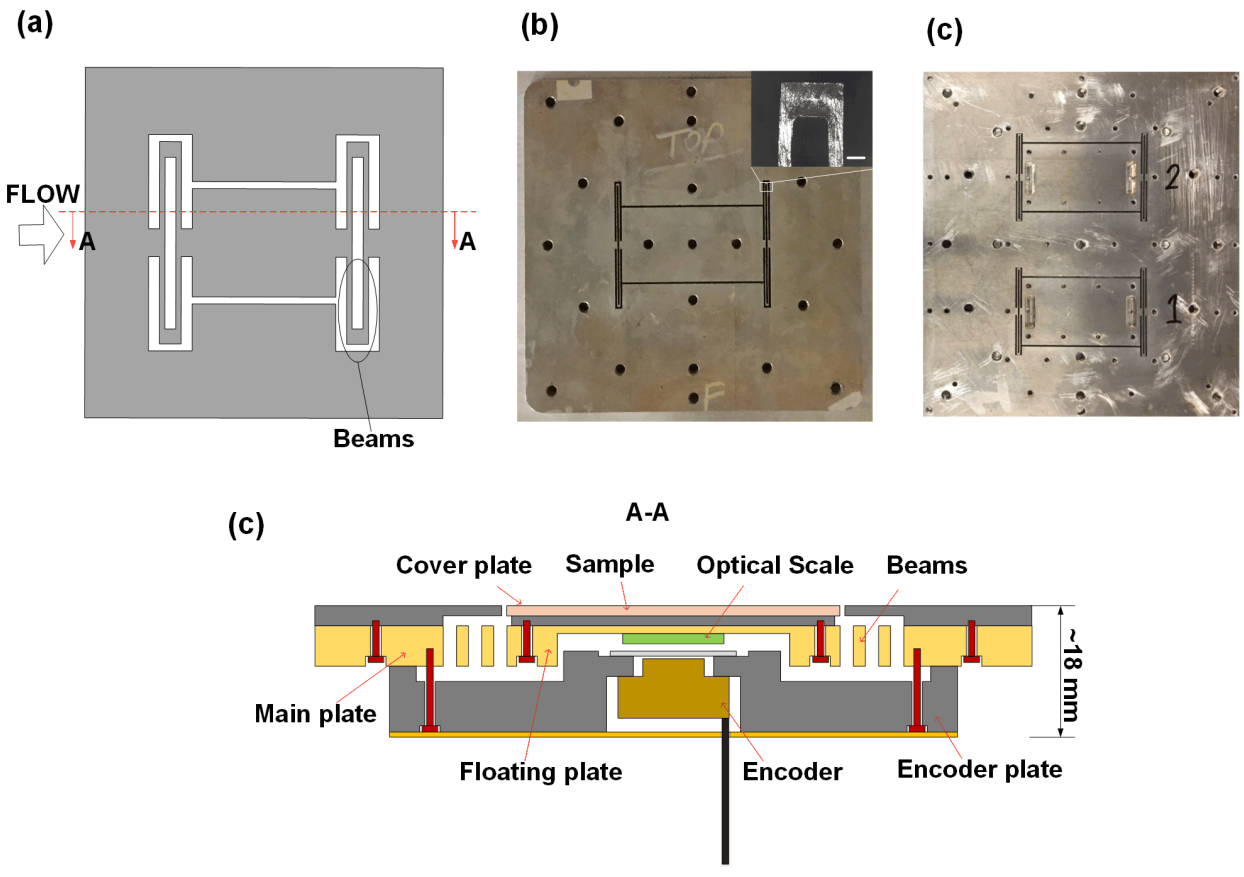

Figure 3-5 Schematic drawing of the monolithic metal shear sensor. (a) Schematic top view of the shear stress sensor. (b) Top view picture of single-plate shear stress sensor and the folded beams with scale bar indicating 500 μm. (c) Top view picture of double-plate shear stress sensor. (d) Schematic cross section view of the shear stress sensor.

Knowing spring constant of the beam after sensor characterization, which is discussed in 3.3.4, the shear stress can be directly measured by reading the displacement of the plates. As shown in Figure 3-5(d), an optical encoder (M2000 linear encoder, Celera Motion Inc.) is used to measure the displacement. The optical scale is attached onto the back of the floating plate while an encoder head is sealed into the encoder holder and fixed to the substrate. The optical encoder shines laser onto the scale and sense the change in diffraction patterns from the reflected lights with resolution as high as 78 nm (2 nm for advanced models of encoder). The encoder holder is attached to the sensor plate to ensure the alignment requirements between the encoder head and the optical scale, as well as seal encoder.

3.3.2.2 Sensor Geometry Design

In designing the sensor dimension, flow condition, encoder resolution, manufacturing limitation and resonance frequency should be considered. The first step is to determine the spring constant, which should be designed to ensure that (1) the actual displacement is much bigger than the encoder resolution, (2) the displacement should be less than a few viscous lengths to reduce disturbance to the boundary layer [40] (3) the resonant frequency is designed to be away from the environmental noise frequency to avoid resonance.

Firstly, the spring constant of the folded beams needs to be designed to meet the requirement (1) and (2). The designing process is similar as previous MEMS sensor, as discussed in Section 3.2.2.

For example, for target TBL flow at Re_x of $O(10^6)$, which is the range for small boat, the shear stress τ is estimated to be at the level of $O(10^{-3} Pa)$. We prefer the SHPo sample to be as large as possible to reduce "entrance effect"[36] and better represent large area application on large marine vessels. Due to current SHPo surface fabrication limitation, the sample size is about 4 cm x 7 cm. The encoder resolution is $O(100nm)$, pre-defined by the manufacturer. Using Hook`s law, the spring constant should be $O(1000N/m)$.

Meanwhile, since this sensor is designed for applications with large vibration (e.g., large water tunnel) and more violent turbulent flow, resonant frequency needs to be considered to avoid sensor resonance. Different from a simple one-spring system where the displacement is between the moving element and the wall, here the displacement is between the floating plate and the encoder holder, which is not fixed to wall and might also vibrate. Figure 3-6 (a) showed the vibration model where m_0 is the encoder holder, m_1 is the floating plate, x(t) is the relative distance between encoder holder and floating plate, d(t) is the relative distance between encoder holder and the wall.

The motion equation on the floating plate is:

$$m(x+d)'' + cx' + kx = 0 \tag{4-1}$$

Using Laplace transform:

$$(ms^2 + cs + k)X(s) + ms^2 P(s) = 0 \tag{4-2}$$

So the transfer function:

$$TR = \left| \frac{X(s)}{P(s)} \right| = \frac{m\omega^2}{\sqrt{(k - m\omega^2)^2 + c^2\omega^2}} \tag{4-3}$$

With natural frequency $\omega_n = \sqrt{k/m}$ and damping ratio $\xi = c/(2m\omega_n)$, the transfer function is then:

$$TR = \frac{\beta^2}{\sqrt{(1-\beta)^2 + (2\xi\beta)^2}} \tag{4-4}$$

where $\beta = \omega / \omega_n$. Figure 3-6(b) plot out the transfer function at different damping ratio. As can be seen from this figure, the system is a "low filter" system where the vibration frequency higher than the natural frequency will remain and lower frequency will be filtered. As a result, we prefer to increase the resonant frequency of the system to suppress vibration. To do that, we need to either increase the spring constant and/or reduce the mass of the floating element (floating plate and the sample). However, increasing the spring constant will decrease the displacement, which requires high sensor resolution. A tradeoff in displacement and vibration design is usually needed to ensure optimal performance.

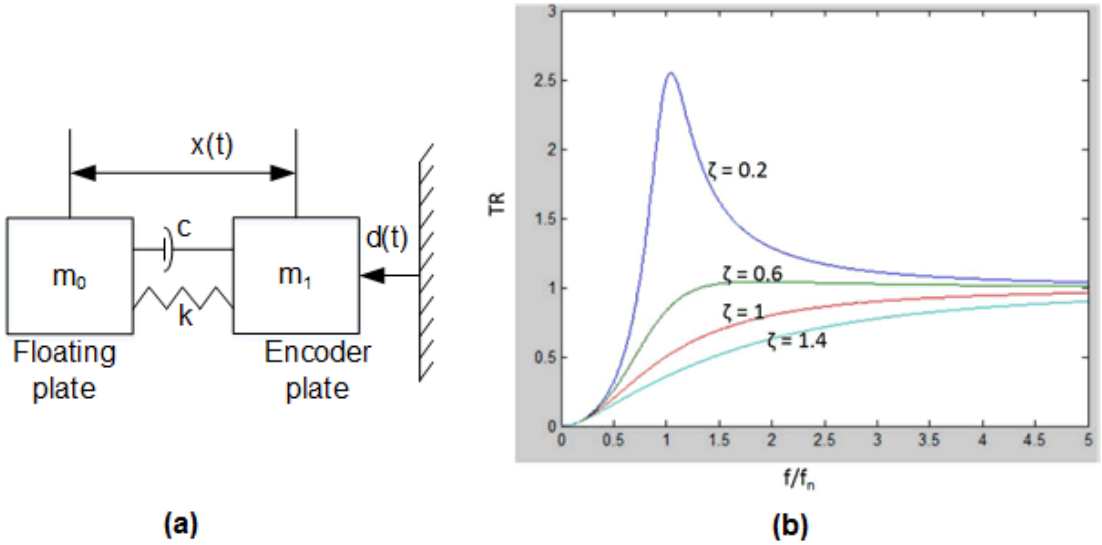

Figure 3-6 Frequency response of the shear sensor. (a) Schematic drawing of the vibration system. (b) Transfer function of the shear sensor system.

Once the spring constant is decided, the detailed beam dimensions need to be designed. For folded beams shown in Figure 3-5, the spring constant is:

$$k = \frac{l^3}{12EI} \tag{4-5}$$

l is the beam length, E is the Young`s modulus, I is the second moment of area. In designing the beam dimensions, sensor size, plate thickness and manufacturing limitations should be considered. High thickness-to-width ratio is preferred to make the sensor only sensitive to streamwise shear force. The metal beams were fabricated using wire EDM. Considering the processing limitation of the wire EDM vendor (Wire Cut Company, Buena Park, California), we set the beam to be 0.5 mm wide, 6.5 mm thick, and 50 mm long (but folded into two 25 mm long sections. With the above design, the resonant frequency is ~100 Hz, which is above the usual environmental vibration frequency (~30-60 Hz).

3.3.3 Finite Element Analysis

To predict the mechanical performance of the sensor, including spring constant, sensitivity and resonant frequency and associated mode shapes, finite element analysis (FEA) was performed (Comsol Multiphysics). We want to assure that the floating plate will displace a reasonable distance close to the theoretical estimation by the target flows and has minimal displacements in any other direction. To simplify the model, we didn`t include the smooth or SHPo surface sample in the model but replace them by an added mass onto the floating plate, as shown in Figure 3-7. First, to study the floating plate sensitivity in all directions, loads in all three directions are applied to the floating plate, which are F_x (spanwise direction), F_y (streamwise direction) and F_z (vertial-to-shear-plane direction). In actual flow condition, the streamwise direction load is much

larger than loads in other diirections. We set both to be the same here to purely compare the sensitivity of the flexural beams in these two directions.

Figure 3-7(a)-(c) shows the FEA result for the floating plate with $F_x = 18.6\,\text{mN}$, $F_y = 18.6\,\text{mN}$, and $F_z = 18.6\,\text{mN}$. This is the approximated minimum shear force for towing tank test used in next the next chapter. The floating plate displace ~1.95 μm in the streamwise direction, while shifting ~0.05 μm in the spanwise direction and ~0.07 μm in vertical-to-shear-plane direction. This indicates that the folded beams are ~ 40 and ~30 times stiffer in the spanwise and vertical-to-shear-plane directioncompared with streamwise direction. For streamwise direction displacement, spring constant $k_x \sim 8000$ was derived. For the target flow condition $\text{Re}_x \sim 10^6 - 10^7$, the displacement of the floating plate is from ~2 μm to ~36 μm. For the smallest displacement, the sensor resolution (0.078 μm) is only ~ 4% of the measured value, ensuring measuring accuracy. For the largest displacement, the displacement is only twice the viscous sublayer thickness similar to single-pivot sensor used in previous study [14], and minimizing the disturbance to the flow [40]. Figure 3-7(d) shows the maximum stress inside the beams at the maximum displacement in flow. The value, 3.75 MPa, is still far less than the yield stress of aluminum 6061 (~250 MPa) which is the material used for the sensor. So the beam structures are considered safe under the flow.

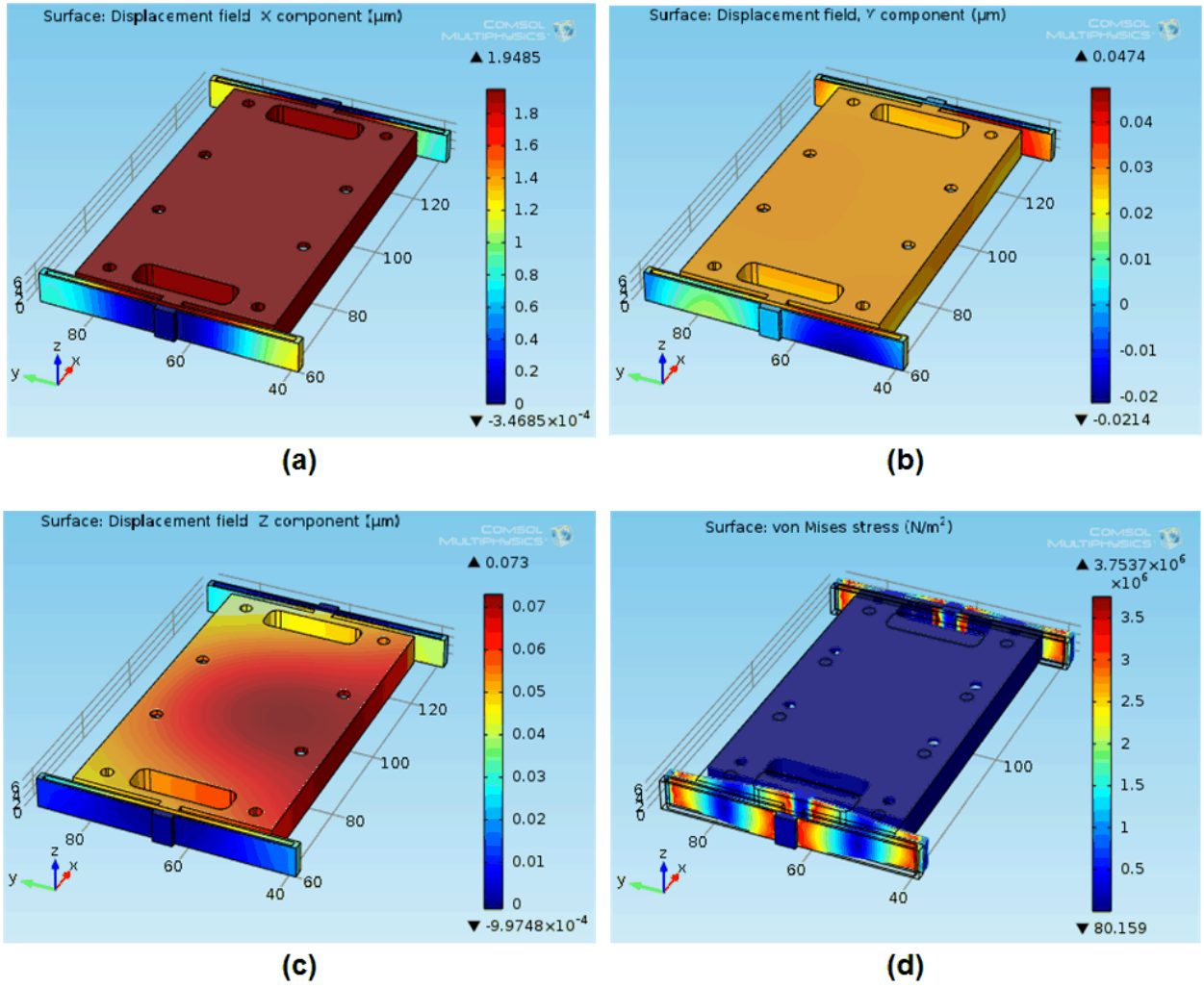

Figure 3-7 Displacement and stress analysis of metal shear sensor using FEA. (a) Floating plate displacement (~1.95 µm) with 18.6 mN in steamwise direction. (b) Floating plate displacement (~0.05 µm) with 18.6 mN in spanwise direction. (c) Floating plate displacement (~0.07 µm) with 18.6 mN in vertical direction. (d) Stress (max 3.75 MPa) inside the beam with maximum displacement (~ 36 µm) in flow.

Meanwhile, resonant frequencies and associated mode shapes for the floating plate were studied using FEA. Figure 3-8 shows the first four mode shapes of the sensor together with the resonant frequencies. As can be seen in the figures, the lowest resonant frequency for vibration along the

streamwise direction is ~120 Hz, which is much higher than regular environmental noise (~ 60 Hz) we encountered at different flow facilities. So the floating plate won`t encounter resonance during flow tests.

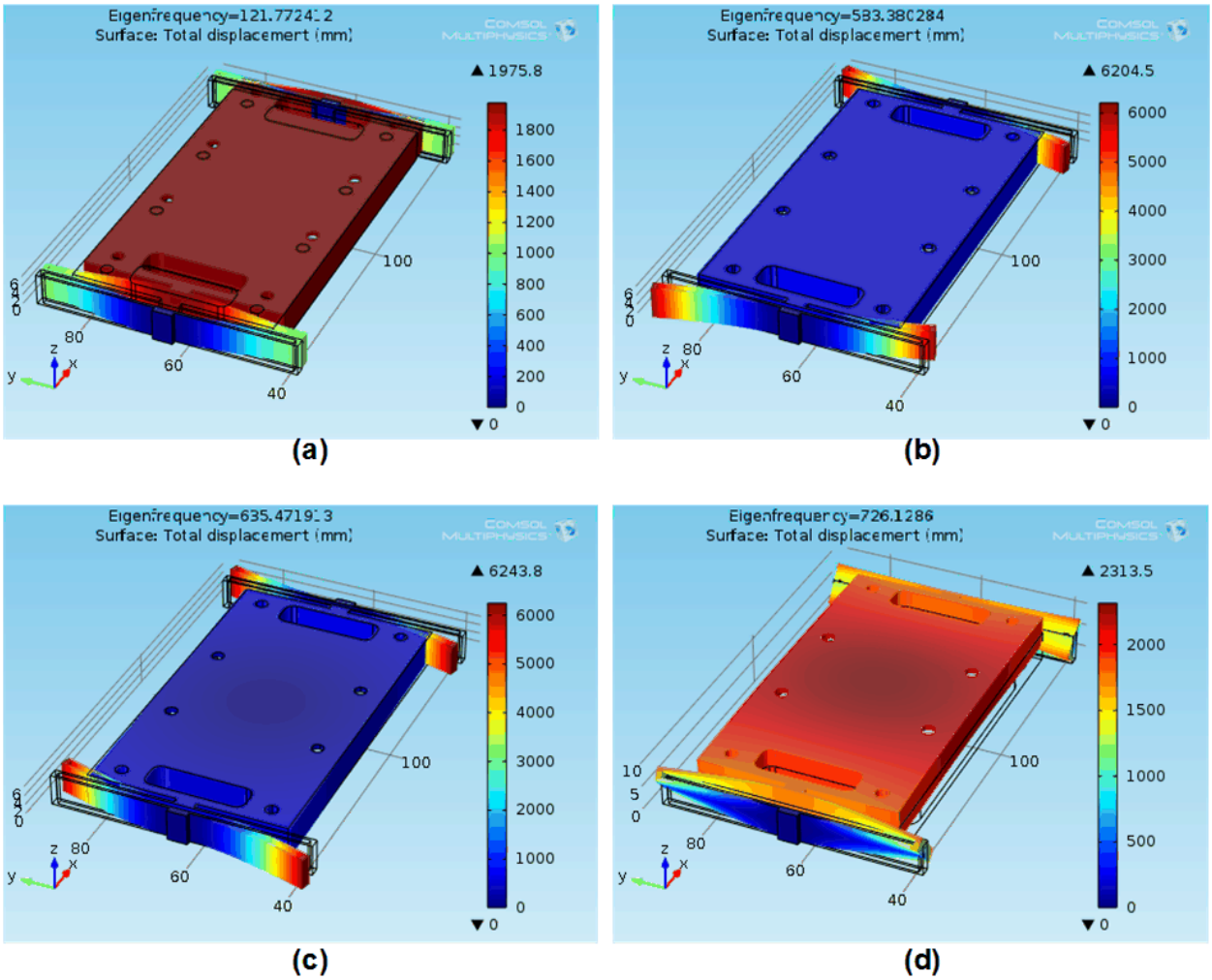

Figure 3-8 Resonant frequencies of the metal shear sensor.

3.3.4 Sensor Fabrication

The metal floating plate was monolithically manufactured from one metal plate using wire EDM after machining the pockets and holes using traditional milling and drilling. A cover plate, encoder holder and sample holder were also machined using milling and drilling and assembled to the

floating plate. The biggest challenge during the sensor fabrication was the wire EDM of extremely flexible beams and the floating plate. The most flexible folded beam machined was 50 mm long, 6 mm thick and 0.25 mm wide. Ideally, the beams and floating plate can be fabricated monolithic out of a metal plate using wire EDM using any path. However, using the current state of the art wire EDM techniques, such highly flexible beams would undergo non-negligible amounts of deflection during the wire EDM process due to thermal stress, dielectric liquid flushing, mechanical vibration, etc., causing non-uniform or broken beams. Similar challenges were expected for other slit-cutting methods, such as waterjet cutting and laser machining.

In order to solve this problem, we have designed special cutting path and sequence that employ temporary connections. This machining concept is composed of three steps: (1) while by making cuts to define the flexure beams and floating plate, leave temporary connections at certain strategic locations, (2) release the flexure beams by cutting some of the temporary connections, (3) release the floating plate by cutting the remaining temporary connections. Figure 3-9 illustrates one example of cutting paths and sequences with wire EDM that use temporary connections to obtain the floating plate. As seen in Figure 3-9(a) and Figure 3-9(b), individual cuts are sequentially made to define parts of the designed flexure beams and the floating plate. However, these cuts are isolated (not yet connected to each other) so all the flexure beams and the floating plate are still fixed to the frame plate by temporary connections. In Figure 3-9(c), some of the isolated cuts are connected to form the folded beams. These short cutting actions in the rigid directions (to connect neighboring isolated cuts) to remove the temporary connections do not deflect the beams and do not affect the integrity of the flexure beams, while releasing very flexible beams (e.g., single-folded beams shown). For the releasing steps, other types of temporary support (e.g., wax) could also be used. In Figure 3-9(d), the floating plate is released at the four corners, completing the

machining process of the plate. It is also possible to leave other locations for the temporary connections for the same design of flexure beams and floating plate. Different designs of floating plate and flexure beams would require different temporary connections, but following a similar process of leaving temporary connections that are later removed.

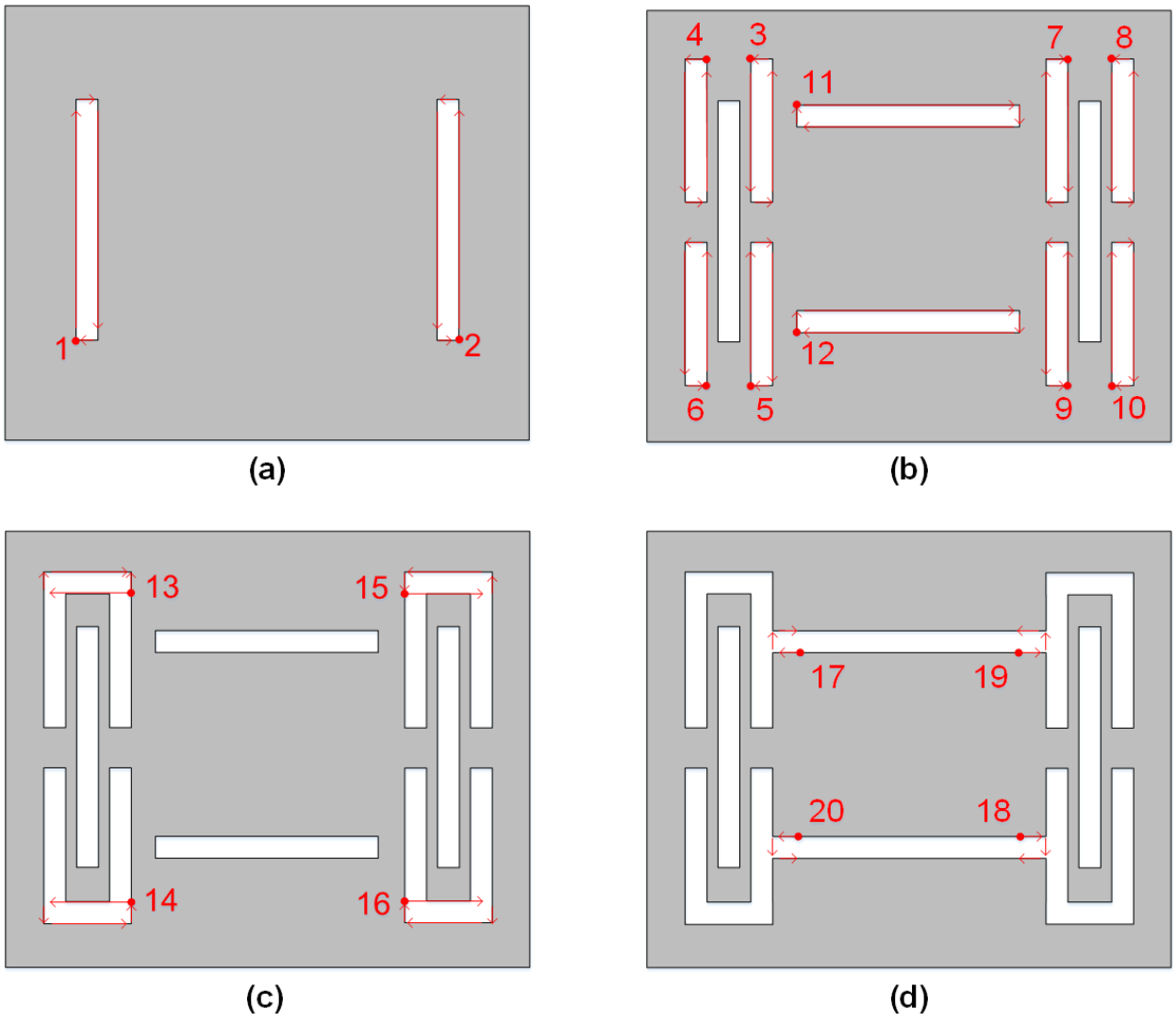

Figure 3-9 One example of cutting paths and sequences with wire EDM in fabricating the metal shear sensor.

Another problem found in the wire EDM process is the residual stress built during the process causing the beams to bend after releasing. The bent beam might even touch the sensor frame, causing measurement error. The key to solve this problem is to avoid any machining onto the beam area during milling or do a stress-releasing heat treatment right before the EDM process.

3.3.5 Sensor Characterization and Verification

3.3.5.1 Resonant Frequency Measurement

As mentioned before, the resonant frequency characterization is important for this shear sensor since it is designed for a wide range of flow facilities with potential large vibration and more violent turbulent flow. The resonant frequency was measured through a step-load method. The floating plate was pulled along the streamwise direction and released, as shown in Figure 3-10(a). The resonant frequency could be obtained by extracting the resonant frequency out of the damping curve using FFT. Figure 3-10(a) shows an example of the damping curve, with resonant frequency of 115 Hz extracted using Fast Fourier Transform (FFT).

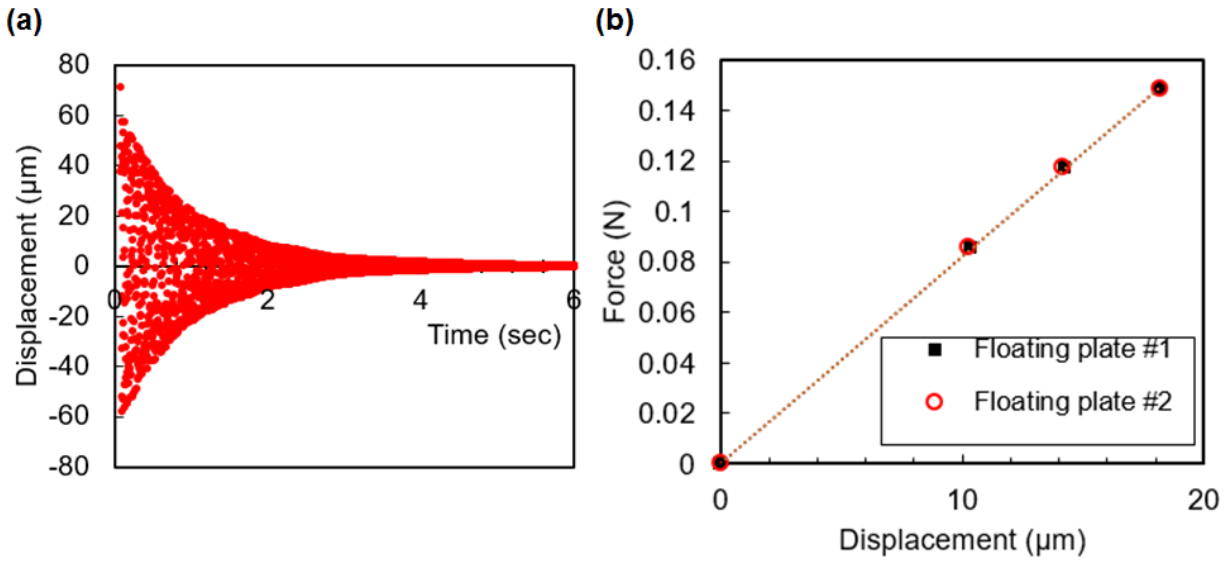

Figure 3-10 Natural frequency and spring constant measurement of shear sensor

3.3.5.2 Spring Constant Calibration

Spring constant if the beams needs to be calibrated for precise shear stress measurement. Two methods have been applied to measure the spring constant of different flexural beams depending on their spring constants. The first method applies when the beams have relatively large spring constant. The sensor was secured perpendicularly so the floating plate could displace along streamwise direction. Since the spring constant is large so the floating plate won`t touch the sensor frame. Different weights were hung onto the floating plate while the output is recorded. During the measuring process, the hung weight is kept still to prevent any forms of pendulum action that introduces measurement error. An exemplary measurement curve is shown in Figure 3-10(b) for two floating plates sensor (Figure 3-5(c)). As can be seen from the figure, both of the floating plates showed good linearity and very close spring constant.

However, if the spring constant is very small, the above method might not work since the floating plate might displace too much and hit the sensor frame when placed vertically. For extremely flexible beams, resonant frequencies are used to calibrate the spring constant. The resonant frequency was first measured without any extra mass on the floating plate. Then an extra known mass was attached onto the floating plate using double-sided tape and the resonant frequency was measured again. The spring constant and floating plate mass can be obtained by solving the following equations:

$$f_1 = \frac{1}{2\pi}\sqrt{\frac{k}{m}} \tag{4-6}$$

$$f_2 = \frac{1}{2\pi}\sqrt{\frac{k}{m+\Delta m}} \tag{4-7}$$

where f_1 and f_2 are the natural frequencies measured using FFT and Δm is the extra known mass added to the floating plate.

3.4 Summary

Two types shear stress sensor were developed in this chapter. The MEMS shear stress sensor was developed by improving the existing sensor [13] designed specifically for measuring SHPo surface drag reduction at in-house water tunnel. Compared with the existing sensor, the updated design and fabrication process greatly simplified the fabrication and increased the sensor robustness. However, due to the inherent drawbacks of silicon-based MEMS sensor, a novel metal shear stress sensor was developed to measure drag reduction of SHPo surfaces with larger area under different flow conditions. Not limited to water flows, the metal shear sensor developed is useful to measure friction drag of different surfaces for not only hydrodynamic applications but also aerospace applications. The following table compared this novel shear sensor with other two categories of commercial shear sensors and showed its advantages:

Table 3-2 Shear stress sensor comparison between MEMS sensor, single-pivot sensor and monolithic metal sensor

Sensor	Advantages	Disadvantages
MEMS sensor	**Slender beam:** -High sensitivity (e.g., 0.1 nN) **Monolithically made:** -Negligible misalignment -Immune to thermal expansion **Small gap O(1um):**	**Difficult packaging:** -Often not robust to water/particle impingement **Size limitation:** -Hard to measure mean shear stress over large area **DRIE etching:**

	-Hydraulically smooth -Less pressure-gradient error **Small mass:** -Insensitive to vibration/acceleration	-Beam thinning down
Single-pivot sensor	**Mature technology** **Harsh Environment:** -Applied at elevated temperature/pressure[9] **Single pivot support** -Stiff along the pivot direction -Insensitive to vibration/acceleration **No size limitation**	**Non-monolithic:** -Sensor misalignment -Thermal expansion -Assembly difficulty **Sensitive to temperature/pressure change**
Monolithic metal sensor	**Monolithically made:** -Negligible misalignment -Immune to thermal expansion **Robustness**: -Could be applied at elevated temperature/pressure -Insensitive to temperature/pressure change **No Size limitation** **Wire EDM:** -Uniform beam with high aspect ratio -Insensitive to vibration/acceleration	**Bubbles/particles in water may block the optical path**

3.5 References

[1] M. Sheplak, L. Cattafesta, and Y. Tian, "Micromachined shear stress sensors for flow control applications," in *IUTAM Symposium on Flow Control and MEMS*, 2008, pp. 67-73.

[2] R. J. Daniello, N. E. Waterhouse, and J. P. Rothstein, "Drag reduction in turbulent flows over superhydrophobic surfaces," *Physics of Fluids*, vol. 21, 085103, 2009.

[3] B. W. Vanoudheusden and J. H. Huijsing, "Integrated Flow Friction Sensor," *Sensors and Actuators*, vol. 15, pp. 135-144, 1988.

[4] C. Brücker, D. Bauer, and H. Chaves, "Dynamic response of micro-pillar sensors measuring fluctuating wall-shear-stress," *Experiments in fluids*, vol. 42, pp. 737-749, 2007.

[5] J. Zhang, H. Tian, Z. Yao, P. Hao, and N. Jiang, "Mechanisms of drag reduction of superhydrophobic surfaces in a turbulent boundary layer flow," *Experiments in Fluids*, vol. 56, pp. 1-13, 2015.

[6] V. Chandrasekharan, J. Sells, J. Meloy, D. P. Arnold, and M. Sheplak, "A Microscale Differential Capacitive Direct Wall-Shear-Stress Sensor," *Journal of Microelectromechanical Systems*, vol. 20, pp. 622-635, 2011.

[7] A. V. Desai and M. A. Haque, "Design and fabrication of a direction sensitive MEMS shear stress sensor with high spatial and temporal resolution," *Journal of Micromechanics and Microengineering*, vol. 14, pp. 1718-1725, 2004.

[8] J. Shajii, K.-Y. Ng, and M. A. Schmidt, "A microfabricated floating-element shear stress sensor using wafer-bonding technology," *Journal of Microelectromechanical Systems*, vol. 1, pp. 89-94, 1992.

[9] R. J. Meritt and J. A. Schetz, "Skin Friction Sensor Validation for High-Speed, High-Enthalpy Flow Applications," *AIAA 2014*, vol. 2800, 2014.

[10] A. Padmanabhan, H. Goldberg, K. D. Breuer, and M. A. Schmidt, "A wafer-bonded floating-element shear stress microsensor with optical position sensing by photodiodes," *Journal of microelectromechanical systems*, vol. 5, pp. 307-315, 1996.

[11] F.-G. Tseng and C.-J. Lin, "Polymer mems-based fabry-perot shear stress sensor," *IEEE Sensors Journal*, vol. 3, pp. 812-817, 2003.

[12] V. Natarajan, M. Kathiresan, K. Thomas, R. R. Ashokan, G. Suresh, E. Varadarajan, *et al.*, "MEMS Sensors for Underwater Applications," in *Micro and Smart Devices and Systems*, ed: Springer, 2014, pp. 487-502.

[13] G. Y. Sun, H. Park, and C. J. Kim, "Development of a Miniature Shear Sensor for Direct Comparison of Skin-Friction Drags," *Journal of Microelectromechanical Systems*, vol. 24, pp. 1426-1435, 2015.

[14] R. A. Bidkar, L. Leblanc, A. J. Kulkarni, V. Bahadur, S. L. Ceccio, and M. Perlin, "Skin-friction drag reduction in the turbulent regime using random-textured hydrophobic surfaces," *Physics of Fluids,* vol. 26, pp. -, 2014.

[15] J. A. Schetz, "Direct measurement of skin friction in complex flows," *Paper No. AIAA,* vol. 44, 2010.

[16] C. Lee, C.-H. Choi, and C.-J. Kim, "Superhydrophobic drag reduction in laminar flows: a critical review," *Experiments in Fluids,* vol. 57, 176, 2016.

[17] P. K. Kundu, I. M. Cohen, and D. R. dowling, "Chapter 12- Turbulence," in *Fluid Mechanics (Fifth Edition)*, ed Boston: Academic Press, 2012, pp. 541-620.

[18] T. G. Min and J. Kim, "Effects of hydrophobic surface on skin-friction drag," *Physics of Fluids,* vol. 16, pp. L55-L58, 2004.

[19] H. Park, H. Park, and J. Kim, "A numerical study of the effects of superhydrophobic surface on skin-friction drag in turbulent channel flow," *Physics of Fluids,* vol. 25, 110815, 2013.

[20] H. Tian, J. Zhang, E. Wang, Z. Yao, and N. Jiang, "Experimental investigation on drag reduction in turbulent boundary layer over superhydrophobic surface by TRPIV," *Theoretical and Applied Mechanics Letters,* vol. 5, pp. 45-49, 2015.

[21] H. Haibao, D. Peng, Z. Feng, S. Dong, and W. Yang, "Effect of hydrophobicity on turbulent boundary layer under water," *Experimental Thermal and Fluid Science,* vol. 60, pp. 148-156, 2015.

[22] B. V. Hokmabad and S. Ghaemi, "Turbulent flow over wetted and non-wetted superhydrophobic counterparts with random structure," *Physics of Fluids,* vol. 28, 015112, 2016.

[23] C. Peguero and K. Breuer, "On drag reduction in turbulent channel flow over superhydrophobic surfaces," in *Advances in Turbulence XII*, ed: Springer, 2009, pp. 233-236.

[24] B. Woolford, J. Prince, D. Maynes, and B. W. Webb, "Particle image velocimetry characterization of turbulent channel flow with rib patterned superhydrophobic walls," *Physics of Fluids,* vol. 21, 085106, 2009.

[25] C.-H. Choi and C.-J. Kim, "Large slip of aqueous liquid flow over a nanoengineered superhydrophobic surface," *Physical Review Letters,* vol. 96, 066001, 2006.

[26] S. Srinivasan, J. A. Kleingartner, J. B. Gilbert, R. E. Cohen, A. J. Milne, and G. H. McKinley, "Sustainable Drag Reduction in Turbulent Taylor-Couette Flows by Depositing Sprayable Superhydrophobic Surfaces," *Physical Review Letters,* vol. 114, 014501, 2015.

[27] B. J. Rosenberg, T. Van Buren, M. K. Fu, and A. J. Smits, "Turbulent drag reduction over air-and liquid-impregnated surfaces," *Physics of Fluids,* vol. 28, 015103, 2016.

[28] D. Saranadhi, D. Chen, J. A. Kleingartner, S. Srinivasan, R. E. Cohen, and G. H. McKinley, "Sustained drag reduction in a turbulent flow using a low-temperature Leidenfrost surface," *Science Advances,* vol. 2, 2016.

[29] G. Sun, H. Park, and C.-J. Kim, "Development of a Miniature Shear Sensor for Direct Comparison of Skin-Friction Drags," *Journal of Microelectromechanical Systems,* vol. 24, pp. 1426-1435, 2015.

[30] H. Park, G. Sun, and C.-J. Kim, "Superhydrophobic turbulent drag reduction as a function of surface grating parameters," *Journal of Fluid Mechanics,* vol. 747, pp. 722-734, 2014.

[31] C. Henoch, T. Krupenkin, P. Kolodner, J. Taylor, M. Hodes, A. Lyons, *et al.*, "Turbulent drag reduction using superhydrophobic surfaces," in *3rd AIAA Flow Control Conference*, 2006, pp. 5-8.

[32] E. Aljallis, M. A. Sarshar, R. Datla, V. Sikka, A. Jones, and C. H. Choi, "Experimental study of skin friction drag reduction on superhydrophobic flat plates in high Reynolds number boundary layer flow," *Physics of Fluids,* vol. 25, 2013.

[33] J. Kim, P. Moin, and R. Moser, "Turbulence Statistics in Fully-Developed Channel Flow at Low Reynolds-Number," *Journal of Fluid Mechanics,* vol. 177, pp. 133-166, 1987.

[34] S. F. Hoerner, *Fluid-dynamic drag: practical information on aerodynamic drag and hydrodynamic resistance*: Hoerner Fluid Dynamics, 1965.

[35] H. Schlichting, K. Gersten, and K. Gersten, *Boundary-layer theory*: Springer Science & Business Media, 2000.

[36] H. Park, "A numerical study of the effects of superhydrophobic surfaces on skin-friction drag reduction in wall-bounded shear flows," Ph.D. dissertation, Mechanical Engineering, University of California, Los Angeles, 2015.

[37] S. H. Lee and H. J. Sung, "Direct numerical simulation of the turbulent boundary layer over a rod-roughened wall," *Journal of Fluid Mechanics,* vol. 584, pp. 125-146, 2007.

[38] K. B. Golovin, J. W. Gose, M. Perlin, S. L. Ceccio, and A. Tuteja, "Bioinspired surfaces for turbulent drag reduction," *Phil. Trans. R. Soc. A*, vol. 374, 20160189, 2016.

[39] M. MacLean and J. A. Schetz, "Numerical study of detailed flow affecting a direct measuring skin-friction gauge," *AIAA journal,* vol. 41, pp. 1271-1281, 2003.

[40] J. W. Naughton and M. Sheplak, "Modern developments in shear-stress measurement," *Progress in Aerospace Sciences,* vol. 38, pp. 515-570, 2002.

Chapter 4 Drag Reduction of Superhydrophobic Surfaces in Turbulent Boundary Layer Flows

4.1 Introduction

Reducing the skin friction drag using superhydrophobic (SHPo) surfaces has attracted strong interest since early 2000s. In laminar flow, SHPo drag reduction has been reasonably well understood, and slips large enough to affect regular-scale flows have been obtained [1-5]. The amount of slip, generally quantified with a slip length, is mainly determined by the structural features of SHPo surfaces, such as the pitch, solid fraction, and pattern type, and further affected by secondary factors, such as the state of the liquid-gas interface [1]. Compared with laminar flow, turbulent flow covers a wider range of potential drag reduction applications including most marine vessels. However, research on turbulent drag reduction using SHPo surfaces is still an open topic with discrepancies reported among different experimental and numerical studies [6, 7]. While most numerical studies have shown definite drag reduction and suggested valuable insights into the drag-reducing mechanism, experimental studies showed either substantial or negligible drag reducing effect of SHPo surface in turbulent flow. Important trend unveiled in numerical studies, such as the effect of Reynolds number [8, 9], has not been verified in experiments or has even been contradicted [7]. Moreover, most experimental studies were limited to channel flows. The few experiments performed in open water were with a small model boat at relatively small Reynolds numbers [10-12]. Solely missing is zero-pressure-gradient (i.e., open water) turbulent boundary layer (TBL) flows at a high Reynolds number, which represent the main applications such as marine vessels. As far as we know, the only SHPo test performed at such realistic flow conditions found drag reduction at low Reynolds numbers but drag increase at high Reynolds numbers [13].

4.1.1 Turbulent Boundary Layer Flow

Zero-pressure-gradient TBL flow is the flow condition best describing the friction drag on the hull of marine vessels, which represent the most prominent application of drag reduction. Different from turbulent pipe or channel flows, TBL flow is bounded by only one wall with TBL growing downstream. Even though it is traditionally accepted that, upon appropriate normalization, turbulent pipe, channel and boundary layer flow can be regarded the same in the near wall region, these three flows are actually different in both near-wall and off-wall region [14] . This indicates that the SHPo drag reduction obtained for channel flow may not represent the scenario for TBL flow well. Moreover, a flow in channel or pipe tends to have pressure gradient in streamwise direction. Since most channels are a closed system in a loop, at high speed the water pressure may be lower than the atmospheric pressure in the test section, presenting an environment fundamentally different from those encountered by watercraft. Considering traveling water vessels, we are interested in zero pressure gradient TBL flows at hydrostatic pressure above the atmosphere. The water pressure has a major impact on the plastron shape, position and stability on SHPo surface [15, 16], which affect the drag reduction capability of SHPo surfaces greatly [6]. To confirm the performance of SHPo surface for applications on marine vessels, preferred is (1) direct measurement of friction drag (2) in open-water TBL flows, (3) especially at high speed.

The skin friction coefficient (C_f) on different surfaces is the criteria to compare drags. The average skin friction coefficient on a surface can be calculated with experimental data:

$$C_{f,avg} = \frac{Drag}{0.5\rho U^2 S} \tag{5-1}$$

where ρ is the density of the water, U is the free stream speed and S is the area of the sample. There has also been a widely-accepted empirical equation for skin friction coefficient on smooth surface [17] in TBL flow:

$$C_f(x) = (2\lg(\mathrm{Re}_x) - 0.65)^{-2.3} \tag{5-2}$$

where $\mathrm{Re}_x = Ux/\nu$ is the Reynolds number based on the distance x measured from the beginning of the TBL and μ is the dynamic viscosity of the fluid. Equation (5-2) predicts the skin friction coefficient at a certain point x. To compare with the averaged skin friction coefficient obtained in experiments, the theoretical value should be calculated by integrating the $C_f(x)$ over the area of the sample and then divided by the area:

$$C_{f,avg} = \frac{1}{S}\iint C_f(x)dxdz \tag{5-3}$$

However, since the sample size is much smaller than the whole flow facility, the variation of $C_f(x)$ on the sample is small. The integration is simplified to approximate $C_{f,avg}$ using the theoretical skin friction coefficient at the center of the sample:

$$C_{f,avg} = (2\lg(\mathrm{Re}_L) - 0.65)^{-2.3} \tag{5-4}$$

where L is the distance from the beginning of the TBL to the center of the sample.

4.1.2 Motivation

With very few experimental studies in TBL flow [6, 10-13] and especially with the increasing drag at high Reynolds numbers [13], this study aims to address the doubts of SHPo drag reduction in TBL flows, with an ultimate goal of experimentally studying zero-pressure-gradient TBL flows at

high Reynolds numbers. In the course, we would also like to learn how Reynolds number and surface geometry affect the drag reduction. In this study, we conducted experiments using different SHPo surfaces, mostly silicon grating microstructures of 50 μm pitch and 90% gas fraction, at four different facilities: low speed channel, high-speed channel, high-speed towing tank and in marina. All four provided TBL flow condition with the latter three reaching high Reynolds numbers ($\mathrm{Re} \sim 10^6 - 10^7$) and the last with actual marine vessel. During all these experiments, our interests were the effect of wetting transition, structure type and surface geometry, and Reynolds number. One of the main discrepancies between experimental and numerical results was the Reynolds number effect, especially in large flow facilities [7].

4.2 Review of Recent Studies on SHPo Surface Turbulent Drag Reduction

4.2.1 Numerical Studies

So far, most of the studies on SHPo turbulent drag reduction have been numerical. Most numerical studies assumed surface structures that are truncated on top (i.e., of a uniform height) and air-water interfaces that are flat and flush with the structure top. The geometries studied were usually ordered structures like gratings and posts. Very recently, curved air-water meniscus [18] or meniscus fluctuation [19] began to be incorporated into numerical studies. Despite the assumptions, advances in numerical simulations have provided valuable physical insights on the mechanisms of turbulent drag reduction. A given SHPo surface has been found to reduce drag more in turbulent flow than in laminar flow [20], indicating additional drag reducing mechanisms in turbulent flow [21]. It was also found that the effective slip length should be on the order of the viscous sublayer thickness, which is about five in viscous wall units (i.e., $y^+ \sim 5$), in order to have an impact on skin-friction drag in turbulent flows [8]. Regarding the drag reduction mechanisms of SHPo

surfaces, some works [8, 22] indicated the drag reduction is an indirect effect through a modification of near-wall turbulence structures, while other works saw it as a direct effect of the slip or shear-free regions [23, 24], similar to the drag reduction in laminar flow. However, despite the discrepancies on drag reducing mechanisms, SHPo drag reduction in fully developed turbulent flow has been confirmed in almost all numerical studies and further shown to increase with Reynolds number [8, 9, 22].

4.2.2 Experimental Studies

Experimental studies on SHPo drag reduction in turbulent flow have been elusive with significant inconsistency compared with numerical studies. Table 4-1 and Figure 4-1 summarized recent experimental studies of SHPo drag reduction in turbulent flows. Since many different flow facilities were used, we compared the results based on frictional Reynolds numbers Re_τ estimated from each report [7]. As seen from the table and graph, results are widely inconsistent between different experiments, even for tests with similar SHPo surface structure and flow conditions. While some studies reported substantial drag reduction (up to ~75% [6]), others showed negligible drag reduction or even drag increase. In reviewing all these results, we are trying to develop some insights into the factors affecting SHPo drag reduction in turbulent flow as well as the reasons for discrepancies between experimental and numerical results.

Table 4-1 Surface parameters and flow conditions of the SHPo turbulent drag reduction studies in the literature

Reference	Microstructure	Flow type	Re_τ	Sample length (cm)
Henoch et al. [25]	Posts	Water tunnel: TBL flow	500-600	20

Daniello et al. [26]	Gratings	Water tunnel: Channel flow	100-300	100
Peguero & Breuer [27]	Gratings, posts, random	Water tunnel: Channel flow	200	43
Woolford et al.[28]	Gratings	Water tunnel: Channel flow	3-100	8
Park et al. [6]	Gratings	Water tunnel: TBL flow	250	2
Zhao et al. [29]	Random	Water tunnel: TBL flow	1700-3000	80
Aljallis et al. [13]	Random	Water tunnel: TBL flow	520-5170	122
Bidkar et al. [30]	Random	Water tunnel: TBL flow	1000-5000	15
Hu et al. [31]	Random	Water tunnel: TBL flow	320	40
Srinivasan et al. [32]	Random	Rheometer: Taylor-Couette flow	480-3810	60
Tian et al. [33]	Random	Water tunnel: TBL flow	480	20
Zhang et al. [34]	Random	Water tunnel: Channel flow	329-467	68
Hokmabad & Ghaemi [35]	Random	Water tunnel: Channel flow	246	50

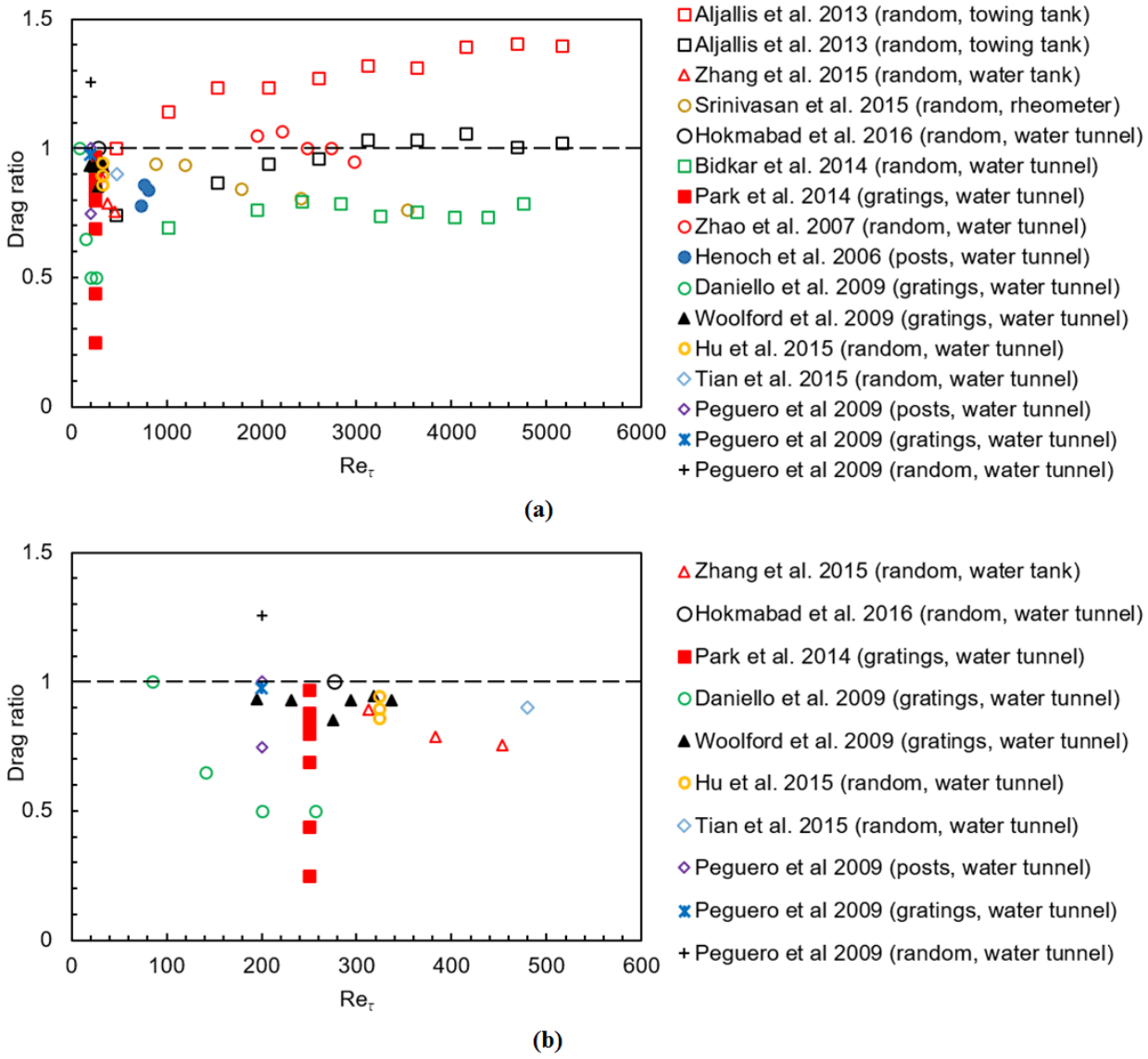

Figure 4-1 Drag ratio (i.e., drag on sample surface / drag on smooth surface) of SHPo drag reduction in turbulent flow experiments. (a) full Reynolds number range ($\mathrm{Re}_\tau = 0-6000$). (b) Magnified for low Reynolds number range ($\mathrm{Re}_\tau = 0-600$).

4.2.2.1 Ordered Structures: Gratings and Posts

The microstructures on SHPo surfaces can be categorized as two types: random structure and ordered structure. As can be seen from Figure 4-1, flow experiments for ordered structure (e.g.,

gratings, posts) were conducted at relatively low Reynolds numbers while flow experiments with random surfaces were conducted over a full range of Reynolds numbers. This is probably because SHPo surface with ordered structures, typically involving photolithography in cleanroom, are made in a relatively small size (e.g., < 2 cm). As high accuracy drag sensors compatible with both such small samples and large flow facilities (e.g., towing tank, large water tunnel) are not available, the SHPo surfaces with ordered structures could not be tested at high Reynolds numbers. In comparison, SHPo surfaces with random structures can be made in large size, allowing for high Reynolds number experiments in large flow facilities. Based on the results in Figure 4-1 [6, 26-28], SHPo surfaces with micro gratings aligned in the streamwise direction appear to reduce drag unambiguously [7]. However, gratings transverse to the flow direction were reported to increase the drag [28]. The effect of grating orientation in experiments matches the predictions in many numerical studies [8, 22, 36, 37], which suggested that streamwise slip would reduce drag while spanwise slip would increase drag. Grating structures aligned with flow will facilitate streamwise slip and suppress spanwise slip, reducing drag, while grating structures transverse to the flow will increase spanwise slip and suppress streamwise slip, increasing drag.

Using grating-structured SHPo surface, Daniello *et al.* [26] studied the drag reduction in turbulent channel flow. They found no observable drag reduction of SHPo surface in laminar regime, as expected from their relatively large channel geometry. Note the drag reducing effect of SHPo wall diminishes as the hydraulic diameter of the channel increases with respect to the slip length of the SHPo wall. However, as the Reynolds number increased to turbulent regime, the drag was reduced by up to 50%. Both of the upper and lower walls of the channel were covered with the SHPo surface. They also found the onset of drag reduction is when the viscous sublayer approaches the

scale of the SHPo feature size, which roughly represents the slip length [1,2]. In their tests, the SHPo drag reduction increased as Reynolds number increased.

Woolford *et al.* [28] tested grating SHPo surface with both streamwise and spanwise alignment. With smaller pitch but higher gas fraction than Daniello et al. [26], they observed the drag reducing by ~11% for streamwise-aligned SHPo surface in a similar Reynolds number range. Note only one wall of the channel was covered with the SHPo surface. They also found the relative drag would increase when the SHPo surface gratings were aligned spanwise to the flow. The water pressure in their experiments was well controlled to prevent Cassie-to-Wenzel wetting transition on SHPo surface. Unlike Daniello et al. [26] and numerical studies [8, 9, 22], the drag reduction (~11%) seemed to be uniform across the entire Reynolds number range.

More recently, drag reduction as high as 75% was obtained by Park et al. [6] using grating SHPo surfaces in TBL flow in a water channel. They studied the influence of the grating geometries on SHPo drag and found the drag ratio reduced more with increasing gas fraction and pitch of the gratings. This is the largest turbulent drag reduction of SHPo surface obtained in experiments. The relationship between drag reduction and surface geometry unveiled in this study is crucial for future design of SHPo surface for real-world application.

There are less experimental studies using SHPo surface made of posts compared with gratings. Henoch et al. [25] studied the drag reduction of SHPo surface made of nanoscale posts (nanograss). Large drag reduction as high as 50% was observed in laminar regime. However, as the Reynolds number increased to turbulent regime, the drag reduction decreased to ~15%. Peguero & Breuer [27] used similar nanograss SHPo surfaces and found no definitive evidence of drag reduction. Based on the numerical studies [8, 22, 36, 37] and the experimental studies of Woolford *et al.* [28],

spanwise slip will increase the drag. Compared with grating structures aligned to the stream, post structures are expected to have more spanwise slip and thus less drag reduction.

4.2.2.2 Random Structures

There have been many experimental studies on SHPo drag reduction using different random structures in a wide range of Reynolds numbers. As can be seen from Figure 4-1, both drag reduction and drag increase have been observed in different tests at different testing facilities. Also, the detailed geometry and morphology of random structures used in these tests are quite different. Several studies [7, 13, 34, 35] used the same spraying product (i.e., NeverWet®, Rust-Oleum) to make SHPo surfaces, but note the resulting surface structures still vary vastly by the coating process. Alijallis *et al.* [13] tested two different random SHPo surface for a wide range of Reynolds number in TBL flows using a high-speed tow tank. The surface with smaller surface roughness increased the drag compared with smooth surface. The surface with higher roughness decreased the drag compared with smooth surface at low Reynolds numbers in transitional regime but maintained or even increased the drag compared with smooth surface at high Reynolds numbers in fully developed regime. Zhang *et al.* [34] tested similar surfaces in channel flow and obtained 10% to 24% drag reduction at relatively low Reynolds number. They also observed the drag ratio decreasing more with the Reynolds number as well as turbulent structures reducing, as predicted in numerical studies. However, no evident of drag reduction was found in the experiments of Hokmabad et al. [35] at similar Reynolds number as Zhang *et al.* [34]. Golovin et al. [7] evaluated same product in channel flow and found no noticeable drag reduction and instead found even drag increase compared with smooth surface at high Reynolds numbers. From the above independent studies, it is suggested that the drag reduction for these types of random SHPo surface is negligible or even negative at high Reynolds numbers. At low Reynolds numbers, there seem to be some

drag reduction compared with smooth surfaces depending on the flow facilities. Alijallis *et al.* [13] observed depletion of plastron along with drag increase compared with smooth surfaces at high Reynolds number. However, with submicron scale roughness on the tested SHPo surface and relatively shallow immersion depth, pure gas diffusion is not expected to deplete all trapped gases [16, 32]. This consideration suggests more violent depletion factors, possibly highly fluctuating pressure, caused gas depletion at high Reynolds numbers. Besides the different surface structure morphology and geometry due to different spraying methods, the discrepancy of the data using the same spray product may have also come from different flow conditions. For example, supersaturated water or microbubbles often existing in water tunnel can sustain large (thick) gas plastron on a random roughness, which would lead to an impractically large drag reduction.

Other customized SHPo surface with random roughness have also been tested. Bidkar et al. [30] studied 12 types of random-structured SHPo surfaces with different roughness and chemical composition. Some types increased the drag ratio while others decreased the drag ratio compared with smooth surface. They have concluded the effect is caused by different surface roughness and found a critical surface roughness that is $1/10^{th}$ of the viscous sublayer thickness. Only when surface roughness was below the critical value the drag ratio was found decreasing. The roughness effect is explained as the form drag caused by wetted protrusions into the water. With the smallest roughness SHPo surfaces tested, they obtained drag reduction of 20% to 30 % even at very high Reynolds number. Other higher roughness SHPo surface samples caused drag increasing compared with smooth surfaces. However, in Alijallis *et al.* [13], the SHPo surface with lower surface roughness (SH-1) generated more drag than both the high-roughness SHPo surface (SH-2) and smooth surface, which cannot be explained solely by the discussion of roughness vs. viscous sublayer. While higher roughness surface might introduce more form drag by wetting protrusions,

it can also capture a thicker plastron for drag reduction. Even if the random surface has small roughness than the threshold, it does not have the gas plastron that provides enough streamwise slip. So the drag of random SHPo surface should be a combination of surface roughness and other factors (e.g., morphology, structure geometry, surface chemistry), which require further studies.

It is also worth noting that no significant wetting was observed for all surfaces tested by Bidkar et al. [30], while Alijallis et al. [13] observed gas depletion at similar Reynolds number range. From the SEM pictures, the surfaces by Alijallis *et al.* [13] seems to have even smaller feature size and pitch than those by Bidkar *et al.* [30], meaning those by Alijallis *et al.* [13] should have more robust meniscus and less gas depletion. Instead of the roughness, we suspect the difference in the result was caused by the difference in the flow condition, e.g., water pressure and gas saturation level. Alijallis *et al.* [13] tested the SHPo surface in towing tank with zero pressure gradient and hydrostatic pressure above the atmospheric pressure. On the other hand, Bidkar et al. [30] conducted the test in water tunnel, where the water pressure could be below the atmospheric pressure at high flow speed in a closed system. The supersaturated water and gas bubbles in the water below the atmospheric pressure would help sustain the gas plastron and even grow it thicker than usual [15].

Srinivasan *et al.* [32] tested random-structured SHPo surface in Taylor-Couette flow using rheometer. They found little reduction of drag ratio at low Reynolds number but reductions as much as ~22% as Reynolds number increased, verifying the Reynolds number effect predicted by many numerical studies [8, 9, 22]. To better sustain the gas plastron on their SHPo surface, the SHPo surface was intentionally connected to outside atmosphere so the loss of air through diffusion could be replenished to maintain the gas plastron during the testing period. In contrast, they showed isolated plastron would have much less drag reduction, especially at high Reynolds

number. As shown in Figure 4-2(a), the plastron on their surface resides on the tall protrusions, forming a continuous gas plastron with high gas fraction. However, as verified previously [15, 16], such gas plastron is very fragile if isolated underwater even at low immersion depth, as shown in Figure 4-2(b). Most recently, the same group tested a very thick (~40 microns) plastron by heating the surface to above Leidenfrost point [38]. As predicted from the thick and continuous (i.e., gas fraction = 100%) gas layer and resulting very large slip length, drag reduction as much as 90% was obtained. However, the heating power needed to sustain the Leidenfrost state was more than 100 times the torque power saved by the reduced drag.

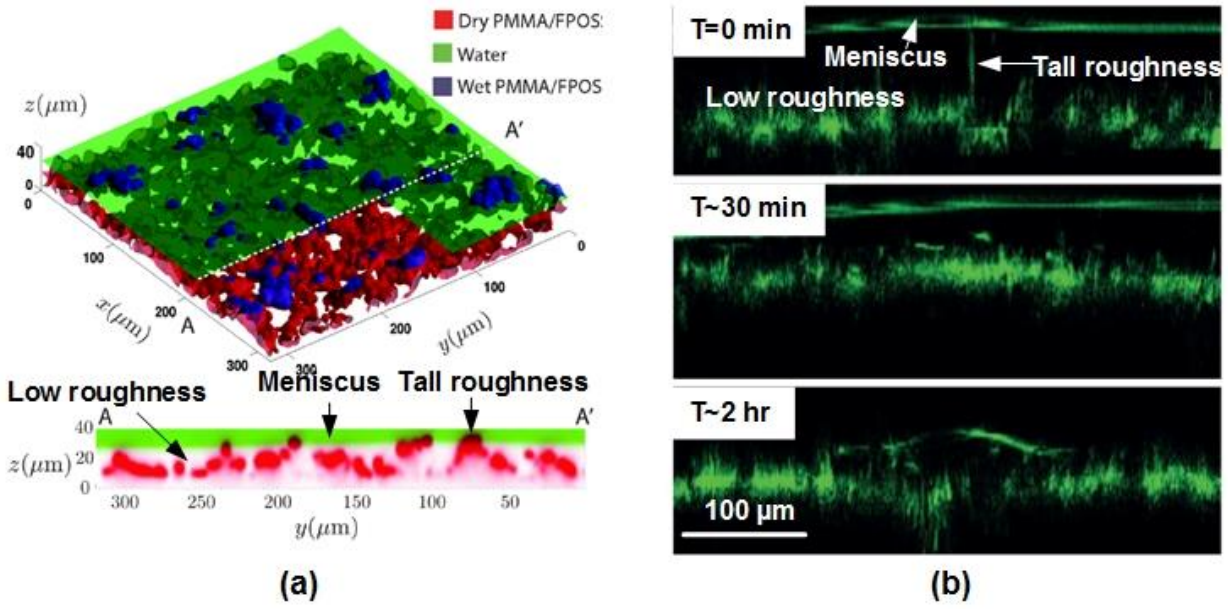

Figure 4-2 Confocal microscopic picture of air-water meniscus on SHPo surfaces with random roughness. (a) Confocal microscopic picture of the surface roughness and meniscus position on SHPo surface tested in [32]. (b) Confocal microscopic picture of the surface roughness and meniscus coming down in [16], immersed at 0.5 m.

Many other experiments have been conducted with random-structured SHPo surface, as shown in Figure 4-1. Random-structured surfaces generally could reduce drag ratio in low Reynolds number but maintains or even increases drag ratio at high Reynolds number, especially in large flow facility. Most random-structured SHPo surfaces have uneven structures composed of tall and short protrusions. As shown in Figure 3-2(a), the tall roughness initially supports thick and significantly continuous air plastron [16, 32] which could reduce drag. However, without additional gas stabilization mechanism like supersaturated water or connection to atmosphere, the large plastron will soon be lost even in static water [16]. It is less robust than the gas on ordered structures with similar scale, especially reentrant structures [15]. Once the air-water meniscus starts to move down into the structural voids, wetted protrusions sticking into water will increase the form drag. Moreover, random structured surface doesn`t have preferential streamwise or spanwise orientation in its structures, where increased spanwise slip will increase the drag [7].

Despite the popularity, we believe the random roughness is not the right approach for drag reduction in most flow applications of practical importance. Firstly, the homogenous nature of random SHPo surface does not provide the slips in preferential direction. Secondly, random structures are usually uneven in height, causing form drag once some protrusions impales and stick into water [7, 30]. Thirdly, the plastron that can induce drag reduction is less stable compared with grating structures [15]. The submicron scale air pockets on random surfaces are usually very robust [15, 16], but they cannot cause significant drag reduction. Note one needs a plastron continuous along flow direction [7, 8, 28]. While thick and large gas plastrons may form on random SHPo surface momentarily, such a plastron is more fragile in shear and pressure than that on ordered structures, encountering structures protrusions and eventual drag increase [15]. Overall, we do not

expect any significant drag reduction on SHPo surfaces made of random roughness in high-Reynolds number TBL flows in open water.

4.2.3 Discussion

4.2.3.1 Ideal Microstructure for Turbulent Drag Reduction

Based on the recent numerical and experimental studies, SHPo surface with textures aligned in the streamwise direction is preferred for turbulent drag reduction [7]. As predicted in many numerical studies [8, 22, 36], the streamwise slip would facilitate drag reduction while the spanwise slip should increase the drag. The ideal structure to maximize streamwise slip while suppress spanwise slip is grating structures. While the grating structure is ideal in terms of performance, its biggest drawback is the large-scale fabrication [7], which is difficult and expensive using current silicon processing technology in cleanroom. The mass manufacturing of grating-structured SHPo surface is crucial and will be another important topic in this dissertation.

4.2.3.2 Meniscus Stability and Reynolds Number Effect

As mentioned earlier, numerical studies [8, 9, 22] have almost unanimously shown the drag ratio decreasing more as Reynolds number increases. This is an exciting trend for practical applications, where high speed applications could enjoy enhanced drag reduction. However, the experiment results are quite inconsistent on this topic. Rheometer experiments [32] has shown a trend consistent with numerical studies that the drag ratio reduced more as Reynolds number increased. Srinivasan *et al.* [32] also derived a skin friction law that shows the dimensionless slip length b^+ scales with $\mathrm{Re}^{1/2}$, which was also supported by the experimental results. In small channel flows, Daniello *et al.* [26] also showed the drag ratio decreasing more with Reynolds number until

saturating. However, recent studies [7, 39] showed possible measurement problems in small channels, which could inaccurately portray the full effect of turbulence over SHPo surfaces.

However, in large-scale flow facilities with high Reynolds number, an opposite trend has been observed as shown Figure 4-1. Random-structured surfaces have shown drag reduction deteriorating [13, 35] or saturating [30] at high Reynolds number. Accordingly, there has not been any fully developed turbulent channel or TBL flow where the drag ratio decreasing more with increasing Reynolds number. Golovin *et al.* [7] concluded the discrepancy to several reasons. First, the increased Reynolds number may increase the spanwise slip without increasing the streamwise slip for random-structured SHPo surfaces, compromising the drag reduction. Second, the high fluctuation of pressure causes the air-water interface to slide down or bend into the structures. If the meniscus slides down into the structures and exposes the protrusion in water, the form drag will be added to the total drag known as roughness effect. Also, even if the meniscus only bends down towards the structure without the wetting protrusion, recent numerical study [18] showed the drag reduction will be deteriorated.

All in all, the unstable air-water interface and the wetting protrusions at high Reynolds number are the main reasons causing the discrepancy between numerical studies and experimental studies on Reynolds number effect. Random SHPo surface may sustain a thick and significantly continuous air plastron in small flow setup like rheometer. However, this delicate plastron is unlikely to sustain in large flow facilities with much significant pressure fluctuation at high Reynolds number.

4.3 SHPo Surface Fabrication

Three major types of SHPo samples were fabricated to test drag reduction in TBL flow: silicon based SHPo surface coated with hydrophobic Teflon AF 1600 coating, Teflon FEP based SHPo

surface, SHPo surface with random structures using NeverWet spray. For silicon based samples, different geometries of micro gratings were also fabricated.

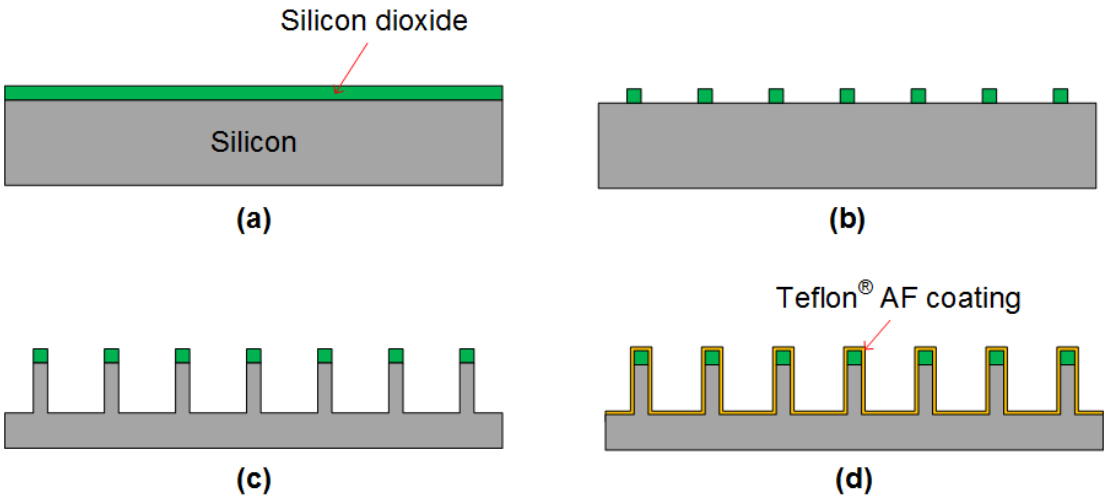

Figure 4-3 Fabrication process of silicon SHPo surface.

The fabrication process of silicon-based SHPo surface is shown in Figure 4-3. It starts with a 500 µm thick silicon wafer with 1 µm silicon dioxide layer on top. Then the silicon dioxide layer was patterned using photolithography and reactive ion etching (RIE). The oxide gratings served as a mask for the following deep-reactive-ion-etching (DRIE), which define the micro trenches on the silicon wafer with different depth. After the DRIE etching, the samples were cleaned using oxygen plasma to remove the polymer residuals left during plasma etching. Then the samples were coated with a thin layer of photoresist AZ 5214 and diced to rectangular shape. The photoresist, serves as a protection layer, is to protect the sample from getting dirty during the dicing. After dicing, a thorough cleaning using Piranha solution (98 wt.% sulfuric acid : 30 wt.% hydrogen peroxide = 4:1) and oxygen plasma was needed. After that, the Teflon AF 1600 were spin coated and baked in two stages: 165 ℃ for 15 minutes and 330 ℃ for 10 min following manufacturer`s specifications. Figure 4-4(a)(b) shows the silicon SHPo surface with zoomed-in views showing the structure of

the tip. As can be seen from Figure 4-4(a), the top of the grating has “reentrant structure” from undercut of silicon during etching. However, in Figure 4-4(b), the silicon grating with smaller dimension doesn`t have “reentrant” structure. This is probably caused by longer etching time when fabricating structures in Figure 4-4(a).

The Teflon FEP based SHPo surface was fabricated using hot embossing process. Silicon mold with the reverse feature of the SHPo surface was manufactured using DRIE and RIE etching. Then Teflon FEP film is pressed into the micro trenches on the mold at elevated temperature (~275 ℃). The mold was then cooled down and the SHPo surface was demolded from it. The detailed process parameters for mold fabrication and hot embossing will be discussed in Chapter 5. Figure 4-4(c) show the micro grating structures of the Teflon FEP SHPo surface with the end-view of the grating (Figure 4-4(c)). No reentrant structures exist on top of the micro-gratings, and the corners of grating top are even round as shown in Figure 4-4(c).

The SHPo surfaces with random structures were made using a two-step coating process using commercial SHPo spraying product (NeverWet, Rust-Oleum, LLC). In step one, an acrylic-based polymer solution was applied as a binder layer on silicon rectangular piece that is already diced to the right dimensions. In step two, hydrophobic nanoparticles dispersed in ethanol were sprayed as a topcoat on the binder layer, while the binder layer was flashed for a few minutes. The topcoat solutions contain 3%-4% of nanoparticles in dispersion. The topcoat attaches the hydrophobic nanoparticles to the base layer and leads to form nanoscale surface texture. 1%-2% of microparticles is also included in the solution. It enhanced the bonding sites between the binder and topcoat and resulted in higher roughness of the surface texture. Figure 4-4(d) shows the surface texture and morphology of the coatings at different magnifications. As can be seen from the figure, the surface has both micro-scale roughness and nano-scale roughness.

To simplify the notation for different SHPo surfaces used in flow test, we assigned numbers for each different type of SHPo surface, as shown in Table 4-2.

Table 4-2 Summary of all SHPo surfaces parameters used in flow test

Notation	Description
SHPo#1	Silicon SHPo surface with micro-gratings. The gratings have 50 μm pitch, 90% gas fraction and 60 μm height.
SHPo#2	Silicon SHPo surface with micro-gratings. The gratings have 25 μm pitch, 90% gas fraction and 25 μm height.
SHPo#3	Teflon FEP SHPo surface with micro-gratings. The gratings have 50 μm pitch, 85% gas fraction and 40 μm height.
SHPo#4	NeverWet SHPo surface with random roughness
SHPo#5	Silicon SHPo surface with micro-gratings. The gratings have 50 μm pitch, 90% gas fraction and 30 μm height.

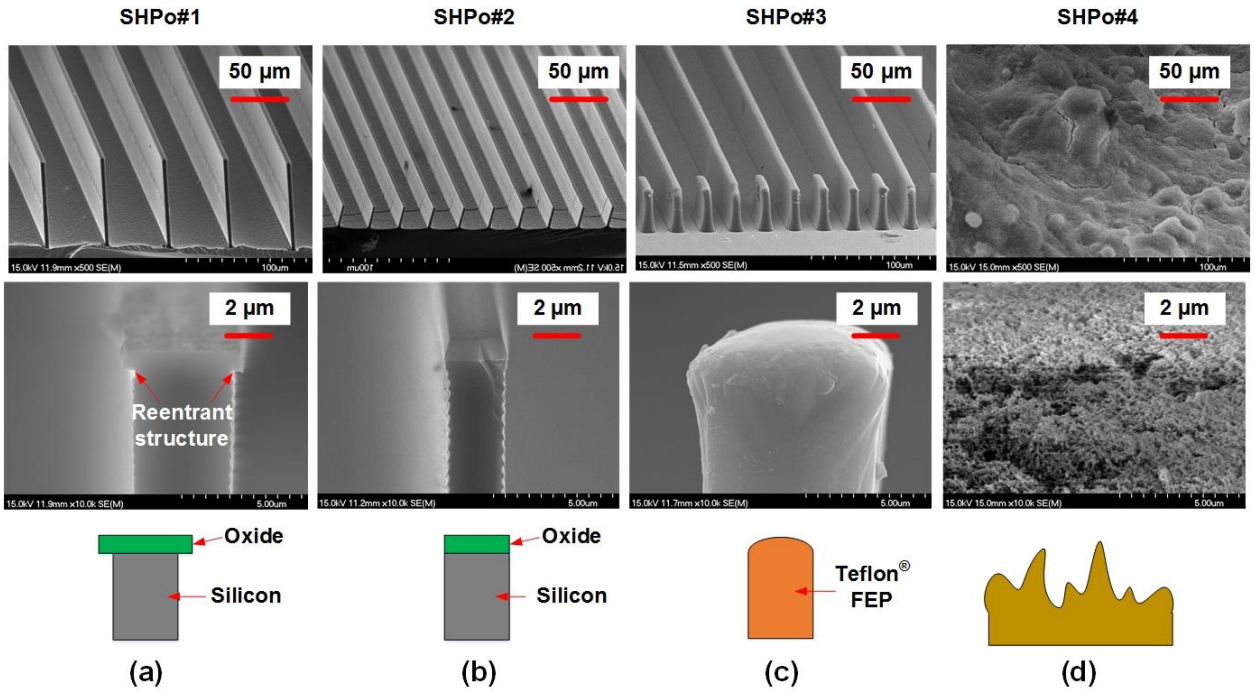

Figure 4-4 Structures of different SHPo surface used for drag reduction test. (a)(b) Silicon SHPo surface. (c) Teflon FEP SHPo surface (d) NeverWet random SHPo surface

For the examinations of the wetting properties of different SHPo surfaces, static contact angles were measured. As shown in Figure 4-5, the static contact angle was measured by placing a deionized water droplet (~ 7 μL in volume, ~2 mm in diameter) on the surface. For SHPo surface with ordered structures (Figure 4-5(a)(b)), the measured contact angles were consistent with theoretical contact angle calculated using Cassie state theory (~160^{o}), confirming the air-water meniscus is on top of the trenches. For random SHPo surface, the contact angle result was similar to the previous study [13], confirming the superhydrophobicity of the coating.

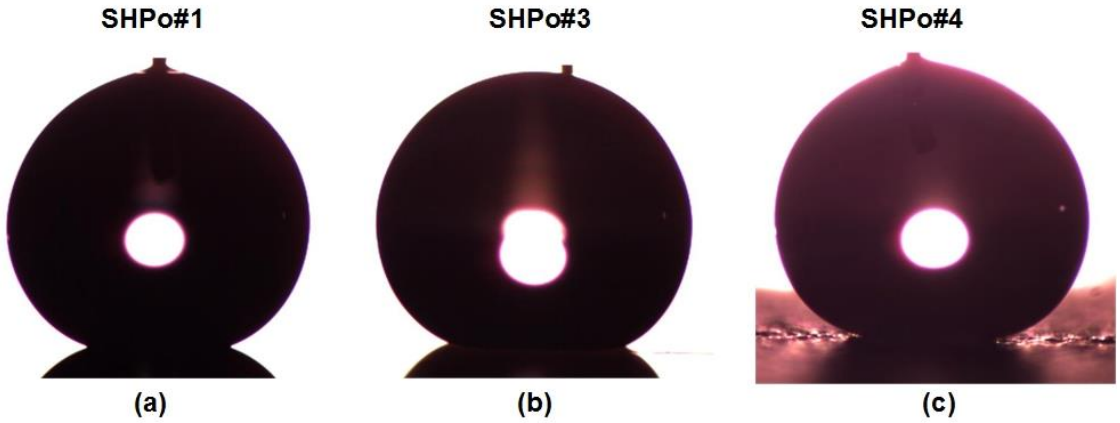

Figure 4-5 Contact angle on different SHPo surfaces used in drag reduction test. (a) silicon SHPo surface (SHPo#1). (b) Teflon FEP SHPo surface (SHPo#3). (c) NeverWet random SHPo surface (SHPo#4).

4.4 Low-Speed Water Tunnel Test

4.4.1 Flow Facilities and Testing Methods

The low speed water tunnel is the same as the one used in [6], as shown in Figure 4-6. The water tunnel has a test section of 610 mm × 50 m × 50 mm in the streamwise, vertical and spanwise directions respectively. The highest free stream speed is ~1.2 m/s and the testing section is ~0.45

m from the inlet, which corresponds to frictional Reynolds number $\mathrm{Re}_\tau = u_\tau \delta / \nu \sim 650$ at the testing section location base on the frictional velocity u_τ, boundary layer thickness δ (both estimated from the boundary layer theory [17] and verified using LDV in [6]) and kinematic viscosity ν. The flow condition at the testing section is fully developed turbulent boundary layer flow, as confirmed in [6] by matching the measured velocity profile with "log law" of turbulent flows and showing no effect of adverse pressure gradient.

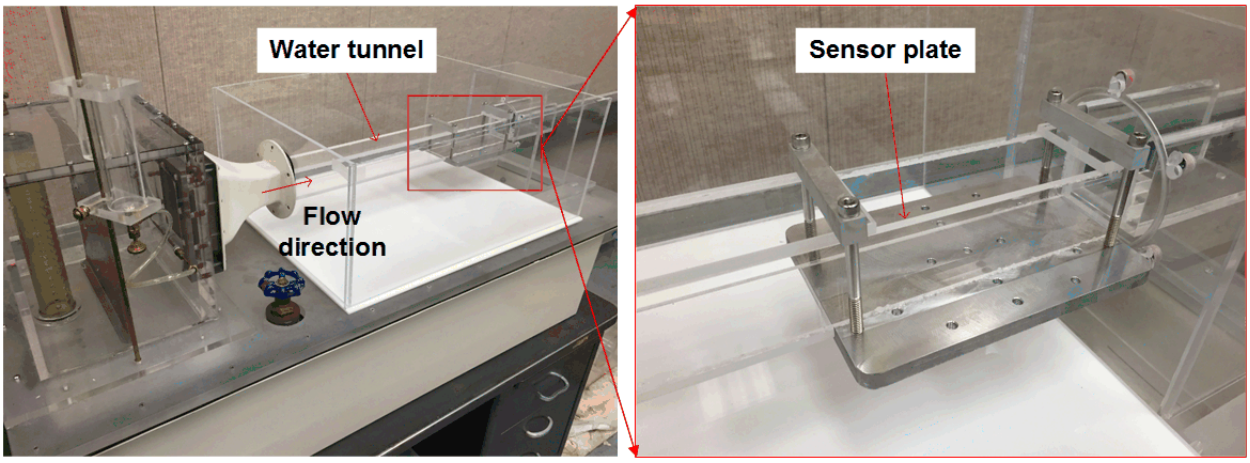

(a) (b)

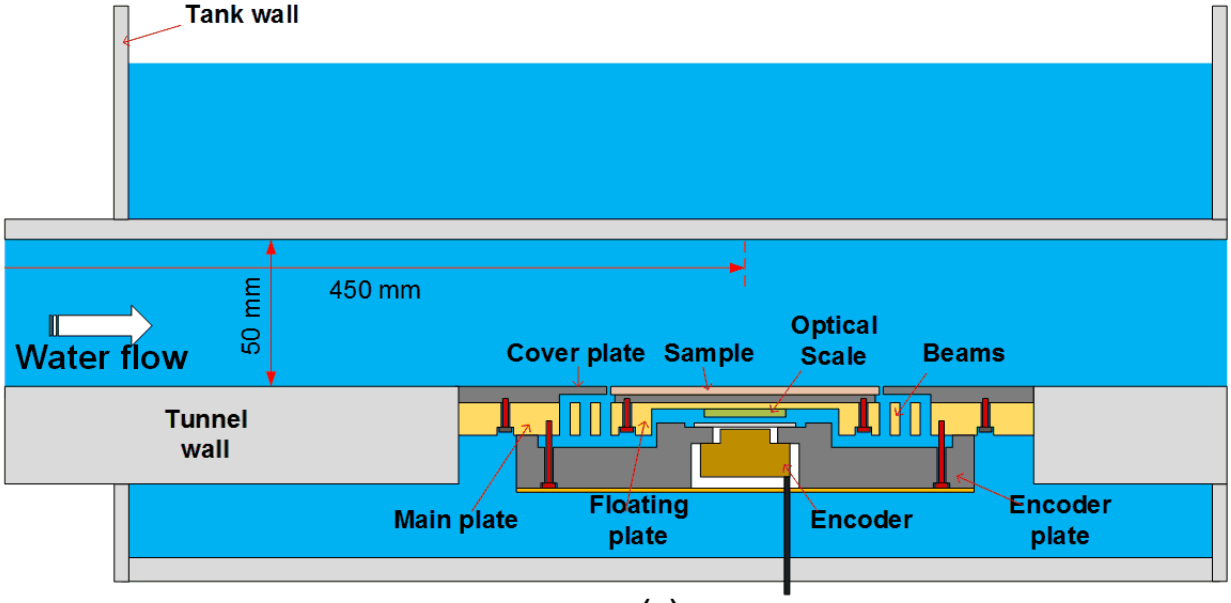

(c)

Figure 4-6 Picture and schematic drawing of low-speed water tunnel and shear sensor. (a) Picture of water tunnel and testing section. (b) Picture of attaching mechanism of shear stress sensor onto water tunnel. (c) Schematic drawing (not to scale) of the cross-section view of water tunnel and shear stress sensor.

The schematic drawing and pictures of the water tunnel is shown in Figure 4-6. The shear stress sensor discussed in previous chapter was installed at the bottom of the water tunnel to avoid big air bubbles floating on the top of the water tunnel. The air bubbles might cause a thick air layer formed on top of the microstructures of the SHPo surface, which will lead to over estimation of the drag reduction. However, the sensor plate was wider than the width of the water tunnel due to the length of the beam needed for high sensing resolution. To reduce the spanwise flow caused by leakage, a water tank was made to enclose the sensor. During the flow test, the tank was filled with water so that the static water pressure outside the tunnel in the tank is the same as that in the tunnel. When the flow pressure changed, the water leaked in or out will decrease or increase the water level in the tank, balancing the pressure across the water tunnel wall and suppressing spanwise flow.

4.4.2 Results

SHPo surface #1 composed of micro gratings was used in this test. The gratings had 50 μm pitch, 90% gas fraction and 60 μm grating height. The sample size was 2 cm x 7 cm. Figure 4-7(a) shows the skin friction coefficient of both smooth surface and SHPo surfaces at different Reynolds numbers by varying the flow speed in the water tunnel. The theoretical line is Equation (5-4) using the distance from the beginning of the water tunnel test section (i.e., virtual origin) to the center of the sample, which is 0.45 m. The skin friction coefficient in experiment showed good agreement with theoretical values. Figure 4-7(b) showed the drag ratio of SHPo surface over smooth surfaces.

Throughout the test, the SHPo surface stayed shiny (i.e., plastron existing), with no noticeable wetting transition. As the Reynolds number increased, the drag ratio started to decrease (i.e., drag reduction increases) with maximum drag reduction ~15% at highest speed. Moreover, drag reduction increased as the Reynolds number increased, consistent with the trend predicted in numerical studies [9, 22, 39] and observed in rheometer tests [32].

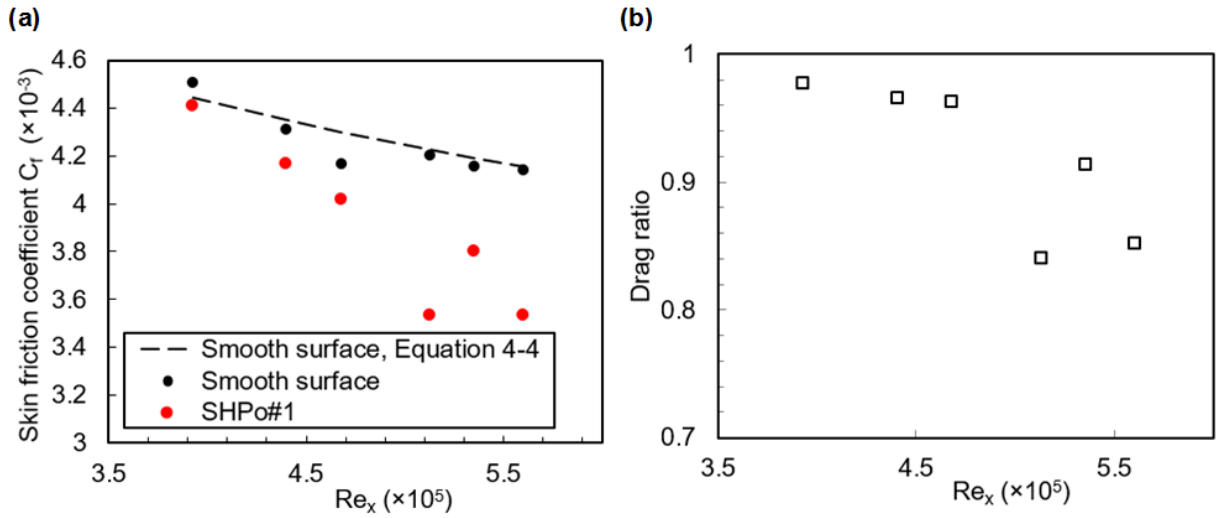

Figure 4-7 SHPo surface testing results in low-speed water tunnel. (a) skin friction coefficient of smooth and SHPo surfaces (b) drag ratio of SHPo surfaces in low-speed water tunnel.

4.5 High-Speed Water Tunnel Test

4.5.1 Flow Facilities and Testing Methods

Figure 4-8 shows the schematic drawing and the picture of the window used for high-speed water tunnel test at the Naval Underwater Warfare Center (NUWC) in Newport, Rhode Island. The main plate and the encoder were both inside the water tunnel with encoder sealed inside “encoder plate” and looking at the optical scale through a glass window. The encoder plate was attached onto the main plate using screws with cables come through the window through a watertight wire gripper.

Then the main plate was attached onto the window also with screws and vibration-absorbing spacer in between them. The top surface of the main plate was made flushed with the top surface of the window by adjusting the tightness of the screws.

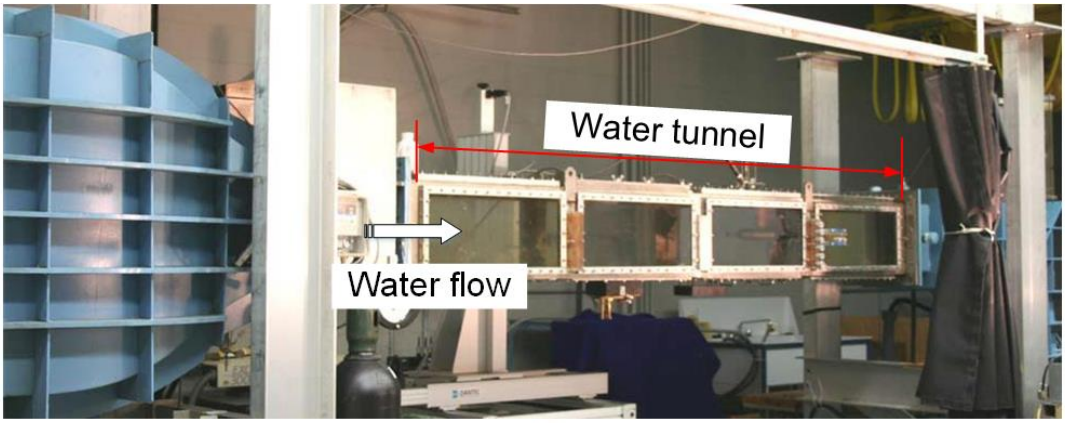

(a)

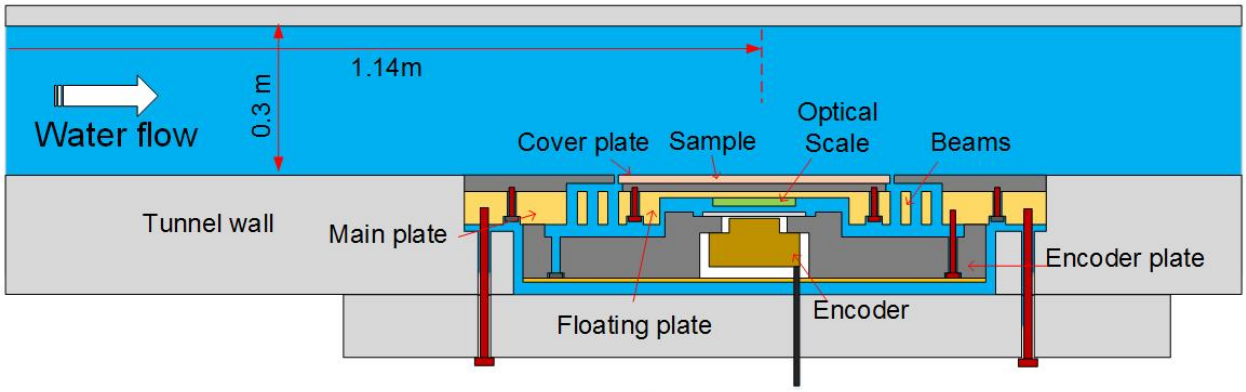

(b)

Figure 4-8 High-speed water tunnel experimental setup. (a) Picture of the high-speed water tunnel (provided by NUWC). (b) Schematics (not drawn to scale) of cross-section view of the water tunnel and shear sensor.

One issue when using the high-speed tunnel is the vibration problem. The large vibration from the pump, especially when the flow speed is high, may cause the floating plate to vibrate too much and hit the surrounding cover plate. To avoid the hitting, the gap between the floating plate and

the cover plate could be made very large but that will affect the measuring accuracy. Based on shear sensor analysis in previous chapter, this vibration system is a low-filter system where outside vibrations lower than the natural frequency tends to be filtered. One way to solve this problem is to increase the resonant frequency to be above environment noise frequency. The environmental vibration was measured to be 30-50 Hz. To increase the natural frequency of the folded beams, the floating plate and the sample holder were machined to be hollow, as shown in Figure 4-8, to reduce the weight. Another way to reduce the vibration of the floating plate is to use vibration absorbing material to damp the vibration transferred to the main plate. Vibration absorbing material "sorbothane" (Sorbothane Inc.) was used as spacer in between the main plate and the window.

Another issue of flowing tests is the air bubble generated in water because the pressure in the test section dipped below the atmospheric pressure at high speeds. Figure 4-9 shows the pressure-flow speed relationship of the high-speed water tunnel provided by NUWC. The water pressure was measured to go below the atmospheric pressure by as much as 5 psi at highest speed. The bubbles created in between the encoder plate and the main plate would block the path of the laser beam shining on and reflected from the optical scales. To solve this problem, water was highly degassed by removing the dissolved gas through boiling. The main plate and the encoder plate was assembled in the degassed water in a pot inside the water tunnel. After the water tunnel was filled with water, the sensor assembly was moved out of the pot and installed onto the water tank window. In this way, the water in between the encoder holder and the main plate would be undersaturated, slowing down gas bubble generation at high speed.

Actual experiments at the high-speed water tunnel were performed by Gintare Kerezyte with technical support from the team at NUWC.

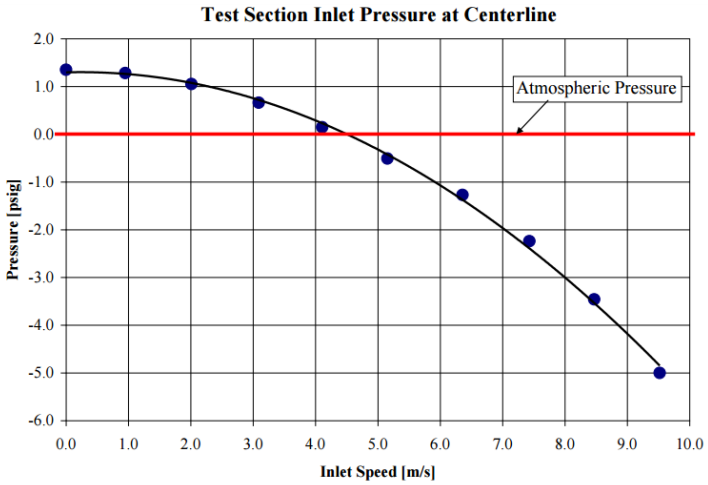

Figure 4-9 Pressure inside the high-speed water channel at different speeds (provided by NUWC)

4.5.2 Results

Three different SHPo surfaces have been tested: SHPo#1, SHPo#2, and SHPo#5. All the SHPo surface were silicon-based SHPo surfaces composed of micro gratings. Teflon AF 1600 was coated on the surface to ensure hydrophobicity. For each surface, three rounds of tests were conducted with the flow speed first increasing from the lowest to the highest speed, followed by decreasing to the lowest, and then increasing again. Figure 4-10 shows the skin friction coefficients and drag ratio for different SHPo surfaces. The skin friction coefficients of all SHPo surfaces were lower than that of the smooth surfaces. More specifically, the SHPo surfaces with smaller pitch (25 μm) showed higher skin friction coefficient and drag ratio compared with those of higher pitch (50 μm), consistent with the previous study [6]. The drag ratio decreases as the Reynolds number increased for all surfaces, clearly showing the Reynolds number effect. Drag reduction up to ~25% was obtained.

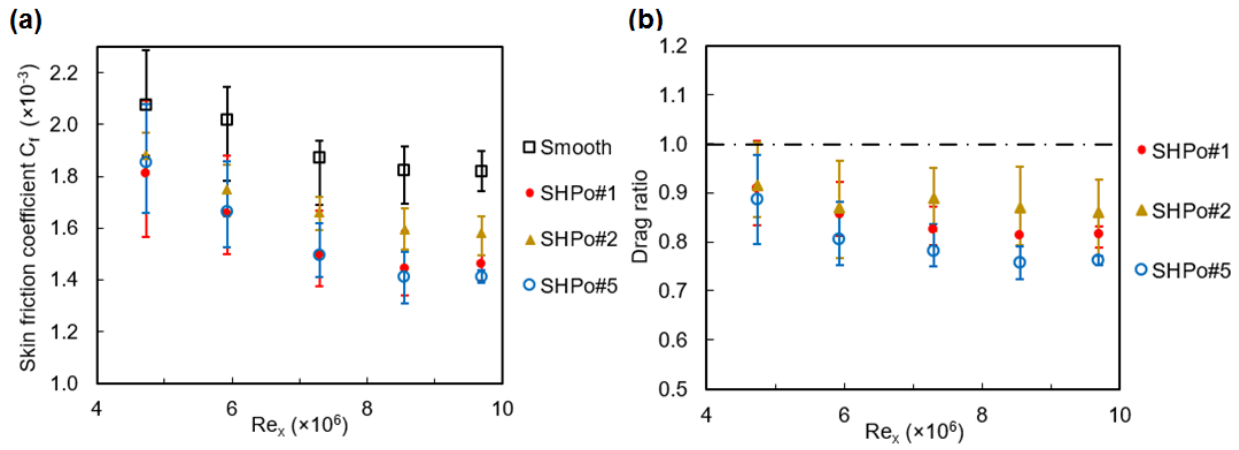

Figure 4-10 SHPo surfaces testing results in high-speed water tunnel. (a) skin friction coefficient and (b) drag ratio of different SHPo surfaces at different Reynolds numbers.

Compared with towing tank test discussed in next section, much less wetting was observed during the experiments even with similar Reynolds number range. We think this robustness of gas layer attributes to the supersaturated water (i.e., vacuum pressure as shown in Figure 4-9) in the water tunnel at high speeds. As shown in Figure 4-9, pressure inside the water tunnel dropped below atmosphere pressure after ~4 m/s, corresponding to $\mathrm{Re} \sim 4.7\times10^6$. In Figure 4-11, the surface dewetted at $\mathrm{Re} \sim 4.7\times10^6$, consistent with the pressure change. The negative pressure would first cause the existing gas inside the SHPo surface to expand, pushing the water out at wetted area. Meanwhile, since the water was supersaturated, gas started to diffuse into the plastron on SHPo surface. However, as the Reynolds number continues to increase, the front of the SHPo surface started to get wetted again possibly due to high shear and pressure fluctuation. The wetting caused the drag ratio to increase again at the highest speed (Figure 4-10(b)). All in all, this is the first time that Reynolds number effect was observed in high speed water tunnel, showing the wetting transition is the key element that prevented the Reynolds effect showing up in other studies [30].

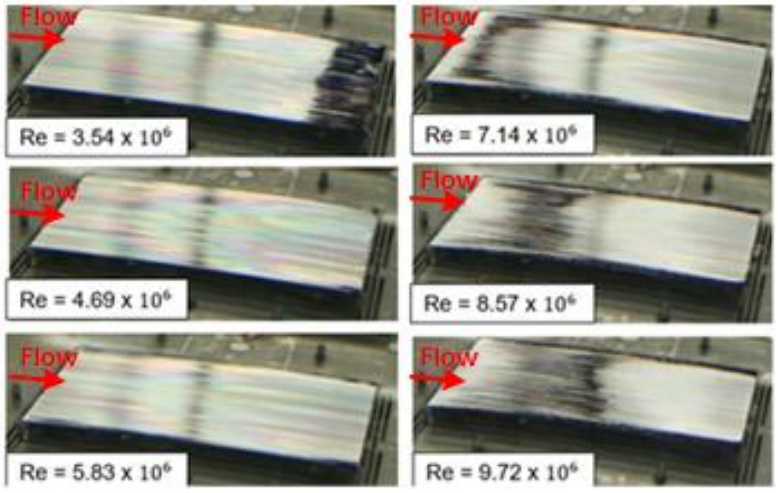

Figure 4-11 Pictures showing wetting of SHPo#1 at different speeds during high-speed water channel experiments. Other types of SHPo surfaces had similar wetting behavior.

4.6 High-Speed Towing Tank Test

4.6.1 Flow Facilities and Testing Methods

4.6.1.1 Towing Tank Facility and Shear Sensor Attachment

Towing tank facility (95.4 m long, 3.6 m wide, and 1.8 m deep) at the Davidson Laboratory of the Steven Institute of Technology was used to create high-speed TBL flows. The aluminum towing plate shown in Figure 4-12 is 1.4 m long, 0.7 m wide and 0.02 m thick. As shown in Figure 4-12(a)(b), the towing plate is suspended vertically in the tank by two struts, which in turn hang from a carriage rail. As can be seen from the figure, the rotating axis is kept at an angle from the moving direction. This design is to reduce the yaw angle caused by asymmetry of the towing plate. The asymmetry could not be avoided because our towing plate was too thick for the clamp and thus screwed in to the center from one side. When the towing plate is not symmetric, a pressure difference on two sides of the plate will cause the plate to turn. However, the none parallel rotating axis will cause the plate to have an angle of attack, which will balance the pressure difference

caused by the pressure asymmetry. Meanwhile, an inclinometer is attached to the top of the towing plate so the yaw angle could be measured in real time. The technical team at the Davidson Laboratory has supported the experiments.

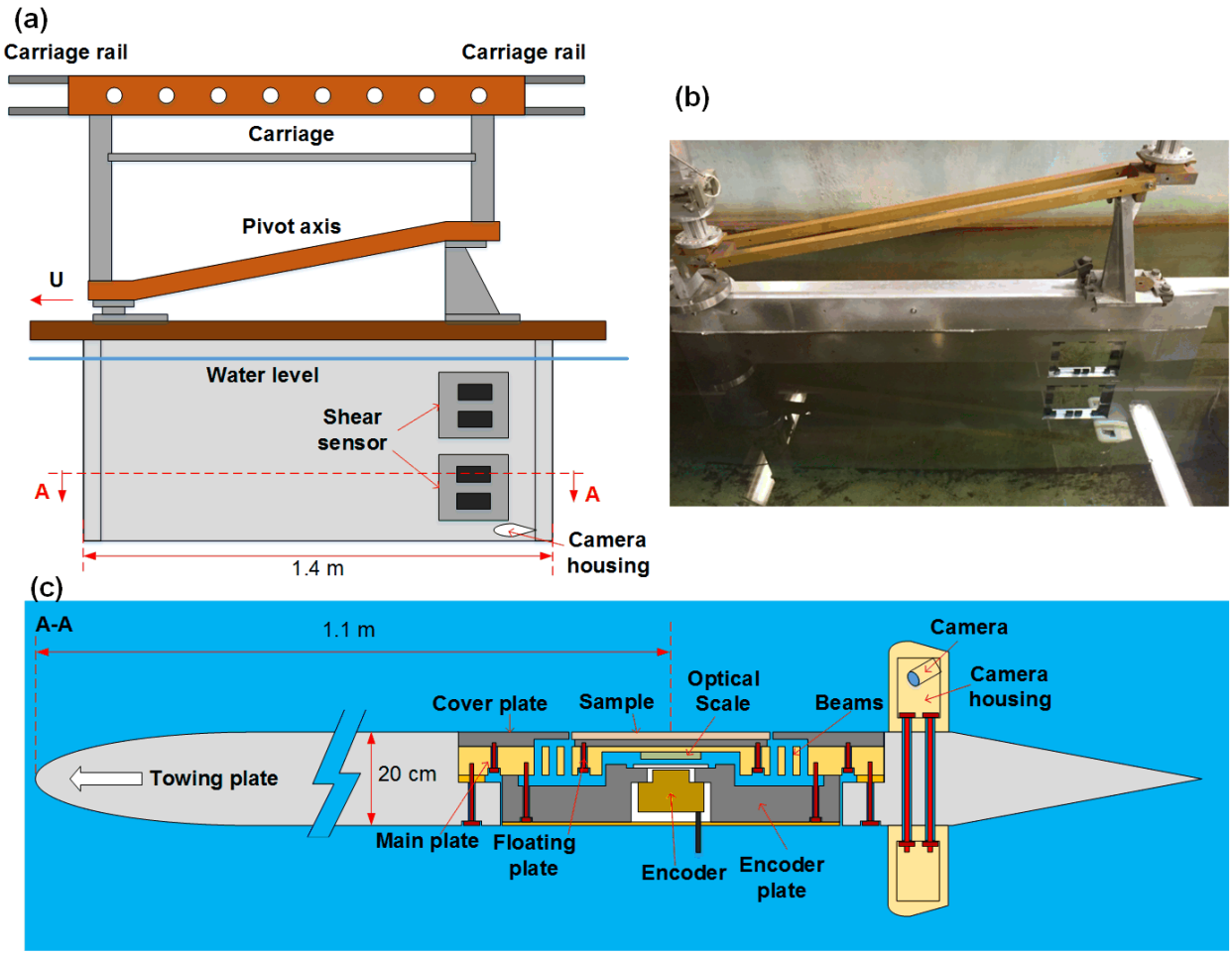

Figure 4-12 High-speed towing tank experimental setup. (a) Schematics (not drawn to scale) of towing tank experimental setup. (b) Picture of the towing plate. (c) Schematics (not drawn to scale) of cross-section view of the shear sensor.

Figure 4-12(c) shows the schematic cross section drawings of the sensor attachment. The shear stress sensor was attached onto the towing plate using screws. To eliminate any potential bubble trapped in between the encoder plate and the main plate, the encoder plate was installed underwater

onto the main plate after bubbles were carefully blown away from the back of the main plate. The encoder cables went through a slot on the back of the towing plate, which was sealed by tape to reduce the disturbance. The shear stress sensor was installed and tested at different speeds.

4.6.1.2 Honeycomb Towing Plate Development

The towing plate shown in Figure 4-12(b) was made wide (tall) to increase SHPo surface immersion depth and made thick to make sure the shear sensor was flush with the plate surfaces on both sides. Compared with the previous towing tank test [13], the increased thickness of our towing plate would lead to two problems: (1) difficult handling due to the increased weight (2) bigger splash at high speed due to increased thickness. To solve these two problems, (1) we made the inside of the plate hollow with honeycomb structure to reduce weight while keeping the structural strength. The weight was eventually reduced more than 50% compared with solid plate. (2) We shaped the front and rear end of the plate streamlined (by American Best Manufacturing, Burbank, CA) to reduce the wave and splash during high-speed tests.

As shown in Figure 4-13, the honeycomb panel with aluminum honeycomb in between two thin aluminum sheets was made by Kerr Panel Manufacturing (KPM) in Henderson, Colorado, to form the main body of the towing plate to reduce weight. The front and rear end parts were made streamline shape was designed by us and machined by American Best Engineering in Burbank, California, and inserted into the honeycomb panel to reduce the wave and drag caused during the high-speed test. The solid bars on the sides are used to increase the strength of the whole plate. All the seams and gap were sealed using underwater epoxy to ensure watertight sealing of the honeycomb. Two openings were made on the sensor plate holder at different positions to hold the shear stress sensor at different immersion depth.

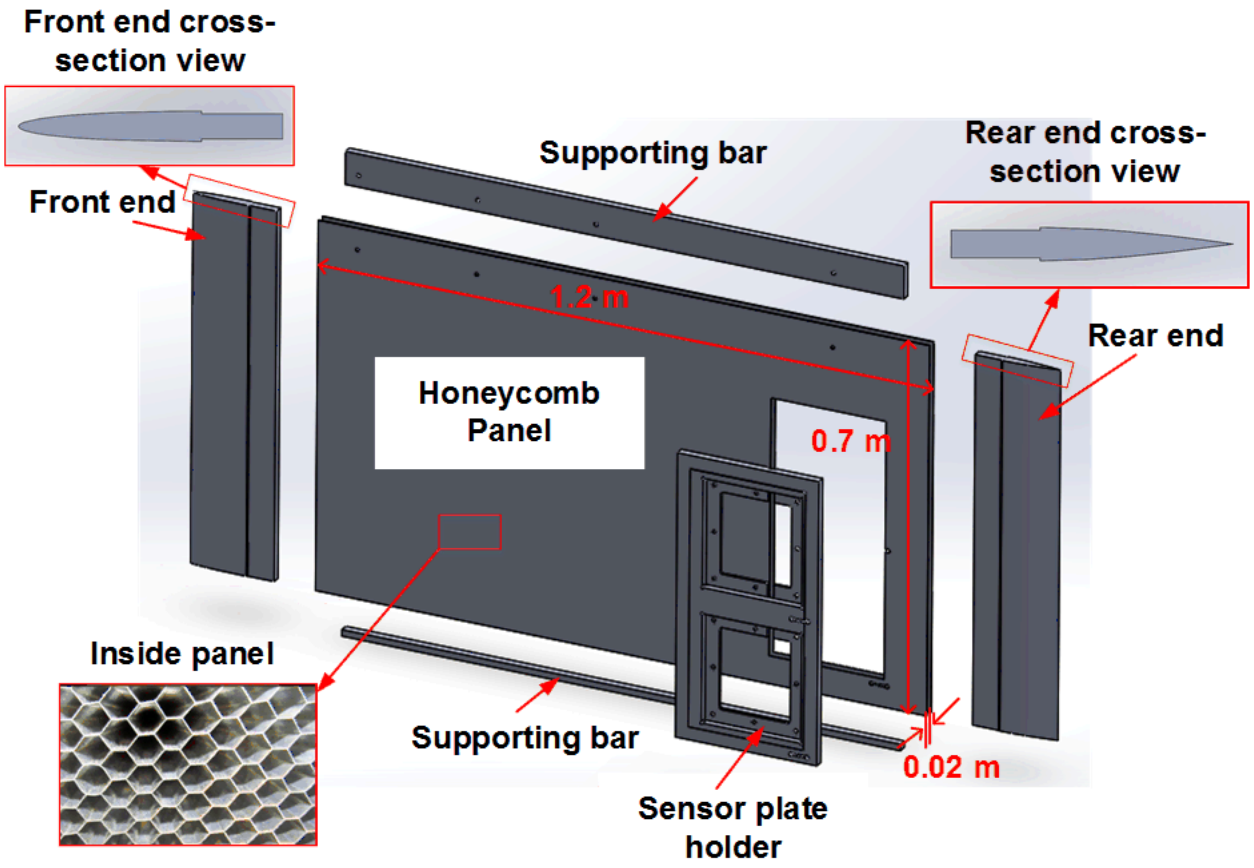

Figure 4-13 Design of the honeycomb towing plate for towing tank test.

4.6.1.3 Compact Real-Time Underwater Camera Development

Monitoring the SHPo surface wetting during the test is crucial to understand the drag data, as shown later in the results. Unfortunately, no commercial underwater camera was found small enough to fit into the camera housing that we designed to be streamlined and small enough in order to minimize the drag and disturbances against the towing experiment. Also, most commercial underwater cameras can only do recording instead of real-time monitoring, which is critical for us to identify any potential problems right away during the test. To solve this problem, we have developed our own underwater miniature camera system.

The camera used here is a spy camera (Adafruit) designed for Raspberry Pi computer. The small size (8.5 mm tall, 11.5 mm long and wide) of the camera allows us to fit it into a small camera housing with streamlined shape. Figure 4-14 shows the configuration of camera system. The camera was first sealed into a metal case with a removable glass top, which allowed easy adjustment of the focal length of the camera by twisting the camera lens and re-seal. The camera case was then placed into the housing with adjustable viewing angles. Using a 2-meter ribbon cable, the camera was connected to the main Raspberry Pi computer, which was controlled remotely. Once immersed in water, the glass window on the housing was open to fill the void inside the housing with water to avoid any image distortion. Then a thin rubber band was used to fix the glass window underwater at high speeds. This underwater camera was developed together with undergraduate student Jeong-Won Lee.

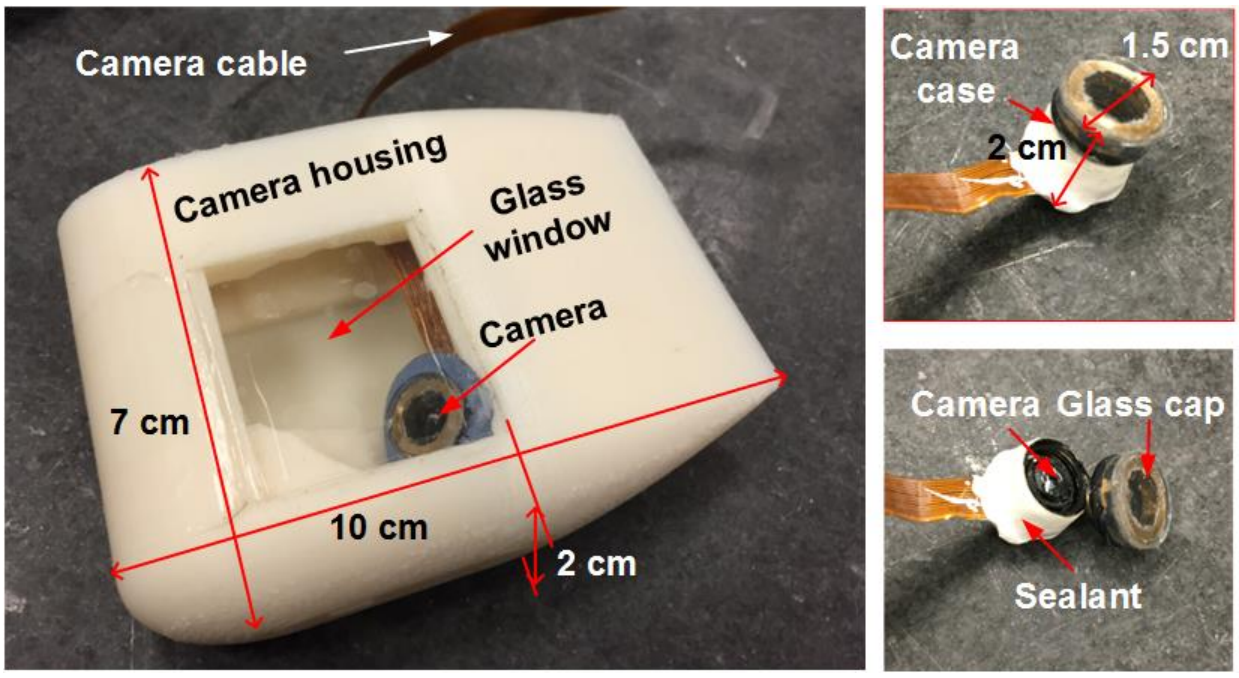

Figure 4-14 Design of underwater camera for real-time SHPo surface monitoring

4.6.1.4 Drag Ratio on Dewetted Area of SHPo Surfaces

For SHPo surface with massive wetting during the experiments, we also extracted the drag ratio only for dewetted area (i.e., Cassie state). When there are both wetted and dewetted areas on the SHPo surface at the same time, the drag ratio of the whole SHPo surface D_{total} is the weighted average of drag in wetted area and dewetted area:

$$D_{total} = D_w S_w + D_c S_c = D_w S_w + D_c (1 - S_w) \tag{5-5}$$

D_w and D_c are the drag ratio of the wetted area (i.e., Wenzel state) and dewetted area (i.e., Cassie state), S_w and S_c are the area ratio for wetted area and dewetted area, respectively. We first obtained the area ratio of wetted area by calculating the ratio of dark area S_w from the picture of SHPo surface using ImageJ. We then experimentally measured the drag ratio of wetted area (i.e., Wenzel state) D_w for each sample at different speeds by intentionally wetting the whole SHPo surface. Then Equation (5-5) was used to obtain the drag ratio of dewetted area (i.e., Cassie state) D_c.

4.6.2 Results

Figure 4-15(a) shows the skin frictional drag coefficient (C_D) of the reference (smooth) and different SHPo surfaces measured at speed range of 2-10 m/s. The value of theoretical skin frictional coefficient is determined using Equation (5-4) with the distance between the sample center and the leading edge being 1.1 m. The theoretical skin friction coefficient shows good agreement with the experimental data with smooth surfaces. The four separate runs of the smooth surface correspond to four separate installments for the test setup to show the repeatability of the shear stress sensor measurement as well as the repeatability of the flow conditions. Figure 4-15(b)

shows the drag ratio of different SHPo surfaces compared to the smooth surface. The detail geometry and dimension of the surface structure for different SHPo surface is shown in Table 4-2.

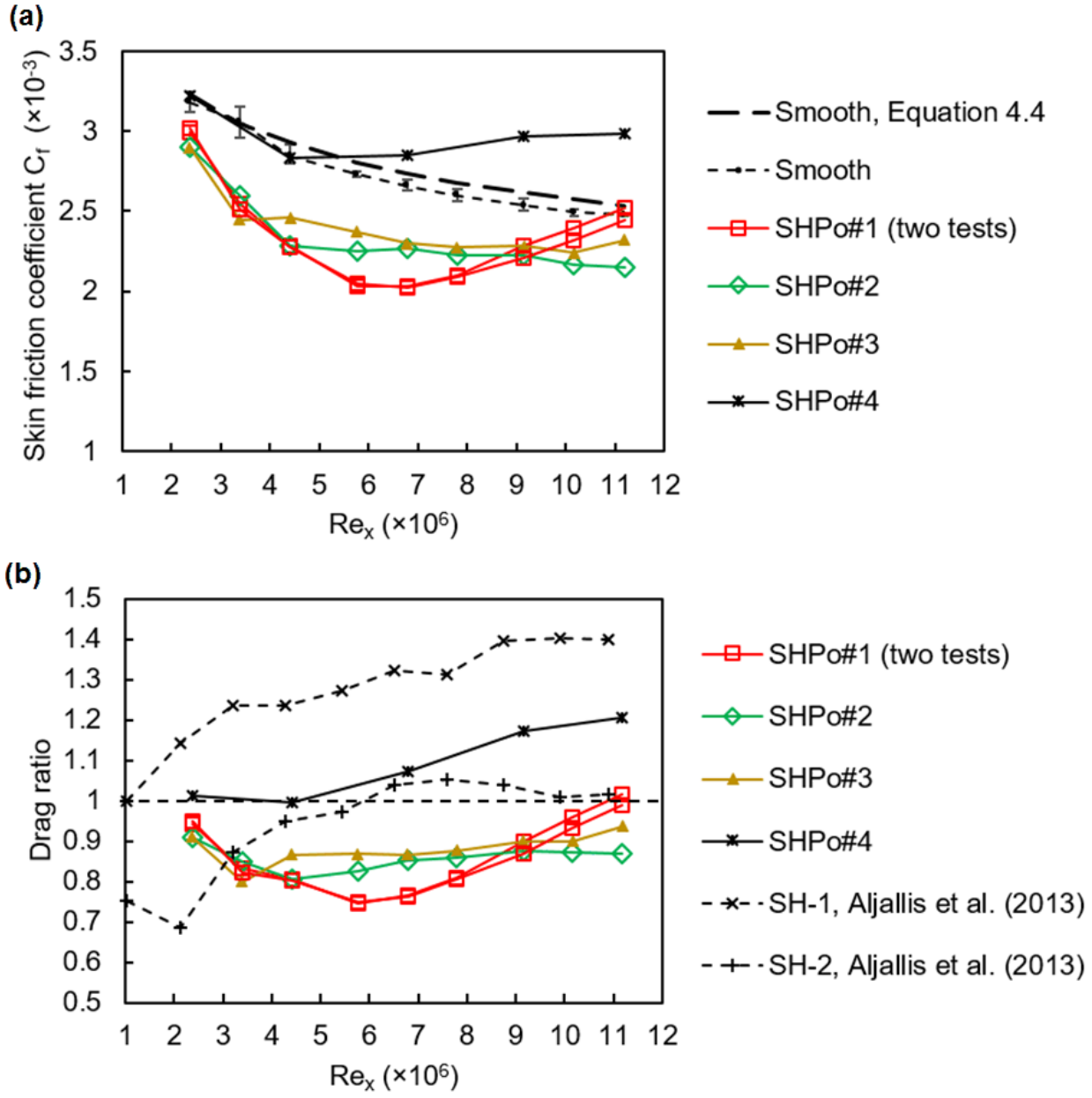

Figure 4-15 SHPo surfaces testing results in high-speed towing tank. (a) Skin friction coefficient of smooth and different SHPo surfaces tested in high-speed towing tank. (b) Drag ratio of different SHPo surfaces tested in high-speed towing tank.

For silicon SHPo surface with 50 μm pitch, 90% gas fraction and 60 μm trench depth (SHPo#1), the drag ratio first decreases by 25% to about 75% as the Reynolds number increases. However, after $\mathrm{Re} \sim 6\times10^6$, the drag ratio starts to increase as the Reynolds number increases and eventually reaches 100 %, which indicate no drag reduction. The trend of drag change matches well with the wetting behavior of the SHPo surface, as shown in Figure 4-16. Before $\mathrm{Re} \sim 6\times10^6$, most area of the surface stays bright (dewetted), indicating the existence of gas. Then as the Reynolds number increases passing $\mathrm{Re} \sim 6\times10^6$, massive wetting started to show up at the front of the sample and expands as the Reynolds number increased. Eventually, more than half of the area got wetted and the total drag increased to similar as smooth surface (i.e., no drag reduction).

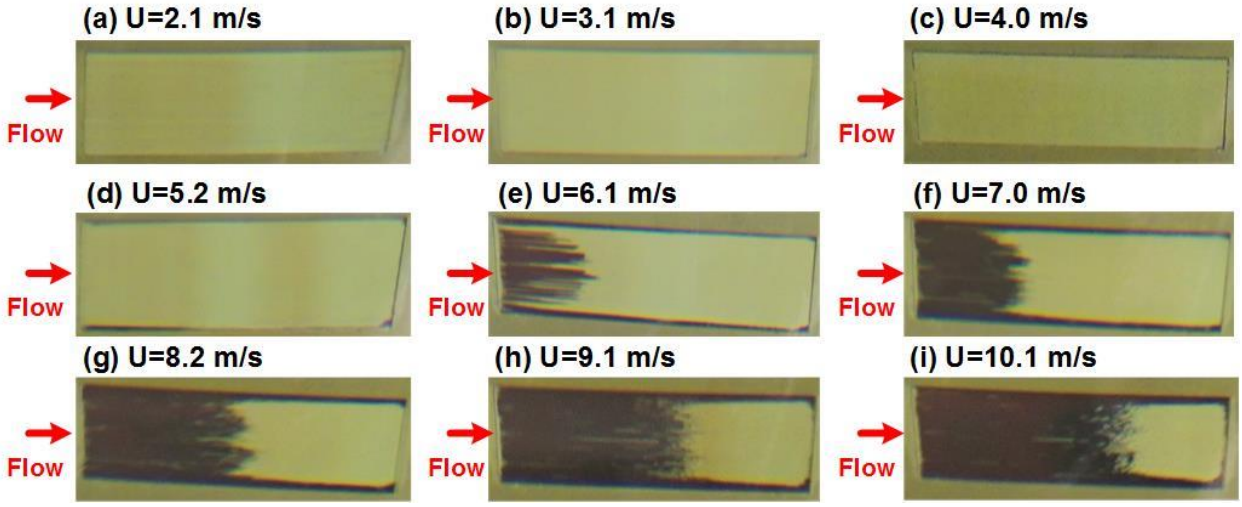

Figure 4-16 Pictures of SHPo surface (SHPo#1) showing wetting area after each testing speed. SHPo surface is the rectangle shape in the center of each picture. Dark area indicates wetted state (Wenzel) while bright area indicates dewetted state (Cassie). Flow direction is from left to right. From (a) to (i), the flow speed increases.

For the drag ratio curve on Si SHPo surface with 25 µm pitch, 90% gas fraction and 25 µm trench depth (SHPo#2), the trend is similar as the one for 50 µm pitch SHPo sample. Meanwhile, the skin friction drag and drag ratio are higher than 50 µm pitch SHPo sample, as predicted in computational studies [22] and experiments [6]. The trend of drag change also matches the wetting behavior of the SHPo surface (Figure 4-17). Before $\mathrm{Re} \sim 5\times10^{6}$, most of the surface stays dewetted and the drag decreased with the Reynolds number increasing. However, after $\mathrm{Re} \sim 5\times10^{6}$, massive wetting (dark area) started to show up in the front of the sample and the total drag started to increase, as shown in Figure 4-17(d). Due to the lack of reentrant structures (Figure 4-4(b)), the wetting started earlier than SHPo#1 tested previously. Meanwhile, different from 50 µm pitch SHPo sample, the drag increased slower as Reynolds number increases after the threshold, maintaining ~13% drag reduction eventually even at highest Reynolds number of $\mathrm{Re} \sim 1.1\times10^{7}$.

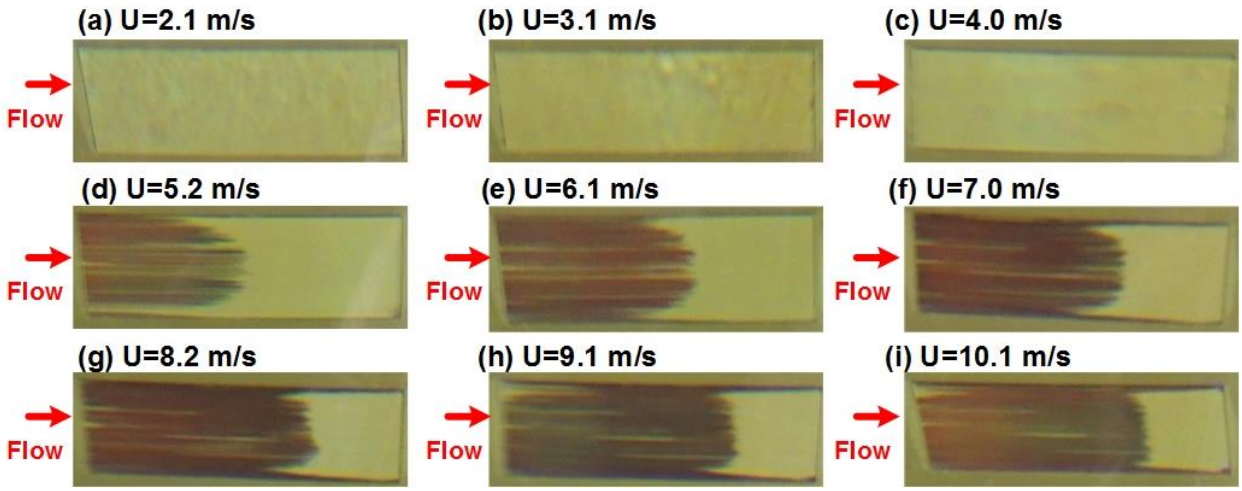

Figure 4-17 Pictures of SHPo surface (SHPo#2) showing wetting area after each testing speed. SHPo surface is the rectangle shape in the center of each picture. Dark area indicates wetted state (Wenzel) while bright area indicates dewetted state (Cassie). Flow direction is from left to right. From (a) to (i), the flow speed increases.

For the drag ratio curve of FEP SHPo surface with 50 µm pitch, 85% gas fraction and 40 µm trench depth (SHPo#3), the Reynolds number ($\mathrm{Re} \sim 4\times10^{6}$) where the drag start to increase is smaller compared to that of silicon SHPo surface. Possibly due to the lack of reentrant edge and rounded corners on the top of the trench, as shown in Figure 4-4(e), the surface wetted more than silicon SHPo surfaces which leads to higher drag, as shown in Figure 4-18. As the Reynolds number increases, the drag ratio first decreases by ~18% at $\mathrm{Re} \sim 3.5\times10^{6}$ and then the reduction increased back to ~5% at the highest Reynolds number.

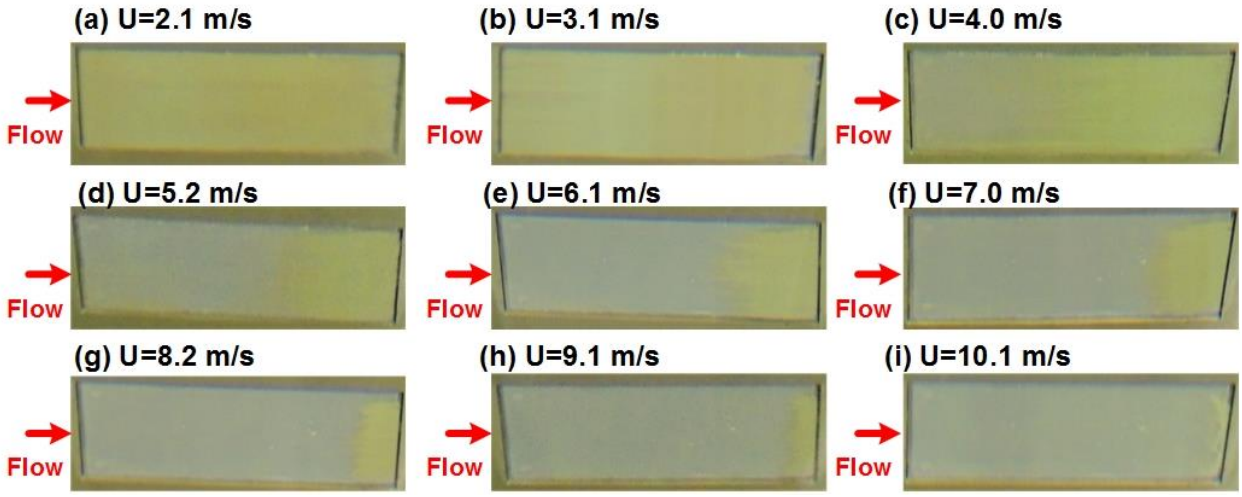

Figure 4-18 Pictures of SHPo surface (SHPo#3) showing wetting area after each testing speed. SHPo surface is the rectangle shape in the center of each picture. Grey area indicates wetted state (Wenzel) while yellow area indicates dewetted state (Cassie). Flow direction is from left to right. From (a) to (i), the flow speed increases.

For the rough NeverWet surface (SHPo#4), the drag ratio is above that of smooth surfaces for all speeds, indicating drag increase (Figure 4-15). However, no significant wetting was observable even at highest speed (Figure 4-19). As summarized in [7] over several independent studies, NeverWet surface might have drag reduction at low Reynolds number turbulent flow depending

on the surface roughness and flow condition (e.g., pressure, water saturation). However, all previous studies [7, 13] showed NeverWet surface cannot have drag reduction in high Reynolds number turbulent flow.

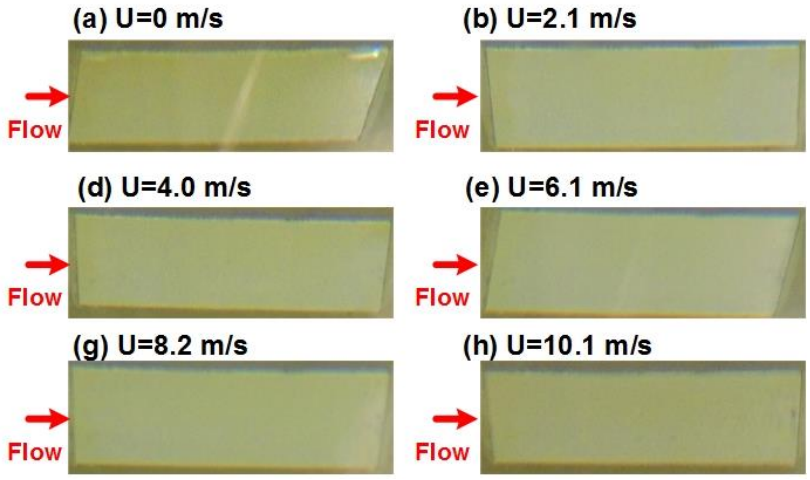

Figure 4-19 Pictures of SHPo surface (SHPo#4) showing no wetting area after each testing speed. SHPo surface is the rectangle shape in the center of each picture. Flow direction is from left to right. From (a) to (i), the flow speed increases

4.6.3 Discussion

Firstly, drag ratio reduced significantly down to ~75%, providing a significant drag reduction (~25%) for the first time at Reynolds numbers up to $\mathrm{Re} \sim 6\times10^{6}$ in towing tank facility, demonstrating the robustness of our silicon-based SHPo surface against wetting. Secondly, drag reduced more with higher Reynolds number, confirming the Reynolds number effect on the drag reduction predicted numerically. As discussed in section 6.1.4, the effect of Reynolds number on turbulent drag reduction has been an open-ended topic. In both numerical [8, 22] and rheometer/microchannel experiments [26, 32], the drag reduction has been confirmed to increase with the Reynolds number. However, in larger-scale, fully developed turbulent boundary layer

flow, the opposite trend was observed [7]. To our best knowledge, this is the first time that drag reduction increasing with Reynolds number has been observed in fully developed TBL flow.

The consistency between wetting and drag ratio supports our argument that wetting is the main reason for drag increasing after $\mathrm{Re} \sim 6\times10^{6}$. To calculate the drag ratio of only dewetted area after mass wetting had occurred, the skin friction coefficient of wetted area was first measured for Equation (5-5). The samples are wetted right after previous drag reduction test at all speeds. Figure 4-20 shows the skin friction coefficient of wetted (Wenzel) area for different SHPo surfaces at different speeds. Interestingly, for SHPo surface with 50 μm pitch (SHPo#1), the skin friction coefficient first decreased and then increased as the Reynolds number increased. For SHPo surface with 25 μm pitch (SHPo#2), the skin friction coefficient first decreased as Reynolds number increased.

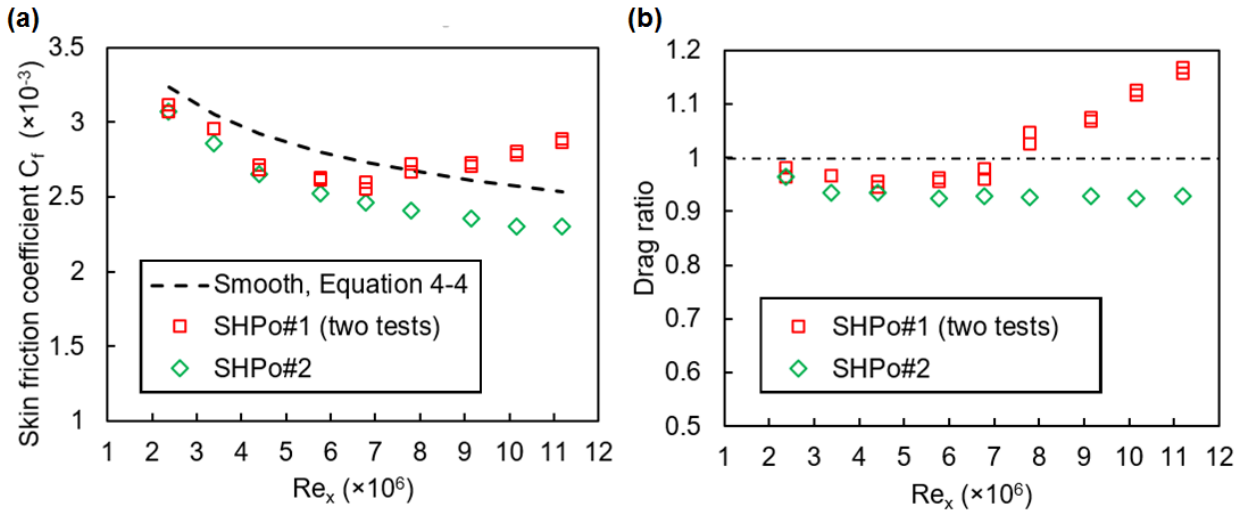

Figure 4-20 Skin friction coefficient of completely wetted SHPo surface at different speeds in towing tank test.

For the interesting trend shown in Figure 4-20, riblet drag reduction was applied to explain the results. As shown in Figure 4-21, $l_g^+ = \sqrt{A}/\delta$ where A is the cross-section area of the space in between two gratings and δ is the turbulent boundary layer wall unit. We obtained the relationship between drag ratio and l_g^+ for different SHPo surfaces at different Reynolds numbers. For SHPo surface #1, l_g^+ is larger due to large pitch while SHPo surface #2 has smaller l_g^+. Figure 4-21 (a) is the experimental (solid circle) and numerical results (void triangle) for riblet structure [40]. The experimental trend in Figure 4-20(a), reproduced here as Figure 4-21*Figure* (b) for convenience, matches the results for riblet structures in Figure 4-21 (a) with minimum drag ratio near $l_g^+ \sim 10$. This result suggests the SHPo surface in Wenzel state performed like riblet structures, providing drag reduction in only a certain range of Reynolds numbers.

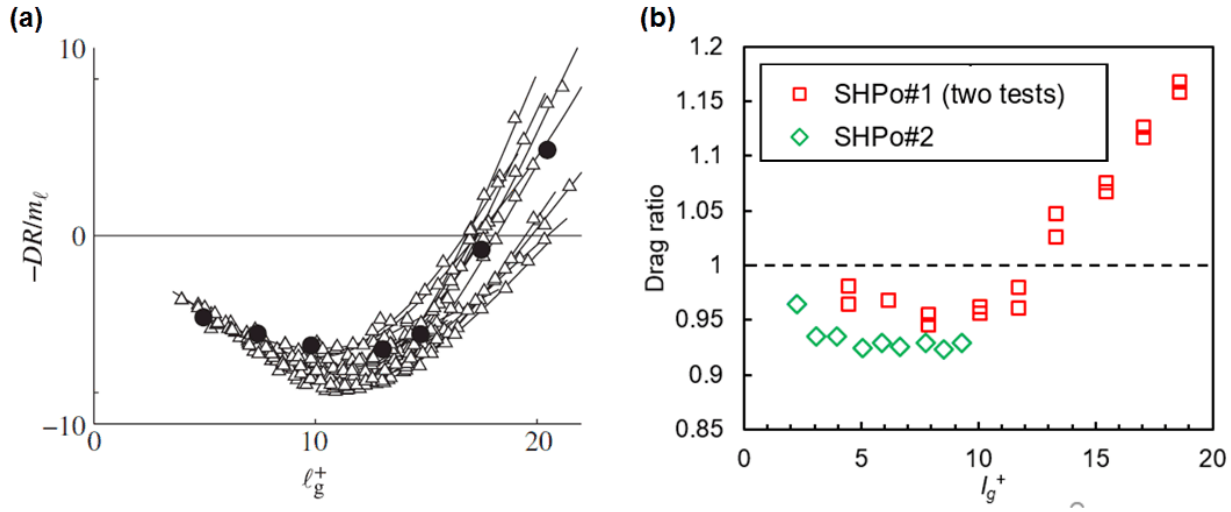

Figure 4-21 Drag ratio of riblet drag reduction and completely wetted SHPo surfaces. (a) Previous experimental (solid circle) and numerical (void triangle) studies [40] on riblets structure drag reduction showing relationship between drag ratio and nondimensionalized l_g^+. (b) Relationship

between drag ratio and nondimensionalized l_g^+ for two different SHPo surfaces in Wenzel state at different Reynolds numbers.

Using Equation (5-5) and the skin friction coefficients obtained in two tests, the skin friction coefficients and drag ratio only for the dewetted area were calculated and plotted in Figure 4-22(a). Two tests with the same SHPo surface of 50 μm pitch (SHPo#1) showed good consistency in skin friction coefficient and drag ratio. A SHPo surface with 25 μm pitch (SHPo#2) showed higher skin friction coefficient and drag ratio compared with SHPo#1, consistent with previous studies [6], which reported a more drag by a large pitch. Figure 4-22(a) indicates that the drag would decrease to as low as 60% (i.e., drag reduction as much as 40%) if the SHPo surface stayed without any wetting in high Reynolds number flow. This resistance against wetting would be difficult for passive surfaces with similar geometry scale. The current surfaces of SHPo#1 already had reentrant structures at the top of the grating to enhance the air-water meniscus robustness. To overcome this wetting transition, active surfaces that could restore Cassie state [41] after wetting transition would be needed.

After obtaining the drag ratio data for dewetted area on SHPo surfaces, we apply analytical equation concluded from previous numerical [21] and experimental study [32] for SHPo surface drag reduction to obtain the dimensionless slip length:

$$b^+ = \frac{U_\infty}{u_{\tau 0}} \cdot \left(\frac{1}{\sqrt{Drag}} - 1\right) - \frac{1}{\kappa} \log\left(\sqrt{Drag}\right) \tag{5-6}$$

The obtained dimensionless slip lengths at different Reynolds number was plotted against $\sqrt{\mathrm{Re}}$ and shown in Figure 4-22(b). From the figure, it is evident that b^+ is linear to $\sqrt{\mathrm{Re}}$ for both types

of SHPo surfaces. This result matches the SHPo surface drag reduction test results obtained in rheometer test [32].

The experimental data was also compared directly with the numerical data in [21], as shown in Figure 4-22(c)(d). The dimensionless width of shear free interface is: $d^+ = u_\tau d/\nu$. The friction velocity is obtained from experiment skin friction data: $u_\tau = \sqrt{\tau/\rho} = \sqrt{0.5 C_f U^2}$. The width of shear free interface $d = Pitch \cdot GF$ is the spacing between two gratings. Even though the numerical study [21] didn`t cover d^+ range in the experiment, the experimental data generally match the extension line converging to point (0, 1) indicating smooth surface. Note that the numerical study assumes flat air-water interface flush with the top of the surface microstructures, while the air-water interface in actual experiment tends to bend downwards and slide down into the micro-structures. This deviation from the flat-flush assumption is known to decrease the slip length, and will compromise drag reduction according to other studies on turbulent flow [18, 42].

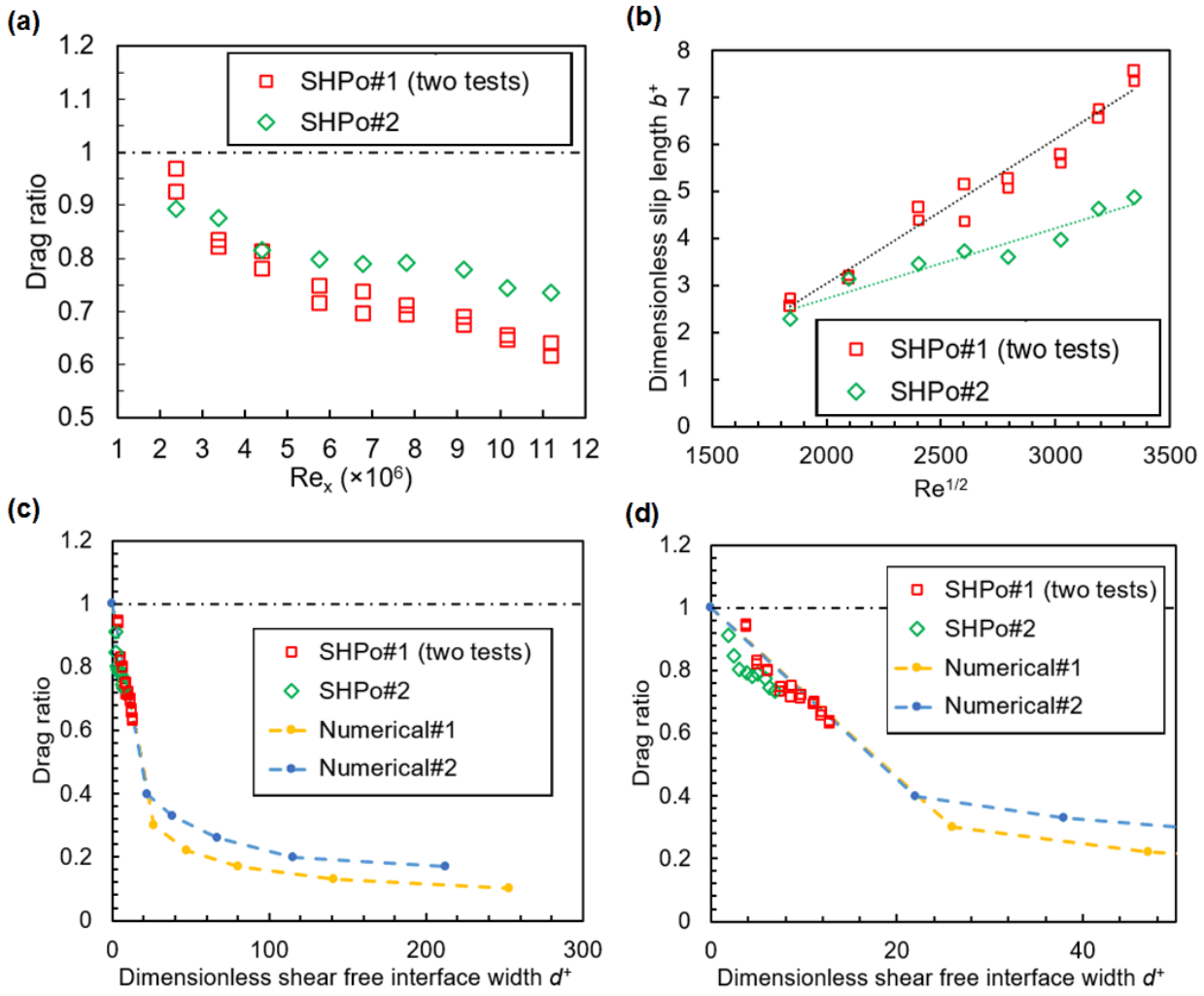

Figure 4-22 Drag ratio on SHPo surfaces considering only the dewetted area (i.e., Equation (5-5)). (a) drag ratio of the dewetted area on different SHPo surfaces at different Reynolds numbers. (b) Dimensionless slip length that is obtained using Equation (5-6) from numerical study [32] at different Re. The dash lines are linear fit to both types of SHPo surfaces. (c)(d) Variations of drag ratio with the dimensionless width of shear free interface (d^+). The numerical data are from [21] for grating SHPo surfaces. Numerical#1: Gas fraction = 91.7%, $\mathrm{Re}_{\tau,in}=140$. Numerical#2: Gas fraction = 87.5%, $\mathrm{Re}_{\tau,in}=200$. The drag ratio-d+ relationship is independent of Reynolds number in [21].

4.7 Demonstration of SHPo Surface Drag Reduction in Field Test

4.7.1 Motivation

As described in Chapter 1, reducing the frictional drag of marine vessels would have a substantial impact both economically and environmentally [43]. However, while a few studies were reported using small model boats [10, 11] or model submarine [12] at low Reynolds numbers ($\mathrm{Re}_x \sim 10^4 - 10^5$), there has been no field test of SHPo surface on actual marine vessel at high Reynolds numbers. Most of the turbulent drag reduction tests of SHPo surfaces were conducted in water tunnel, rheometer or even micro-channels, where flow condition and other environmental conditions were quite different from the flow near marine vessel in seawater. One test that are closest to marine vessel conditions is the towing tank test [13]. However, no drag reduction or even drag increasing was observed at high Reynolds number.

For actual field test, there has been few suitable sensor for evaluating SHPo surface drag reduction. Covering the whole ship with SHPo surface and conduct long-term trip test would be too expensive and time-consuming. Moreover, the long-term fouling of SHPo surface and gas replenishing after wetting remain a problem. For small sample of SHPo surface, there lacks a reliable sensor that can be incorporated into the hull of marine vessels while providing high resolution and robustness against environmental change. The commonly used piezoelectrical sensor [30] is usually too bulky and sensitive to temperature and pressure fluctuation in field test. Other equipment used in experiment environment like PIV or LDV are also too bulky for marine test. Furthermore, the robustness of SHPo surface at high Reynolds number is another critical issue. As shown by Aljallis et al. [13], even random-structured SHPo surface with nanoscale roughness may get partially wetted in high Reynolds number flow, causing loss of drag reduction capability.

Here, we conducted the first field test on a boat in seawater using the newly-developed sensor discussed in Chapter 2. First, the sensor developed is compact enough to be incorporated into boat hull. It also has high resolution to sense small shear force applied on our small (4 cm x 7 cm) SHPo surface sample and high robustness against the environmental parameters change during the field test. Second, the reentrant structure on silicon SHPo surface makes it robust against wetting transition as high as $\mathrm{Re}_x \sim 4\times10^6$.

4.7.2 Testing setup on modified boat

A Boston Whaler boat was modified for this test. A picture of the boat is shown in Figure 4-23(a). The boat hull is 13.3 feet long, 5 feet wide and 2 feet tall. With three people on board, it has a draught of ~30 cm. The boat is powered by one engine in the back and the maximum speed with three people on board is about 10 knots (~5 m/s).

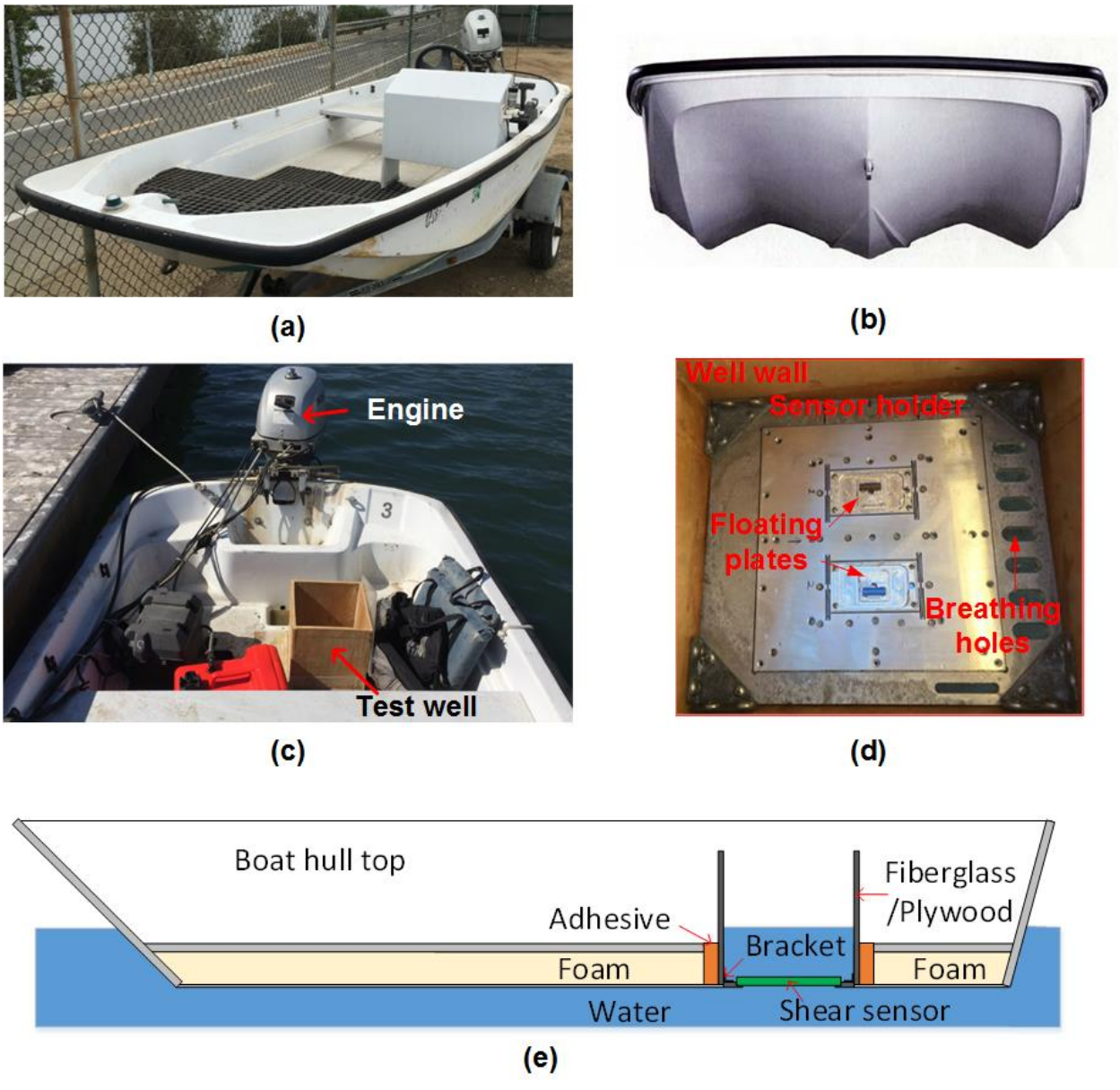

Figure 4-23 Pictures of the experiment setup of the modified boat. (a) 13' Boston Whaler boat used in the test (b) Shape of the boat hull viewed from the front. (c) Customized well in the boat (d) top view of the test well and the sensor holder. (e) Schematic cross section view (not drawn to scale) of the boat and sensor.

To be able to incorporate the shear sensor onto the boat, a "test well" was made into the boat hull by Byron Pfeifer of the UCLA Marina Aquatic Center, as shown in Figure 4-23(c)(d). The well is

a rectangular through hole on the ship hull with a tank on top to hold the water. A sensor holder was attached onto the sidewall of the well and the sensor plate is mounted onto the sensor holder. The bottom of the sensor holder was made flush with the bottom of the boat hull to ensure continuous boundary layer over the sensor. “Breathing holes” were made on the sensor holder at the rear end of the flow direction. Since the main rectangular hole will be sealed after the sensor plate is mounted, these “breathing holes” are to ensure there is no pressure difference across the sensor plate, which may push the floating plate vertically and affect the measurement. The real-time underwater camera (not shown on picture) was also used to observe the SHPo surface underwater in real time, similar as towing tank test.

Even though the sailing speed could be precisely measured using both GPS and speedometer, it is still difficult to define the flow conditions (e.g., Reynolds number) because of unknown size of wetted area. Firstly, as shown in the front view of a Boston Whaler (Figure 4-23(b) [44]), the hull shape evolved from the *Hickman Sea Sled* with two runners on the two sides. The double “V” shape under the boat is used to trap air and lift the boat out of water at high speed [45]. However, the lifting is affected by speed, wave, bow angle and other factors and changes with time. This indicates the wetted area of the boat bottom is changing. Second, with engine in the back, the boat tends to have a bow-up angle during sailing. This angle is also affected by the angle of the propeller, waves and sailing speeds. Because it is difficult to control flow conditions under the boat, it is necessary to test both SHPo surface and smooth surface in parallel at the same time to ensure fair comparison. The sensor is composed of two floating plates in parallel with similar spring constants, as shown in Figure 3-5(c). SHPo surface sample and smooth surface sample with the same size will be placed on two floating plates respectively. The displacement readings from the optical encoders for both plates were obtained at the same time, ensuring same flow conditions.

4.7.3 Results

4.7.3.1 Double Floating Plate Sensor Validation

Since the location of the two floating plates are slightly different, we first conducted an experiment with two same smooth surfaces mounted on two floating plates to confirm the same flow conditions at both locations. Figure 4-24 showed the tested results. As can be seen from the figure, we tested at three different speeds with one or two tests at each speed. The absolute shear force values were different for different tests even for the same speed reading, possibly due to different bow-up angle and currents in seawater. However, the relative difference between the two parallel floating plates remained very small for each test. This has verified that both floating plates are experiencing the same flow condition at the same time and the small difference in location doesn`t affect the result.

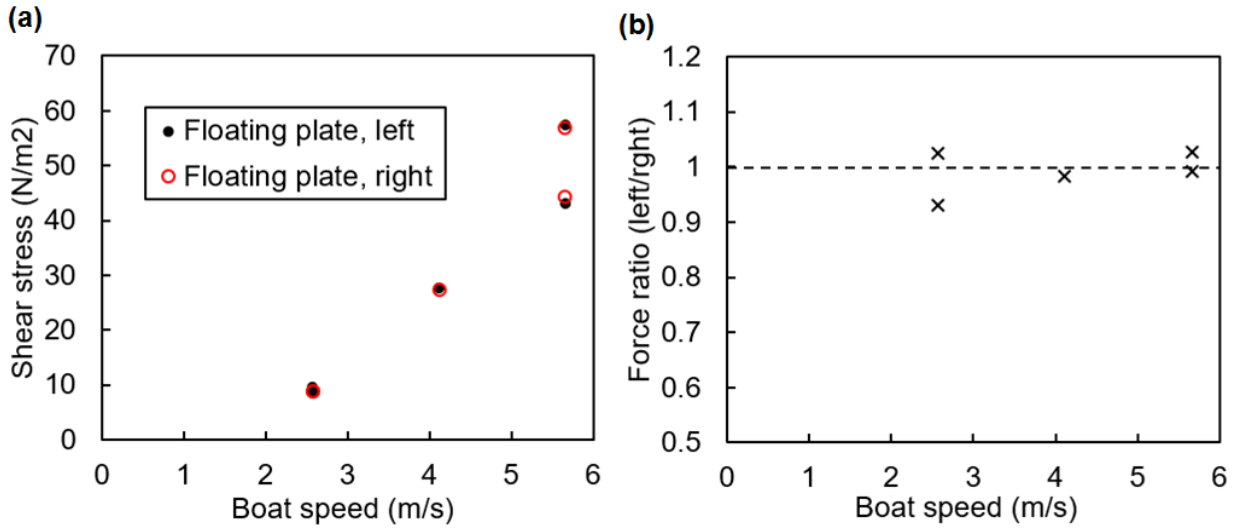

Figure 4-24 Testing with two same smooth surfaces in boat test. (a) Skin friction coefficient and (b) drag ratio of smooth surfaces at different speeds in field test.

4.7.3.2 SHPo Surface Drag Reduction Test

Silicon SHPo surface coated with Teflon AF 1600 was used in the drag reduction test. The SHPo surface has a pitch of 50 μm, gas fraction of 90% and grating height of 60 μm (SHPo#1 in Table 4-2). Figure 4-25 shows the pictures of SHPo surface throughout the test at speed of ~3 m/s. As can be seen from the figure, there were bubbles originated from the seawater and got trapped on the SHPo surface before test started (Figure 4-25(a)). During the test, due to shallow draught of the boat, bubbles created in the front of the boat flew passing the SHPo surface. Small bubbles were seen passing the SHPo surface at high speeds (Figure 4-25(b)) while large bubbles showed up as the boat started to decelerate (Figure 4-25(c)). Eventually after the boat stopped, the SHPo surface remained shiny without any bubble attached or wetting areas (Figure 4-25(d)).

As has been observed from the previous towing tank test, same SHPo surface began to show massive wetting after 4 m/s which corresponds to shear stress of ~23 N/m^2. However, during the boat test, no wetting was observed up to the highest speed tested (~ 5 m/s) with shear stress of ~ 50 N/m^2 for smooth surface. This is probably because the bubbles passing by the SHPo surface replenished the loss of gas, sustaining the plastron even at higher shear rate. Meanwhile, the increased drag at lowest speed might be caused by the form drag from initially trapped bubble (Figure 4-25(a)).

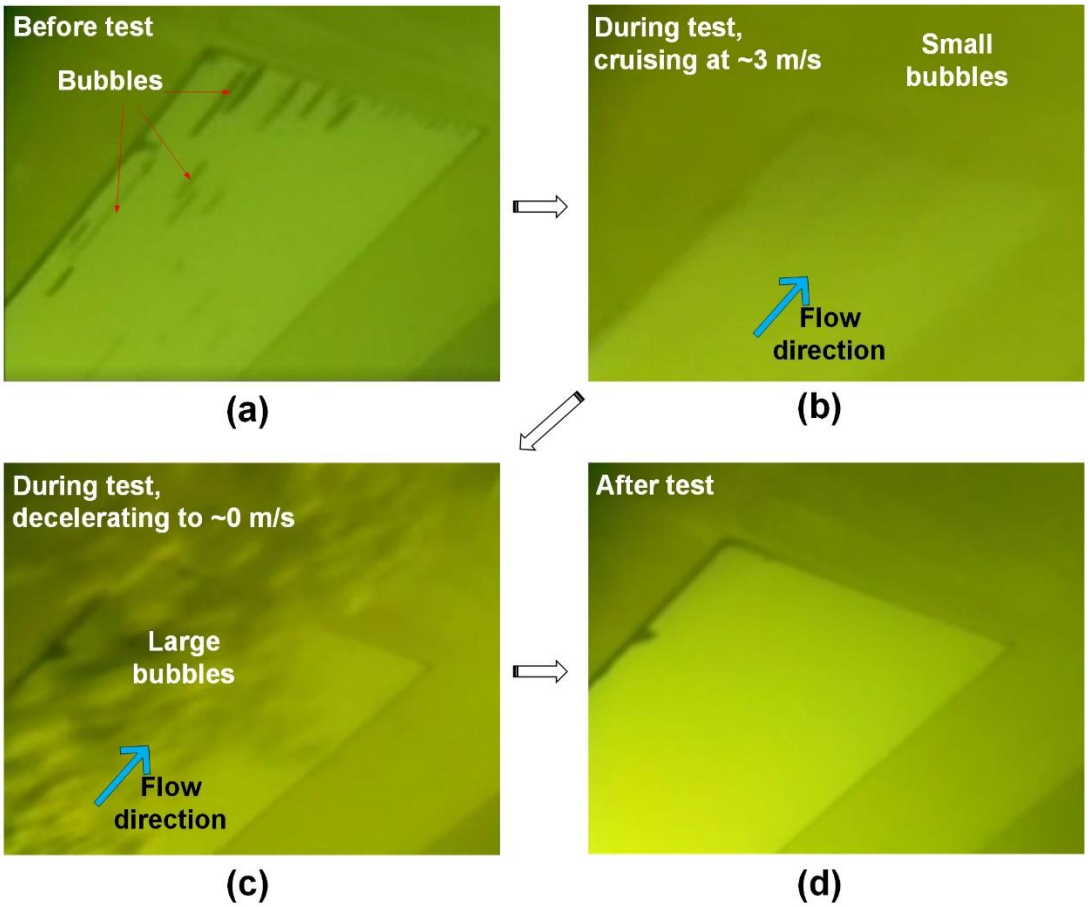

Figure 4-25 Pictures of tested SHPo surface in boat test (~3m/s).

Figure 4-26 shows the shear stress data from the sensor reading and drag ratio between SHPo surface and smooth surface for each test. At low speeds, the SHPo surface has more drag than the smooth surface, indicating the potential extra form drag created by the bubbles trapped on the surface. As the boat sped up, the bubbles were swept away, and the drag started to decrease. At the highest speed tested of ~ 5 m/s ($\mathrm{Re}_x \sim 7\times10^6$), the drag decreased by ~20% to ~80% of the smooth surface.

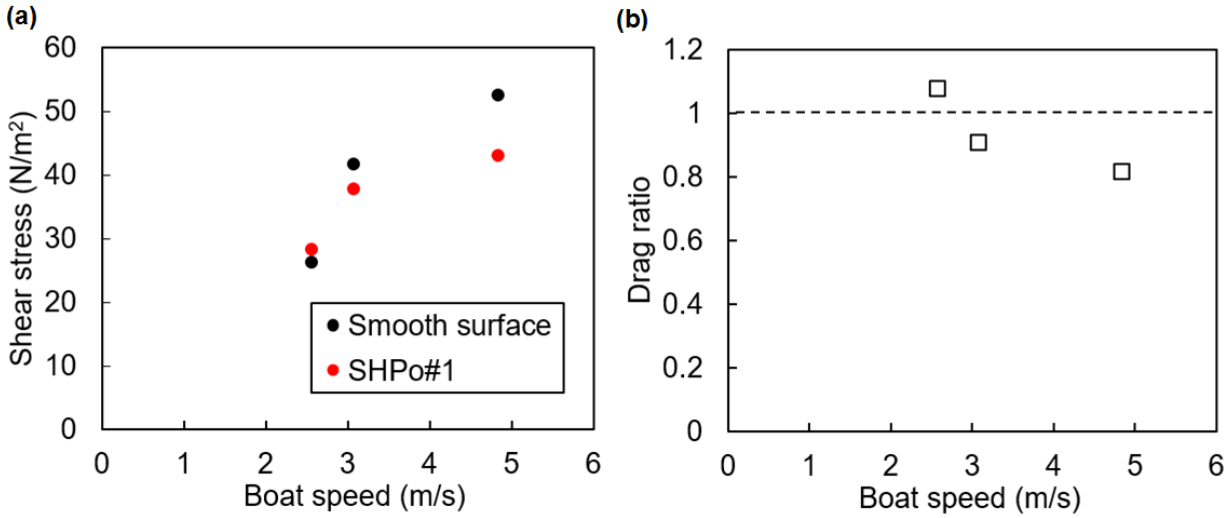

Figure 4-26 SHPo surface performance in boat test. (a) Skin friction coefficient and (b) drag ratio of SHPo surfaces at different speeds in field test.

4.7.4 Discussion

As a preliminary test, this experiment for the first time verified the drag reduction capability of the passive SHPo surface in high-speed boat tests. More importantly, the drag reduced more as Reynolds number increased. This trend is consistent with previous numerical studies [8, 9, 22] and our towing tank test (section 4.5). Due to the small size and speed limit of current boat, the Reynolds number (Re ~10^6-10^7) near the sensor is still much lower compared with other commercial marine vessels (Re ~10^8 - 10^9). However, according to Reynolds number effect, higher drag reduction is expected for larger marine vessels if SHPo surface stay dewetted.

Meanwhile, it needs to be pointed out that the bubbles in water and the shallow immersion depth of current boat helped the SHPo surface to stay dewetted throughout the test. The flowing bubbles created by the boat replenished the SHPo surface which would otherwise get wetted at such high shear rate, according to our recent towing tank test (section 4.5) and other experiment results [13].

However, with other large commercial marine vessels with higher immersion depth and more streamlined shape, we won`t expect the existence of similar bubbles flows. On the contrary, the high immersion depth and biofouling would accelerate the SHPo surface to wetting process [15, 16]. In those circumstances, active gas replenishing methods [41] to dewet the SHPo surface will be needed.

All in all, even though high drag reduction has been achieved for the first time in seawater field test, much work still need to be done to (1) sustain the gas on SHPo surface at large immersion depth and high Reynolds number (2) scale up the manufacturing of grating-structured SHPo surface for large area application.

4.8 Flow Tests Summary

Figure 4-27(a) summarized the drag ratios of all the SHPo surfaces tested above, together with all previous SHPo surface turbulent studies. Figure 4-27(b) summarized all our open water high-Reynolds number tests with only one previous study [13]. In summary:

(1) We obtained drag reduction up to 25% at high Reynolds number range ($\mathrm{Re} \sim 3.0\times10^{6} - 1.1\times10^{7}$) in open-water TBL flow for the first time.

(2) We observed drag reduction increasing with Reynolds number in large flow facilities for the first time, confirming previous numerical studies [8, 22] and rheometer experiment [32].

(3) Even though surface wetting prevents us from getting even higher drag reduction, we believe the semi-active gas replenishing mechanism [41] will eventually solve this problem, leading to much higher (Figure 4-22(a)) and sustainable drag reduction.

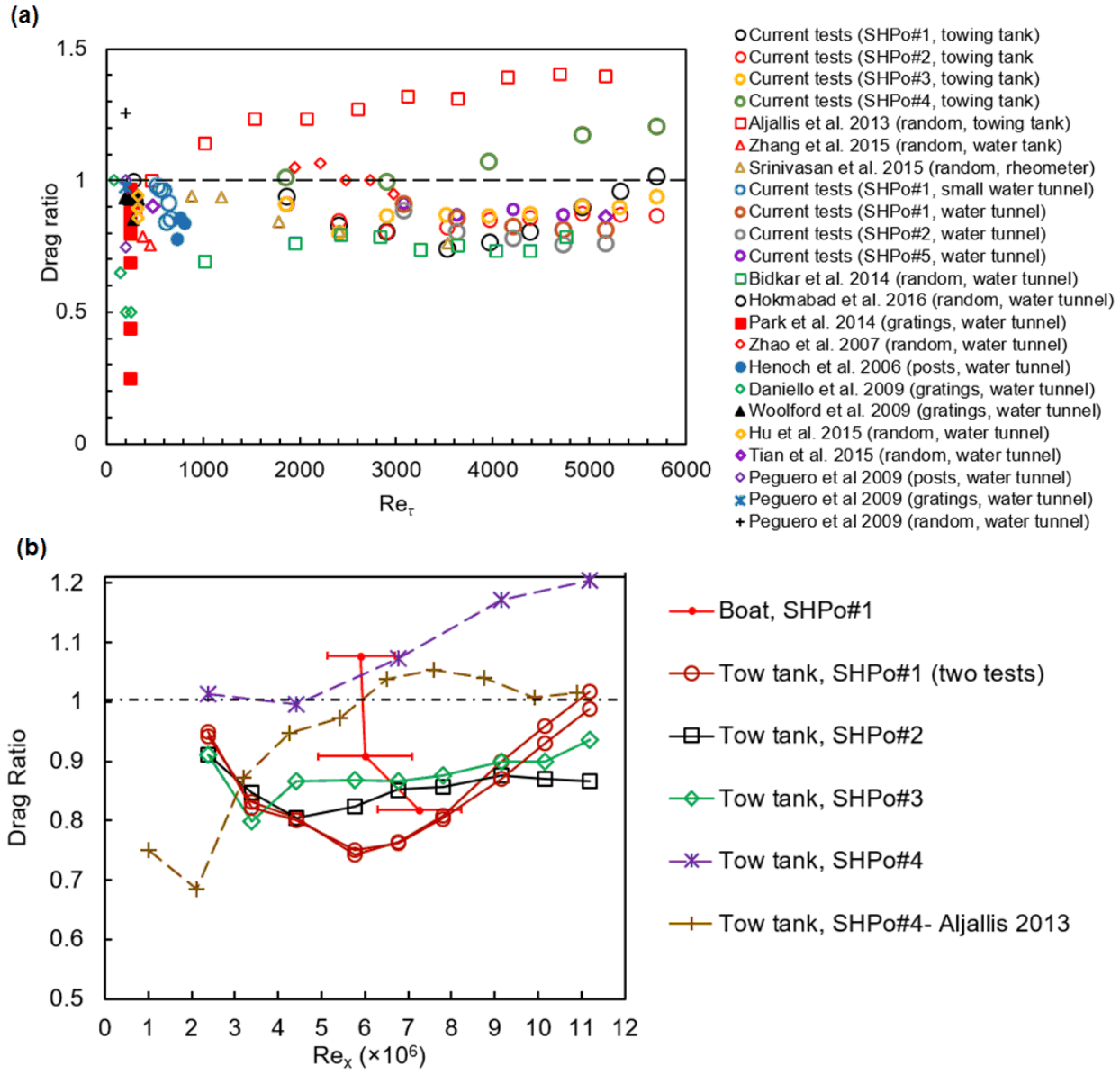

Figure 4-27 Summary of all SHPo surface flow tests in turbulent flow. (a) SHPo surface flow tests in turbulent flow (Figure 4-1) with our current tests (shown as empty circles in figure). (b) Open-water TBL flow test results [13] with our current open-water TBL flow tests.

4.9 References

[1] C. Lee, C.-H. Choi, and C.-J. Kim, "Superhydrophobic drag reduction in laminar flows: a critical review," *Experiments in Fluids,* vol. 57, 176, 2016.

[2] C. Lee, C.-H. Choi, and C.-J. Kim, "Structured surfaces for a giant liquid slip," *Physical Review Letters,* vol. 101, 64501, 2008.

[3] C. Lee and C.-J. Kim, "Maximizing the giant liquid slip on superhydrophobic microstructures by nanostructuring their sidewalls," *Langmuir,* vol. 25, pp. 12812-12818, 2009.

[4] C.-H. Choi and C.-J. Kim, "Large slip of aqueous liquid flow over a nanoengineered superhydrophobic surface," *Physical Review Letters,* vol. 96, 066001, 2006.

[5] Y. C. Jung and B. Bhushan, "Biomimetic structures for fluid drag reduction in laminar and turbulent flows," *Journal of Physics-Condensed Matter,* vol. 22, 2010.

[6] H. Park, G. Sun, and C.-J. Kim, "Superhydrophobic turbulent drag reduction as a function of surface grating parameters," *Journal of Fluid Mechanics,* vol. 747, pp. 722-734, 2014.

[7] K. B. Golovin, J. W. Gose, M. Perlin, S. L. Ceccio, and A. Tuteja, "Bioinspired surfaces for turbulent drag reduction," *Phil. Trans. R. Soc. A,* vol. 374, 20160189, 2016.

[8] T. G. Min and J. Kim, "Effects of hydrophobic surface on skin-friction drag," *Physics of Fluids,* vol. 16, pp. L55-L58, 2004.

[9] J. Lee, T. O. Jelly, and T. A. Zaki, "Effect of Reynolds Number on Turbulent Drag Reduction by Superhydrophobic Surface Textures," *Flow, Turbulence and Combustion,* vol. 95, pp. 277-300, 2015.

[10] C. G. Jiang, S. C. Xin, and C. W. Wu, "Drag reduction of a miniature boat with superhydrophobic grille bottom," *Aip Advances,* vol. 1, 2011.

[11] H. Y. Dong, M. J. Cheng, Y. J. Zhang, H. Wei, and F. Shi, "Extraordinary drag-reducing effect of a superhydrophobic coating on a macroscopic model ship at high speed," *Journal of Materials Chemistry A,* vol. 1, pp. 5886-5891, 2013.

[12] S. S. Zhang, X. Ouyang, J. Li, S. Gao, S. H. Han, L. H. Liu, *et al.*, "Underwater Drag-Reducing Effect of Superhydrophobic Submarine Model," *Langmuir,* vol. 31, pp. 587-593, 2015.

[13] E. Aljallis, M. A. Sarshar, R. Datla, V. Sikka, A. Jones, and C. H. Choi, "Experimental study of skin friction drag reduction on superhydrophobic flat plates in high Reynolds number boundary layer flow," *Physics of Fluids,* vol. 25, 2013.

[14] J. Monty, N. Hutchins, H. Ng, I. Marusic, and M. Chong, "A comparison of turbulent pipe, channel and boundary layer flows," *Journal of Fluid Mechanics,* vol. 632, pp. 431-442, 2009.

[15] M. Xu, G. Sun, and C.-J. Kim, "Infinite Lifetime of Underwater Superhydrophobic States," *Physical Review Letters,* vol. 113, 136103, 2014.

[16] R. Poetes, K. Holtzmann, K. Franze, and U. Steiner, "Metastable Underwater Superhydrophobicity," *Physical Review Letters,* vol. 105, 166104, 2010.

[17] H. Schlichting, K. Gersten, and K. Gersten, *Boundary-layer theory*: Springer Science & Business Media, 2000.

[18] D. G. Crowdy, "Analytical formulae for longitudinal slip lengths over unidirectional superhydrophobic surfaces with curved menisci," *Journal of Fluid Mechanics,* vol. 791, 2016.

[19] J. Seo, R. García-Mayoral, and A. Mani, "Pressure fluctuations and interfacial robustness in turbulent flows over superhydrophobic surfaces," *Journal of Fluid Mechanics,* vol. 783, pp. 448-473, 2015.

[20] K. Jeffs, D. Maynes, and B. W. Webb, "Prediction of turbulent channel flow with superhydrophobic walls consisting of micro-ribs and cavities oriented parallel to the flow direction," *International Journal of Heat and Mass Transfer,* vol. 53, pp. 786-796, 2010.

[21] H. Park, "A numerical study of the effects of superhydrophobic surfaces on skin-friction drag reduction in wall-bounded shear flows," Ph.D. dissertation, Mechanical Engineering, University of California, Los Angeles, 2015.

[22] H. Park, H. Park, and J. Kim, "A numerical study of the effects of superhydrophobic surface on skin-friction drag in turbulent channel flow," *Physics of Fluids,* vol. 25, 110815, 2013.

[23] M. B. Martell, J. B. Perot, and J. P. Rothstein, "Direct numerical simulations of turbulent flows over superhydrophobic surfaces," *Journal of Fluid Mechanics,* vol. 620, pp. 31-41, 2009.

[24] M. B. Martell, J. P. Rothstein, and J. B. Perot, "An analysis of superhydrophobic turbulent drag reduction mechanisms using direct numerical simulation," *Physics of Fluids,* vol. 22, 065102, 2010.

[25] C. Henoch, T. Krupenkin, P. Kolodner, J. Taylor, M. Hodes, A. Lyons, *et al.*, "Turbulent drag reduction using superhydrophobic surfaces," in *3rd AIAA Flow Control Conference*, 2006, pp. 5-8.

[26] R. J. Daniello, N. E. Waterhouse, and J. P. Rothstein, "Drag reduction in turbulent flows over superhydrophobic surfaces," *Physics of Fluids,* vol. 21, 085103, 2009.

[27] C. Peguero and K. Breuer, "On drag reduction in turbulent channel flow over superhydrophobic surfaces," in *Advances in Turbulence XII*, ed: Springer, 2009, pp. 233-236.

[28] B. Woolford, J. Prince, D. Maynes, and B. W. Webb, "Particle image velocimetry characterization of turbulent channel flow with rib patterned superhydrophobic walls," *Physics of Fluids,* vol. 21, 085106, 2009.

[29] J.-p. Zhao, X.-d. Du, and X.-h. Shi, "Experimental research on friction-reduction with super-hydrophobic surfaces," *Journal of Marine Science and Application,* vol. 6, pp. 58-61, 2007.

[30] R. A. Bidkar, L. Leblanc, A. J. Kulkarni, V. Bahadur, S. L. Ceccio, and M. Perlin, "Skin-friction drag reduction in the turbulent regime using random-textured hydrophobic surfaces," *Physics of Fluids,* vol. 26, pp. -, 2014.

[31] H. Haibao, D. Peng, Z. Feng, S. Dong, and W. Yang, "Effect of hydrophobicity on turbulent boundary layer under water," *Experimental Thermal and Fluid Science,* vol. 60, pp. 148-156, 2015.

[32] S. Srinivasan, J. A. Kleingartner, J. B. Gilbert, R. E. Cohen, A. J. Milne, and G. H. McKinley, "Sustainable Drag Reduction in Turbulent Taylor-Couette Flows by Depositing Sprayable Superhydrophobic Surfaces," *Physical Review Letters,* vol. 114, 014501, 2015.

[33] H. Tian, J. Zhang, E. Wang, Z. Yao, and N. Jiang, "Experimental investigation on drag reduction in turbulent boundary layer over superhydrophobic surface by TRPIV," *Theoretical and Applied Mechanics Letters,* vol. 5, pp. 45-49, 2015.

[34] J. Zhang, H. Tian, Z. Yao, P. Hao, and N. Jiang, "Mechanisms of drag reduction of superhydrophobic surfaces in a turbulent boundary layer flow," *Experiments in Fluids,* vol. 56, pp. 1-13, 2015.

[35] B. V. Hokmabad and S. Ghaemi, "Turbulent flow over wetted and non-wetted superhydrophobic counterparts with random structure," *Physics of Fluids,* vol. 28, 015112, 2016.

[36] K. Fukagata, N. Kasagi, and P. Koumoutsakos, "A theoretical prediction of friction drag reduction in turbulent flow by superhydrophobic surfaces," *Physics of Fluids,* vol. 18, 051703, 2006.

[37] A. Busse and N. D. Sandham, "Influence of an anisotropic slip-length boundary condition on turbulent channel flow," *Physics of Fluids,* vol. 24, 2012.

[38] D. Saranadhi, D. Chen, J. A. Kleingartner, S. Srinivasan, R. E. Cohen, and G. H. McKinley, "Sustained drag reduction in a turbulent flow using a low-temperature Leidenfrost surface," *Science Advances,* vol. 2, 2016.

[39] S. H. Lee and H. J. Sung, "Direct numerical simulation of the turbulent boundary layer over a rod-roughened wall," *Journal of Fluid Mechanics,* vol. 584, pp. 125-146, 2007.

[40] R. García-Mayoral and J. Jiménez, "Drag reduction by riblets," *Philosophical Transactions of the Royal Society of London A: Mathematical, Physical and Engineering Sciences,* vol. 369, pp. 1412-1427, 2011.

[41] C. Lee and C.-J. Kim, "Underwater Restoration and Retention of Gases on Superhydrophobic Surfaces for Drag Reduction," *Physical Review Letters,* vol. 106, 14502, 2011.

[42] E. Karatay, A. S. Haase, C. W. Visser, C. Sun, D. Lohse, P. A. Tsai, *et al.*, "Control of slippage with tunable bubble mattresses," *Proceedings of the National Academy of Sciences of the United States of America,* vol. 110, pp. 8422-8426, 2013.

[43] S. A. Mäkiharju, M. Perlin, and S. L. Ceccio, "On the energy economics of air lubrication drag reduction," *International Journal of Naval Architecture and Ocean Engineering,* vol. 4, pp. 412-422, 2012.

[44] J. Hebert. (2000). *Original Design and Conception of the 13-foot Whaler Hull*. Available: http://continuouswave.com/whaler/reference/13/originalHullDesign.html

[45] G. Dave, "The Hickman Sea Sled: The Best High Speed Hull Ever?," *Boatbuilder Magazine,* 1998.

Chapter 5 Whole-Teflon Superhydrophobic Surfaces for Sustainable Drag Reduction

5.1 Introduction

5.1.1 Teflon as the Material for Functional Microstructures

Polytetrafluoroethylene (PTFE)-based formulas – best known as brand name Teflon by DuPont – is well known for its great hydrophobicity, superior inertness to almost all chemicals, and non-stick properties. They also show excellent resistance to molecular adsorption from and material leaching to surrounding solutions [1]. These unique properties are crucial for many functional microstructures, such as superhydrophobic (SHPo) surfaces and microfluidic chips. Especially for the key applications of SHPo surfaces (e.g., drag reduction, anti-biofouling), the surface material should remain hydrophobic over the entire service period under water. For many microfluidic chips, the surface should be inert to different solvents, do not adsorb or absorb molecules, and do not leach its molecules to the surrounding solutions [1].

In order to meet the above requirements, for many years coatable PTFE-based formulas (e.g., Teflon AF of DuPont, Cytop of Asahi Glass, and FluoroPel of Cytonix) have been widely used for both SHPo surfaces [2-5] and microfluidic chips [6-9]. However, the inherently low energy of Teflon makes the coated film prone to defects and susceptible to peeling, restricting the reliability and lifetime of the functional microstructures. Also, the high-temperature (e.g., 330°C) required for baking after coating is not compatible with many structural materials, especially polymers. As the underlying structural materials are mostly made of silicon or glass, microfabrication of the surface structures (typically lithographic etching) is too expensive for commercialization. In recent

years, microstructures made entirely of Teflon [1, 10, 11] have shown promising performances. These whole-Teflon microstructures not only possess all the key properties of Teflon but also showed good long-term performance, since the whole structure is intrinsically hydrophobic. Moreover, the hot-embossing method employed to form the whole-Teflon microstructure greatly reduced the fabrication cost and time.

5.1.2 SHPo Surfaces with Self-Regulated Gas Restoration Mechanism

SHPo surfaces have shown promise to traverse in water with an appreciably smaller (i.e., by >10%) friction than the existing surfaces [4, 12-14]. This reduction of drag is caused by the lubrication effect of the air trapped in their hydrophobic microstructures under water. However, unlike the SHPo surface supporting water droplets in air environment, SHPo surface fully immersed under water cannot keep the air for long [15], undermining the fundamental premise of SHPo drag reduction. The short lifetime (typically < 1 hr) of the trapped air under water is currently the main challenge against the use of SHPo materials for underwater applications [15, 16]. A recent breakthrough solved this problem by engineering a self-regulated (i.e., self-initiated, self-limited, and externally powered) gas-restoration mechanism using electrolysis, which made the trapped air sustainable under water indefinitely by supplying a minimal amount of electric power [3, 16]. Electrolysis was preferred over boiling or pneumatic means for its low power consumption, easy actuation control, efficiency at small scales, and most importantly the possibility of self-regulation. When water impregnated any microstructures occasionally under water, the surface “healed” and recovered the lost gas, as illustrated in Figure 5-1. Power was consumed only when and where the surface was wetted. This surface has shown strong robustness against defects and high hydrostatic pressure (measured up to 70 m depth) [17], which mimicked marine conditions.

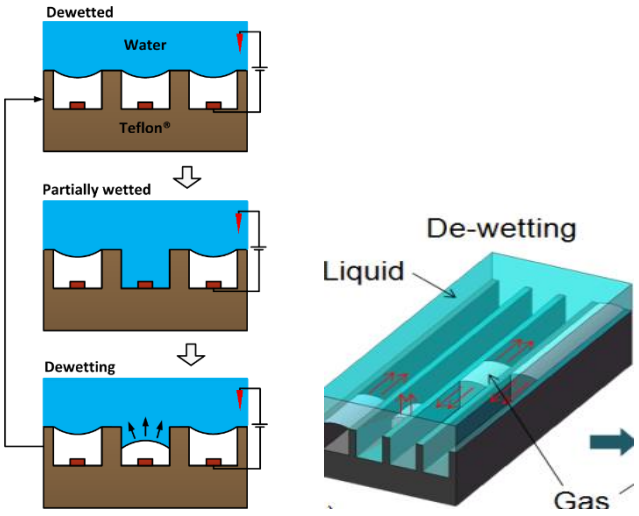

Figure 5-1 Self-regulating gas restoration mechanism. Voltage is always applied between water and the electrodes on the microstructure bottom. (Top) Full Cassie state. The electrochemical circuit is open, consuming no power. (Middle) Water impregnates a portion of microstructures and contacts the electrode, closing the circuit locally. (Bottom) A gas is generated by electrolysis, restoring Cassie state and re-opening the circuit. (Right) The key is how to make the generated gas grow within the structures rather than forming bubbles and leaving

This semi-active mechanism consumed little power (e.g. battery-powered) due to the self-activating and self-limiting nature of its gas generation. The key for the success was forcing the generated gas to spread within the microstructures rather than leaving as bubbles, even though the former scenario was energetically less favorable in general [3]. After impregnation, the seed gas between the structures should spread only laterally when pressurized by an influx of additional gases. If allowed to grow vertically off the structures, additional gas would escape the surface rather than covering more of the surface. To achieve the feat, the bubble expansion should encounter less resistance in the lateral direction along surface structures than in the vertical direction off the surface once the liquid-gas interfaces reach the top of the structures. This

challenging goal was obtained by having the surface structures satisfy certain criteria for the given surface pattern (e.g., ridges, posts) of the microstructures [3].

5.1.3 Motivation

Several studies on SHPo surface drag reduction has demonstrated significant drag reduction in turbulent flows in laboratory conditions [4, 12-14]. However, the fundamental problem against its applications remains to be the short-lived air on the SHPo surfaces fully submerged under water [16], as well as scale-up fabrication of such surfaces [18]. The self-regulated gas restoration mechanism described above uses a minimal amount of external electrical power [3, 19] and has so far been the only verified solution that makes the trapped air sustainable under water. However, the surface developed in previous work [3] used semiconductor process and silicon as material which are too expensive for mass manufacturing. Also, the Teflon AF coating applied on the photoresist and silicon surface are easy to be peeled off after electrolysis.

Inspired by the whole-Teflon microstructures and the self-regulating gas restoration mechanism, in this chapter we further develop (1) a one-step hot embossing process to fabricate a whole-Teflon SHPo surfaces with embedded electrodes for self-regulated gas recovery for mass manufacturing and (2) a self-powered gas restoration mechanism that not only has all the advantages as previous work but also doesn`t need any external power supply for gas restoration. Semi-active SHPo surfaces with the self-powered gas restoration mechanism can be applied onto the ship hull without the need of external electrical connection. This self-powered SHPo surface is expected to not only produce significant (i.e., > 10%) drag reduction found in several laboratory studies [4, 12-14] but also sustain the drag reduction in practical conditions by sustaining the gas layer under water without external power supply. Moreover, the materials chosen and fabrication approach employed

to make these semi-active SHPo surfaces make the proposed manufacturing approach scalable for ultimate mass production in the future.

5.2 Microstructure Design

5.2.1 Geometry Design

As has been discussed in Chapter 4, grating structures are a desired structure for SHPo turbulent drag reduction. Compared with other geometric design (e.g., posts, random microstructures), SHPo surfaces made of micro-grating structures have shown the highest and most consistent drag reduction in turbulent flows [4, 18, 20]. The geometric design of micro gratings is discussed in the following to optimize drag reduction, air-water meniscus stability and gas replenishing process.

5.2.1.1 Maximize Drag Reduction

The drag reducing capability of SHPo surface is mainly affected by pitch and gas fraction at the top of the grating. Studies have shown that the drag reducing capability will be greatly compromised once the air-water meniscus depins from the grating top [21]. The effect of pitch and gas fraction of micro-grating on the drag reduction capability has been well-studied in laminar flow both analytically [22] and experimentally [23]: the slip length b increase linearly with grating pitch and exponentially with gas fraction. However, in turbulent flow, no analytical theory has been established. Even though the numerical [24, 25] and experimental studies[4, 20] have not match with each other yet, they all demonstrated similar trend that the drag reduction increases as the pitch and gas fraction increase. Also, as shown in Figure 5-2 [4], when the gas fraction is approaching 100% (i.e., complete gas layer), the drag reduction is more sensitive to gas fraction changes compared with pitch changes, and increase dramatically as the gas fraction increases [4, 24]. This trend is quite similar to the trend in laminar flow.

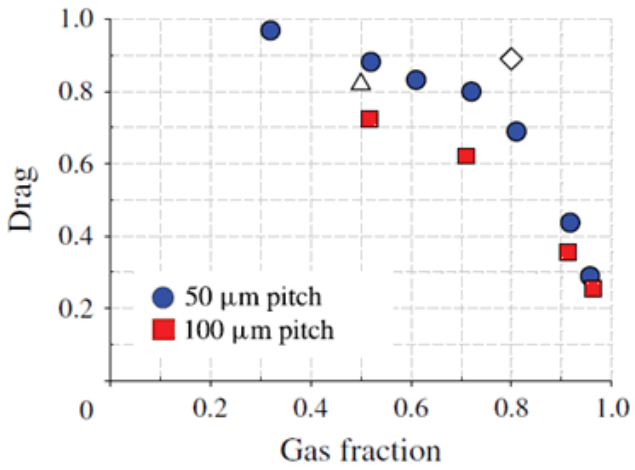

Figure 5-2 Effect of grating geometry of SHPo surface on drag ratio in TBL flow. [4]

Grating height will also affect the drag reduction capability. If the gratings are too low, the curved or fluctuating air-water will touch the grating bottom, leading Cassie to Wenzel transition known as sag impalement [26]. Beside this, the grating height can still affect the drag reduction in two other ways: drag between trapped gas and wall, and meniscus shape. Since the gas in between gratings is trapped underwater, the shear stress on air-water interface drives the gas to flow and circulate inside the cavity, as shown in Figure 5-3(a). This circulation will cause shear stress between gas and the solid wall, increasing drag on SHPo surface [27]. The thicker the gas layer (i.e., larger grating height), the smaller this gas circulation effect is [27].

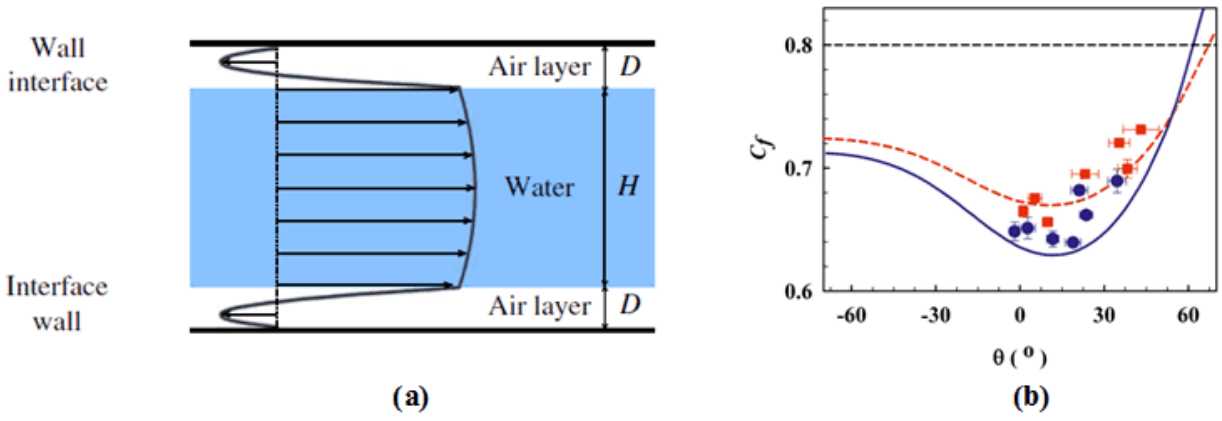

Figure 5-3 Effect of grating height on SHPo surface drag reduction. (a) Circulating gas flow in SHPo surface gas layer [27] (b) Effect of meniscus curvature on skin friction coefficient [28].

The grating height will also affect meniscus shape, which will affect drag reduction (Figure 5-3(b)). As found in recent numerical [29] and experimental studies, the drag reduction will decrease as the meniscus bends into the gratings. For example, Crowdy [28] showed that for grating SHPo surface with 90% gas fraction, when the angle of the meniscus curved from flat to -30^o into the gratings, the slip length decreased by approximately 14%. Once the SHPo surface is immersed, the meniscus will bend toward the solid surface due to hydrostatic pressure. Meanwhile, since all the gas is trapped, pressure will build up inside the cavity and resist further meniscus bending. The smaller volume of the gas, the smaller meniscus bending once immersed [15], as shown in Equation (3-3). Moreover, the pressure usually fluctuates in turbulent flow, smaller grating height will lead to smaller meniscus fluctuation, which could cause higher drag reduction. However, as discussed in [15], diffusion of gas will eventually lead to an equilibrium state or depinning of meniscus, independent of grating height. An optimal grating height for drag reduction is beyond the scope of this dissertation.

5.2.1.2 Increase Meniscus Stability

The pitch and gas fraction of the micro-gratings determine the drag reduction capability and the air-water meniscus stability. The meniscus stability is determined by the following equation:

$$\Delta P = \frac{2\sigma \cos\theta_a}{L\Phi} \tag{6-1}$$

Where ΔP is the maximum pressure difference across the meniscus that the micro-gratings can sustain, σ is the surface tension of water, θ_a is the advancing contact angle of the meniscus on

the grating top, L is the pitch and Φ is the gas fraction. For pitch and gas fraction, there is a tradeoff between drag reduction and meniscus stability: we want to increase them for large drag reduction but decrease them for stable meniscus. However, because the drag reduction is more sensitive to gas fraction when gas fraction is high while the meniscus stability is equally sensitive to both. Large gas fraction with small pitch is a better option.

The above equation only considered 2D scenario while the actual sample is 3D. The grating geometry at the ends of the sample also needs to be considered. Since the turbulent boundary layer is expect to have dramatic change at the starting and ending area of the micro-gratings, it has been found that the areas near the ends of the micro-gratings are prone to wet first. As illustrated in Figure 5-4, three different end structures have been considered for grating SHPo surfaces: closed end, open end and semi open end. Closed-end structure has the best performance in term of meniscus stability due to the extra edge that the meniscus could pin to. However, the whole-Teflon SHPo surface was fabricated using high-temperature molding process and the surface will experience shrinkage after cooled down. We found that the closed end gratings were likely to be distorted at the corner during demolding process. Meanwhile, while the open-end grating can stay intact after demolding, they are easier to get wetted. Thus, we designed a semi-open structure with additional short gratings in between long gratings. The added gratings will make the air-water meniscus more robust and could also stay intact after demolding.

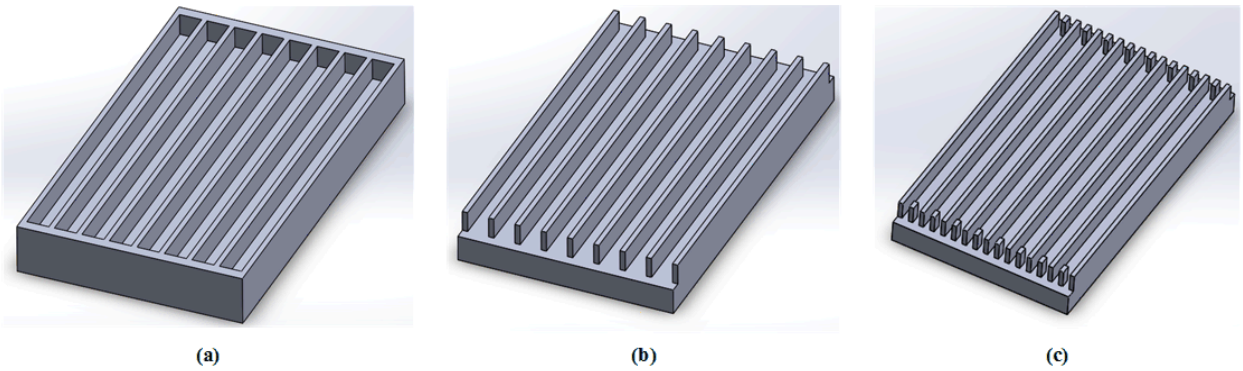

Figure 5-4 SHPo surface with different grating ends. (a) Closed end. (b) Open end. (c) Semi-open end.

It has also been found that making the top surface hydrophilic will help the gas retention inside the SHPo surface [30]. However, we didn`t apply hydrophilic top to whole-Teflon SHPo surface due to the difficulties in integrating the process into current mass manufacturing process.

5.2.1.3 Facilitate Gas Replenishing

The gas restoring mechanism used in [3] was applied to whole-Teflon SHPo surface. Based on [3], the micro-gratings should be designed that the generated gas at the bottom is more favorable to propagate along the grating laterally rather than out of the top of the grating vertically. The process is described in the equation [3]:

$$H / L > \frac{-(1+\cos\theta_{b,rec})\Phi}{2\cos\theta_{g,rec} - 2\sin\theta_{t,rec}} \tag{6-2}$$

where L is the pitch, H is the grating height, Φ is gas fraction, $\theta_{b,rec}$ is the receding contact angle on the bottom surface, $\theta_{g,rec}$ is the receding contact angle on the sidewall surface and $\theta_{t,rec}$ is the receding contact angle on the top surface of the grating.

As shown in Equation (6-2), to facilitate gas propagation, we prefer to reduce right-hand side while increase left-hand side. Firstly, smaller pitch and gas fraction are preferred. Secondly, taller grating is more favorable for gas propagation. However, as shown in previous study [15], taller grating increases the time of wetting process when meniscus sliding down. During the wetting process, little drag reduction exists [21]. For high drag reduction capability, we prefer the meniscus to slide down fast once it depins so the gas restoration process could be triggered. Therefore, low gratings are preferred as long as (1) there is no sag impalement (2) gas still prefer to propagate along the gratings (3) there is not much gas-circulation-induced shear force.

The surface properties play a big role in affecting receding contact angles in Equation (6-2). To minimize the right-hand part, the receding contact angle on the top surface of the grating needs to be as small as possible and ideally equal or less than 90°. The receding angle on the sidewall and the bottom surface needs to be as high as possible, ideally 180°. However, due to fabrication constraints, we only increased the bottom surface receding contact angle using "nanograss" made of Teflon, as shown in Figure 5-5. The structures are the reverse replica of nanoholes on the mold top surface.

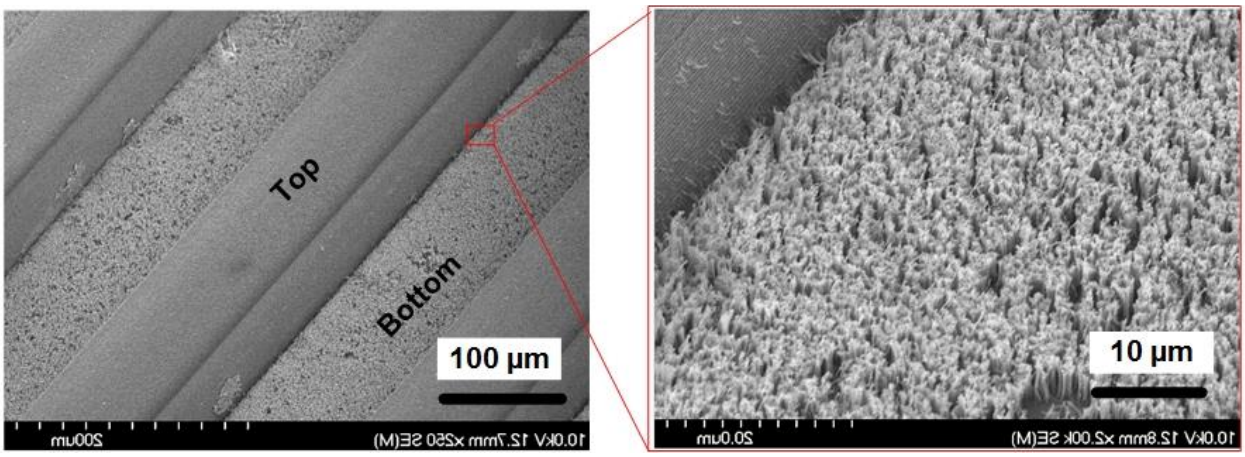

Figure 5-5 "Nanograss" structure at the bottom of the SHPo surface micro-gratings.

5.2.2 Self-powered Gas Restoration

While the self-regulating gas restoration mechanism in [3] could restore the drag reduction capability of SHPo surface even after it get wetted, it relies on outside power source for electrolysis. This will introduce the problems of wire connection and sealing especially for large area applications. To solve this problem, a self-powered gas generation mechanism was developed so no external power source is required for gas restoration. The structure of self-powered SHPo surface is shown in Figure 5-6, metal 1 and metal 2 are electrically connected to each other and chosen to have distinctively different electrode potentials. When a portion of the micro-trenches is filled with electrolyte (e.g., seawater), which connects metal 1 and metal 2, an electrochemical (galvanic) reaction ensues, and the reduction reaction on metal 1 generates a gas (e.g., hydrogen) within the microfeatures. If the micro-trenches are of a proper geometry, as discussed in [3], the generated gas will fill the micro-trenches rather than forming individual bubbles and leave the surface. The gas generation self-regulates itself and effectively maintains the gas inside the micro-trenches against any wetting events. Moreover, no external power supply is needed to generate the gas. The chemical reactions on different electrodes in typical seawater are:

$$\begin{aligned} &Cathode: 2H^+ + 2e^- \Rightarrow H_2 \uparrow \\ &Anode: M - e^- \Rightarrow M^+ \end{aligned} \tag{6-3}$$

where M is the metal 2.

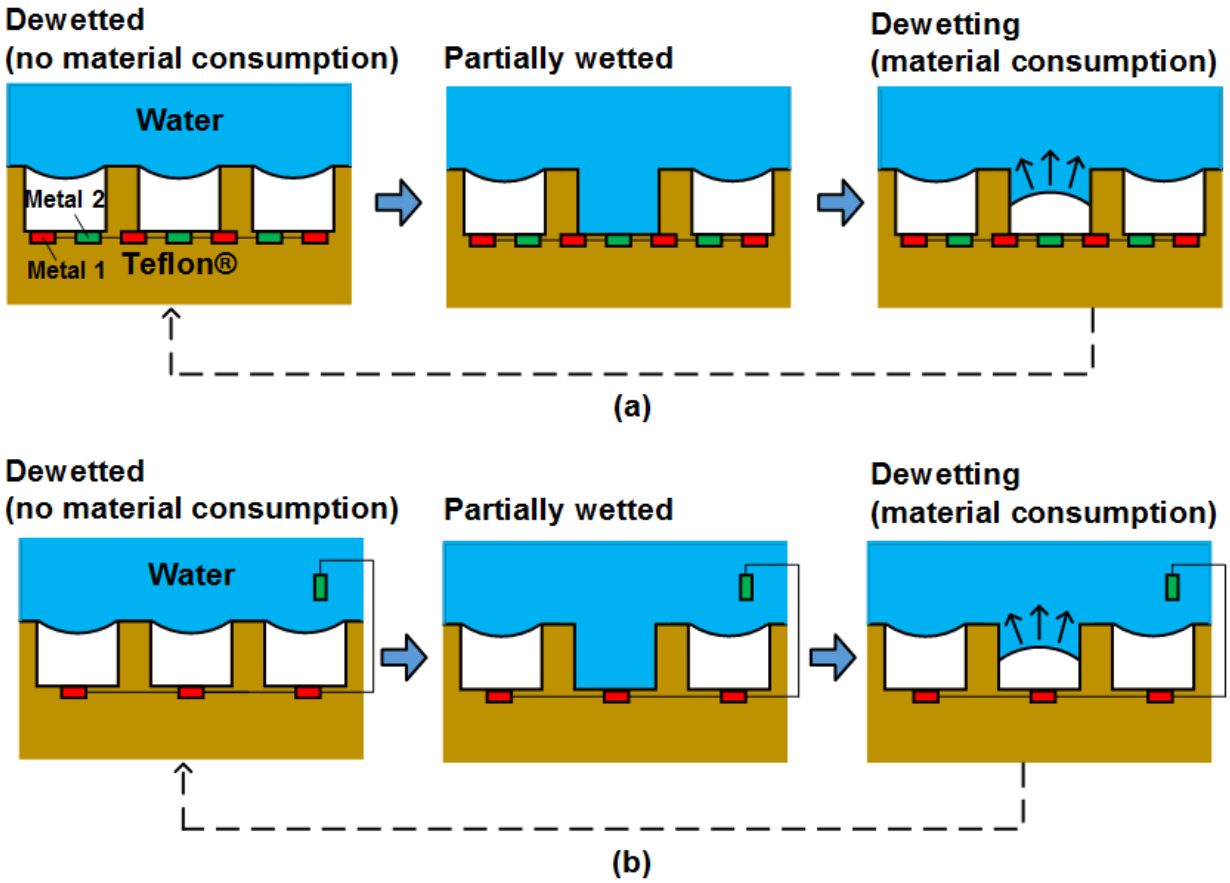

Figure 5-6 Gas replenishing mechanisms of self-powered SHPo surface. (a) Both electrodes are underneath the micro-gratings. (b) Cathode is underneath the micro-gratings while anode is immersed in water.

Electrode material selection is a crucial part of this gas generation mechanism. Both of the electrodes should (1) meet the electrode potential requirements, (2) be compatible with the molding process, (3) be economical. For electrode potential, the cathode material should have higher potential than hydrogen ion in water so it is not involved in the reaction. Also, the cathode material should have low hydrogen evolution potential so hydrogen is easy to be generated on it. Meanwhile, the electrode potential of anode material should be lower than that of hydrogen ion in water so it will be involved in the reaction. The gas generation speed is affected by the material

selection, reaction area and environment parameters (e.g., temperature). The reaction speed shouldn't be too high that the reaction is too violent to stop. It also shouldn`t be too slow that the gas generation is slower than gas depletion. We eventually used magnesium as anode material with nickel or copper as cathode material.

5.3 Mass Manufacturing Process Development

Due to the high glass transition temperature of Teflon FEP, hot embossing is the optimal method to fabricate whole-Teflon microstructures. It also has the potential for mass manufacturing of larger area sample due to its relatively straightforward process. Hot embossing of thermoplastic materials to fabricate microstructures has been studied extensively in recent years [31-39]. However, hot embossing with Teflon for microstructures was reported only recently, using Teflon PFA or FEP [1, 11, 34].

5.3.1 Mold Fabrication

Teflon FEP and PFA has been applied to the fabrication of microfluidics structures [1]. However, in previous studies, the mold was fabricated using PDMS with tuned composition to withstand high temperature. The mold itself might change shape during cooling and cause bad fidelity, which is critical for us since our SHPo surface gratings has smaller (~5 μm) feature size. Moreover, the mold itself might get abraded after many times of repeated mold and demolding cycles. Considering all the factors, we decided to use silicon to fabricate the mold. The mature MEMS fabrication process will precisely define the mold feature size. Also, the silicon material is hard and difficult to be abraded even after multiple cycles of molding and demolding practices.

The fabrication process, shown in Figure 5-7(a)-(f), started with a single-side polished silicon wafer that is 500 μm thick. First, the surface was patterned using DRIE to obtain the micro-

trenches that is about 55 μm deep. Then the wafer was cleaned in oxygen plasma to remove the fluoropolymers deposited during the DRIE process. The oxide mask was then removed using buffered oxide etch (BOE) containing hydrofluoric acid and buffer solutions. After thorough cleaning using Piranha solution (98 wt.% H_2SO_4:30 wt.% H_2O_2 = 4:1), the wafer was etched again in RIE to widen the top part of the micro-trenches and reduce the scalloping structures on the sidewall. The wafer was cleaned in oxygen plasma after that. The nanoholes on the mold were fabricated using silver-nanoparticle-assisted silicon etching [40]. To fabricate nanoholes on the mold, the wafer was first cleaned using Piranha solution for 10 mins and BOE solution for 5 mins respectively. After drying, the sample was immersed into Ag deposition solution (3.71 mol/L HF and 0.004 mol/L $AgNO_3$) for 1 mins to grow silver nanoparticles. After cleaning using DI water, the sample was transferred to Ag etching solution (H_3PO_4:HNO_3:CH_3COOH:H_2O = 3:3:23:1) for 10 mins in to reduce the Ag nanoparticle size. After cleaning, the wafer was dipped into silicon etching solution (6.57 mol/L HF and 0.18 mol/L H_2O_2) for 1 minute to achieve nanoholes on silicon wafer. Eventually, the residual silver was etched away using nitric acid solution.

The RIE etching process was proven to be a critical process for successful demolding of the SHPo surface. Firstly, the DRIE etched sidewall will have negative angles [41] (i.e., reentrant) so the micro-grating structure is “locked” inside, making demolding very difficult. The RIE process will etch the top part of the trench faster than the bottom part, resulting a positive tapered angle (Figure 5-7(g)), which will facilitate demolding. Second, the “scalloping” structure on the sidewall of the DRIE will increase the friction on the sidewall during demolding. The RIE process will etch the nanostructure, smoothing the sidewall.

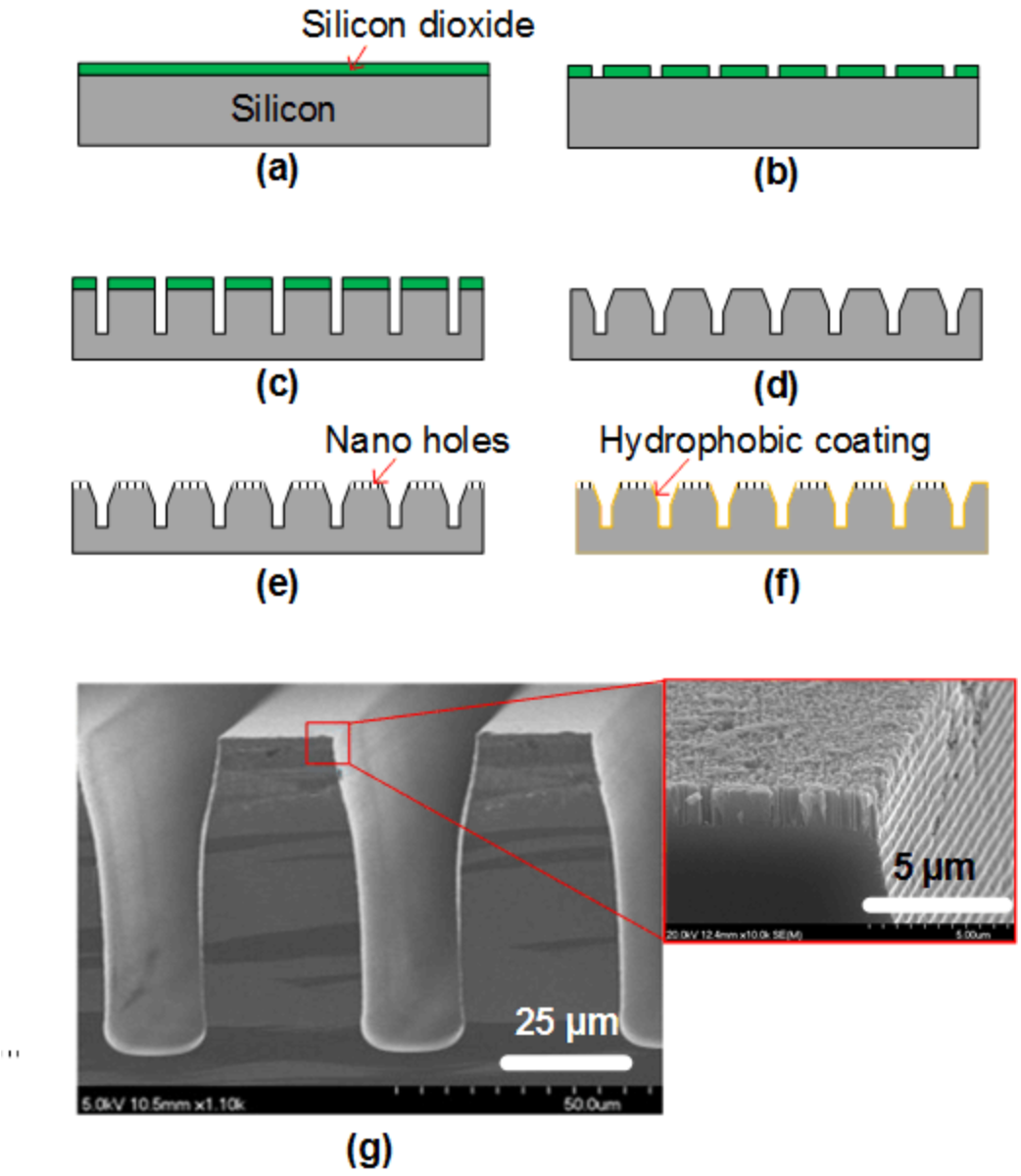

Figure 5-7 Teflon FEP SHPo surface mold fabrication. (a)-(f) Silicon mold fabrication process. (g) SEM picture of typical silicon mold showing tapered sidewall profile.

5.3.2 Molding Process

Teflon FEP is used in the molding process due to its lower glass transition temperature and cost compared with Teflon PFA. The molding process is shown in Figure 5-8, first, the electrodes were

placed between FEP film and mold (Figure 5-8(a)). The electrodes were placed perpendicular to the grating direction so that the electrodes do not substantially cover the micro-trenches. A transparent glass block was placed on top of the FEP film so the molding process could be visualized. The low heat conduction rate of glass could also ensure the Teflon FEP was not cooled from the top to ensure better temperature uniformity across the FEP film. During the molding process under applied pressure (~0.25 MPa) and at an elevated temperature (~275 $^{\circ}C$), the Teflon FEP flew around the electrodes and filled into the trenches on the mold, as shown in Figure 5-8(b). The molding time was about 4 mins. After the molding was completed, the molding pressure remained while the hot plate was actively cooled down using circulating cooling water inside the hot plate. The molding pressure was released after the temperature dropped to room temperature.

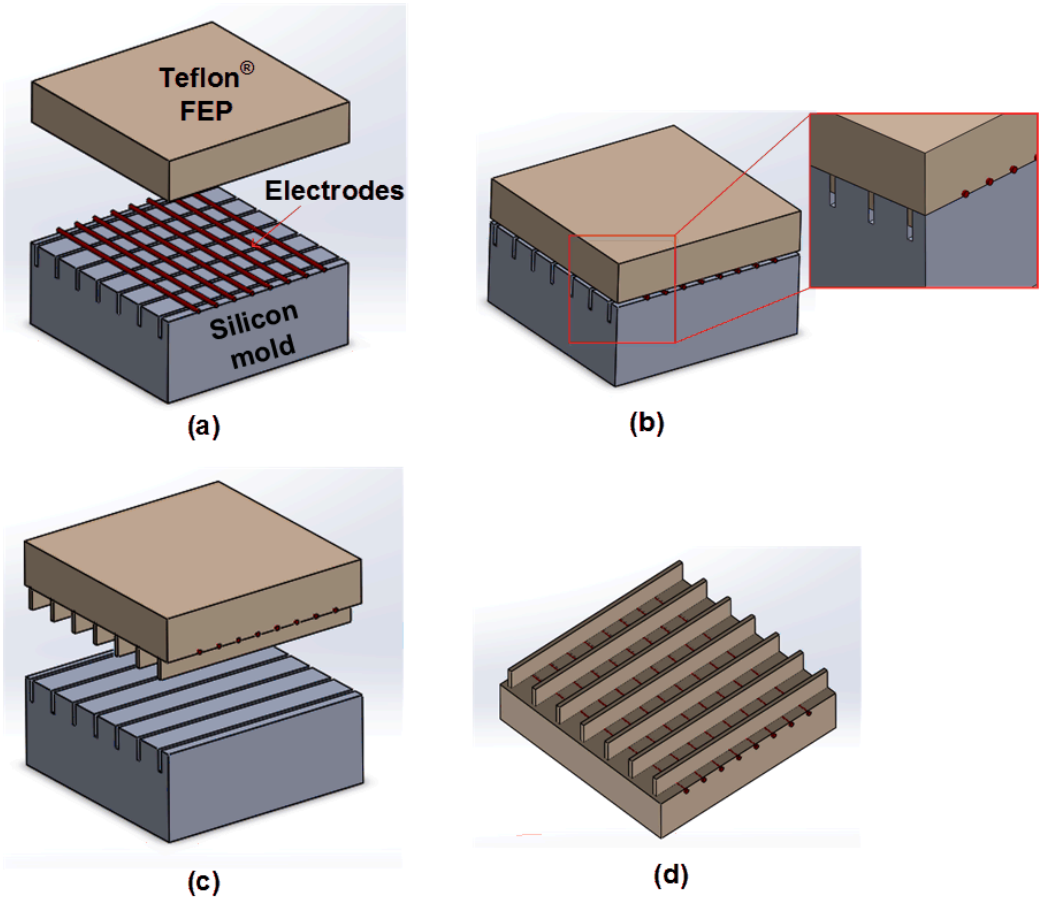

Figure 5-8 Active whole-Teflon SHPo surface fabrication process. (a) Electrodes were placed on silicon mold. (b) Molding process with Teflon FEP flew into the trench while electrodes are still in contact with mold. (c) Demolding after the mold was cooled down. (d) Final whole-Teflon SHPo surfaces with exposed electrodes at the bottom of the micro-gratings.

During the demolding process, a thin razor blade was inserted into the gap between the glass stock and the silicon mold, as shown in Figure 5-9. If the glass surface had a stronger adhesion with the Teflon FEP surface than the mold, the FEP surface would come up with the glass for successful demolding (Figure 5-9(b)). However, if the Teflon FEP SHPo surface had a stronger adhesion with the mold, the SHPo surface would stay on the mold after the glass comes off (Figure 5-9(c)). Then the SHPo surface was peeled from one end. The SHPo surfaces that came off with the glass were found to have better structure integrity. Therefore, the glass surface could be roughened to increase the adhesion to Teflon FEP.

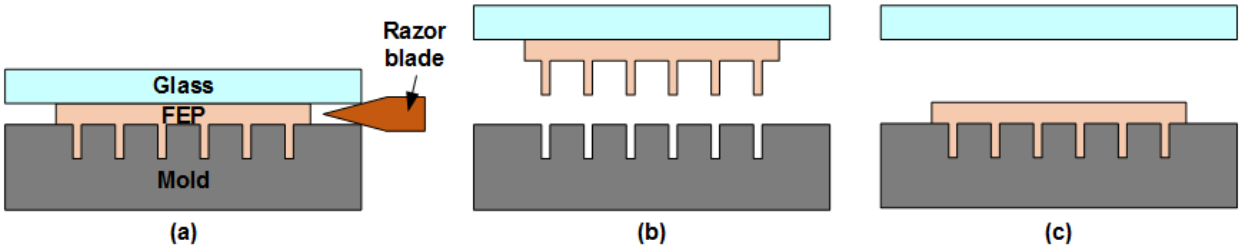

Figure 5-9 Demolding process. (a) Demolding using razor blade. (b) FEP came off with glass. (c) FEP stayed on mold after the glass comes off.

Conventional embossing or imprinting of microstructures with functional materials in between the microstructures usually requires separate fabrication steps of molding the microstructures and placing the functional materials in between the molded microstructures. The current process completes the process with only a single molding step without leaving residual layer on the

functional materials, keeping the simplicity of traditional embossing/imprinting techniques while obtaining functional materials exposed in between the microstructures. The SEM pictures in Figure 5-10 shows the exposed electrode in between the Teflon FEP gratings after molding process.

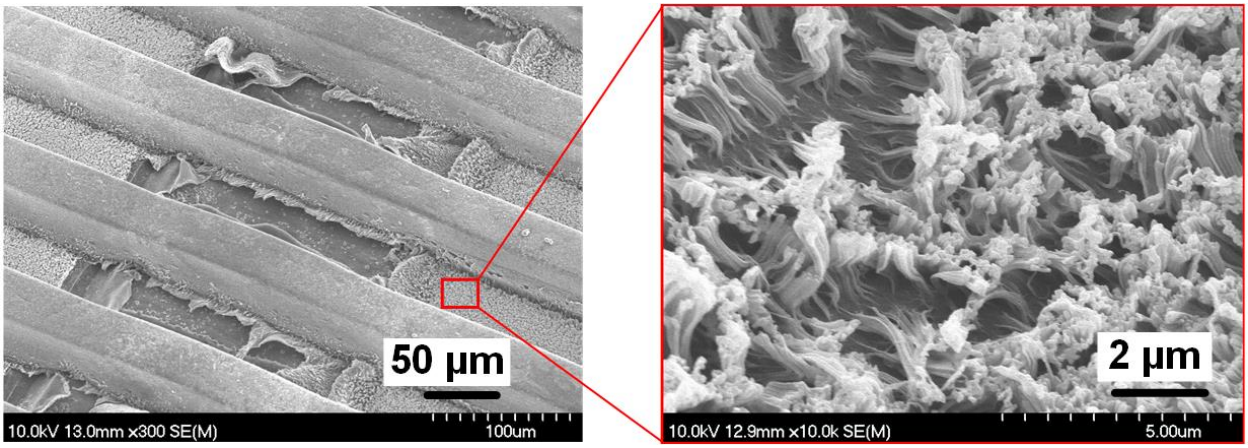

Figure 5-10 Good exposure of copper wires at the bottom of the Teflon FEP gratings with nanostructures.

5.3.3 Electrode Exposure

The key issue of this molding process is to keep electrodes exposed at the bottom of the micro-gratings rather than covered with Teflon FEP. To do this, the electrodes must be in firm contact with the mold throughout the molding process to prevent melted Teflon FEP flowing onto the electrode. Figure 5-11 showed the comparison of exposed and covered electrodes on the same surface.

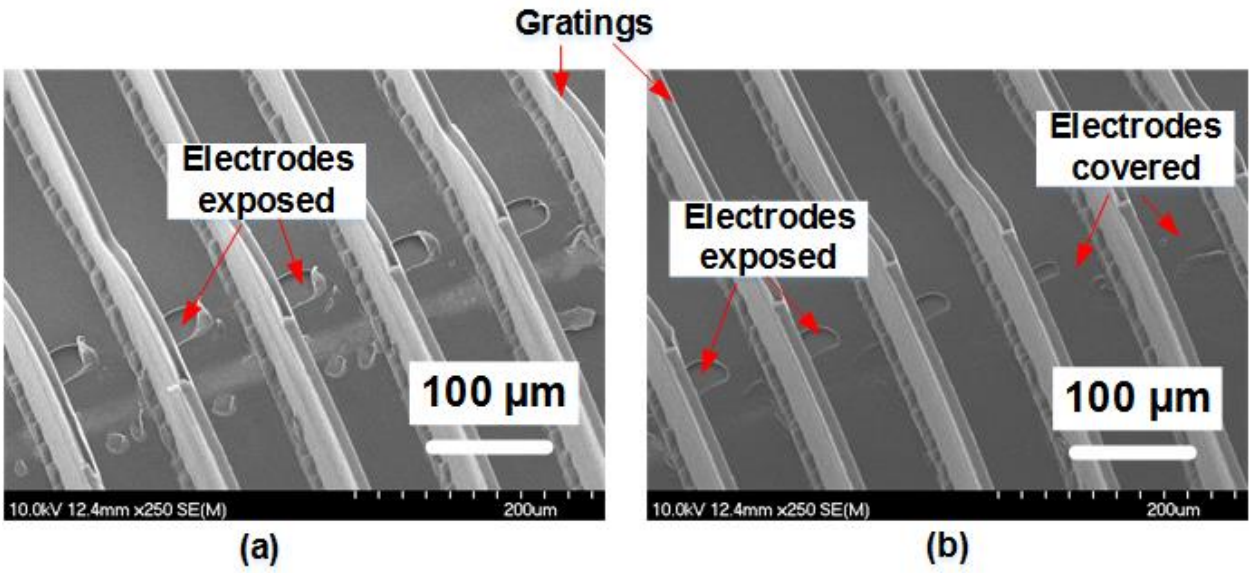

Figure 5-11 Exposed and covered electrode on semi-active Teflon FEP SHPo surface. (a) Exposed electrode. (b) Partially covered electrode.

To achieve good electrode exposure, firstly, the molding parameters, including the temperature, pressure, and time, need to be well controlled. The molding time needs to be minimized. The molding temperature should not be too much above the glass transition temperature of Teflon FEP. If the temperature is too high or molding time is too long, the Teflon FEP film will be completely melted and there will be no pressure pushing the electrodes to the mold, resulting covered electrodes. Moreover, the molding pressure and temperature need to be uniform across the sample since the overall molding time depends on the lastly finished area. If the pressure is not uniform, the firstly finished area will experience longer molding time compared with the lastly finished area, which will cause the electrodes to be covered at the firstly finished area. Lastly, it is important to keep pressure while cooling. Due to the high temperature used in the molding process and the thick glass as a heat source, it is hard to cool down the Teflon FEP film instantaneously. If the pressure

is released during the cooling process, the hot and melted Teflon FEP can still reflow onto the electrodes` surface.

Another way to improve the electrodes` exposure is to twist the electrodes (circular metal wire) after molding, as shown in Figure 5-12. If the Teflon FEP film covered on electrodes is thin, the shear stress during the twisting could remove the thin Teflon FEP film and expose the electrodes. However, if the electrodes are buried too deep inside the Teflon FEP, twisting the long and thin wire would be very difficult and might distort the grating structures as well. Therefore, controlling molding parameters is always required for optimal electrode exposure while twisting the wire could only improve the electrode exposure locally on top of good molding process.

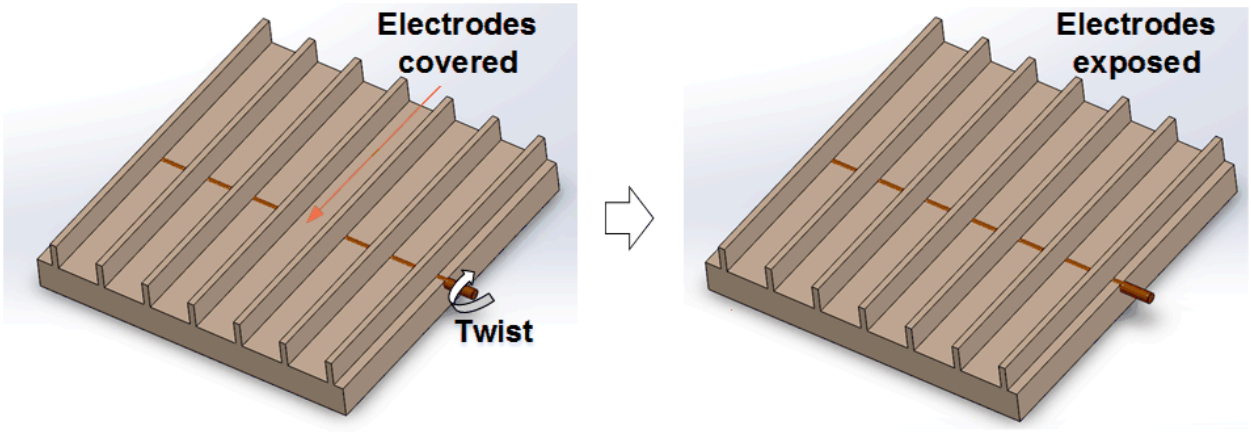

Figure 5-12 Twisting the electrode wire to exposed covered electrode locally.

5.3.4 Hot Embossing Machine

Based on requirements to ensure electrodes exposure, the hot embossing machine should be able to:

(1) precisely control the hot embossing temperature, pressure, and time.

(2) have uniform pressure and temperature distribution.

(3) have active cooling mechanisms.

As shown in Figure 5-13, our customized hot embossing machine was built on top of a commercial manual press. The dial gauge on top will display the downward displacement of the press head. Knowing the spring constant of the press head, as shown in Figure 5-13(b), the pressure can be calculated and well-controlled. The hot plate was electrically heated with feedback temperature control (not shown in figure). Cooling tubes are incorporated inside the hot plate for fast cooling using circulating tap water. The camera on the side is to observe the molding process. The pressure head, as shown in Figure 5-13(b), has a swivel pad on top which could freely rotate. The free rotation ensures the molding force to be perpendicular with the top surface of glass even with non-uniform thickness of the sample. Multiple springs were used on the press head to provide molding force. Since the Teflon FEP film thickness will decrease during the molding process, using springs instead of hard contact could ensure consistent pressure. Also, the point contact of the screw tips would prevent fast heat transfer from the top of the glass to keep molding temperature uniform across the Teflon FEP film.

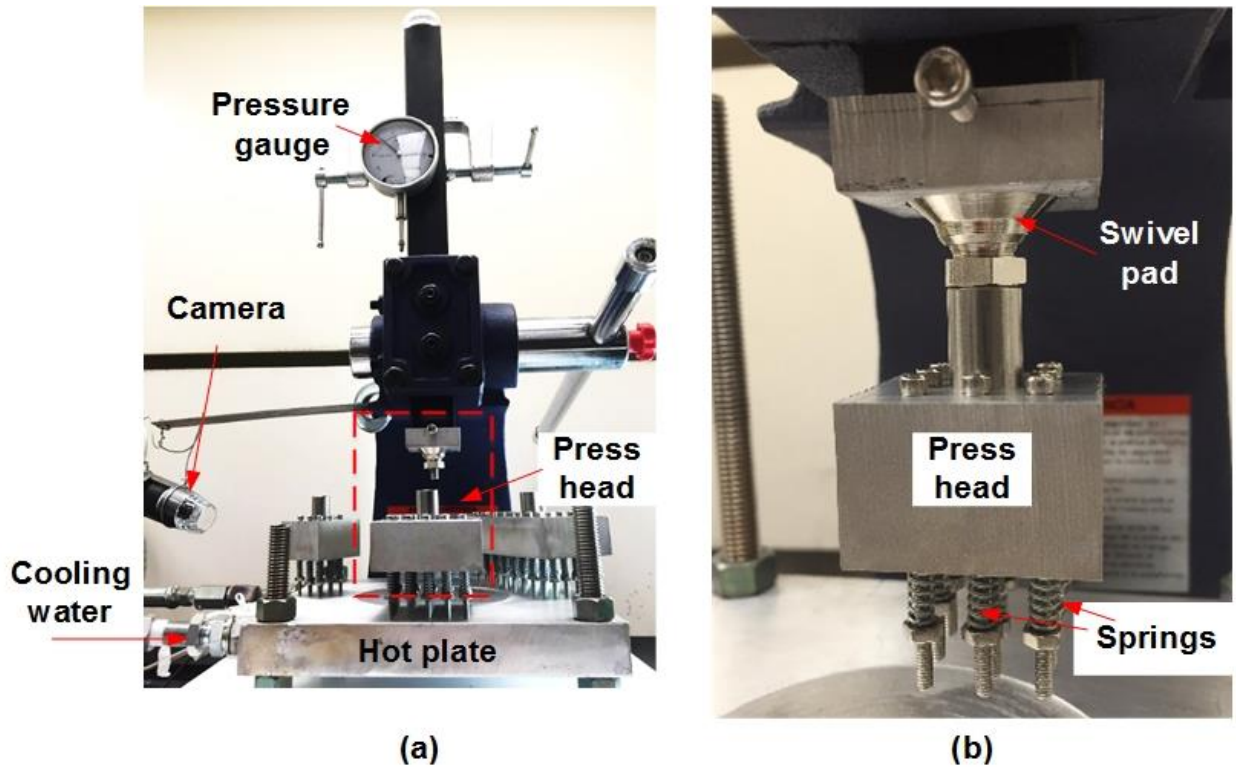

Figure 5-13 Customized hot embossing machine for fabricating semi-active Teflon SHPo surfaces.

5.4 Demonstration of Gas Restoration

5.4.1 Direct Visualization of Meniscus in Gas Generation Process

Firstly, whole-Teflon single trench sample was fabricated to visualize the meniscus change during the dewetting process from the side, similar as sample used in Chapter 2. The fabrication process is the same as described in Figure 2-2, except with electrode at the bottom using process described in Figure 5-8. The schematic of the sample is shown in Figure 5-14.

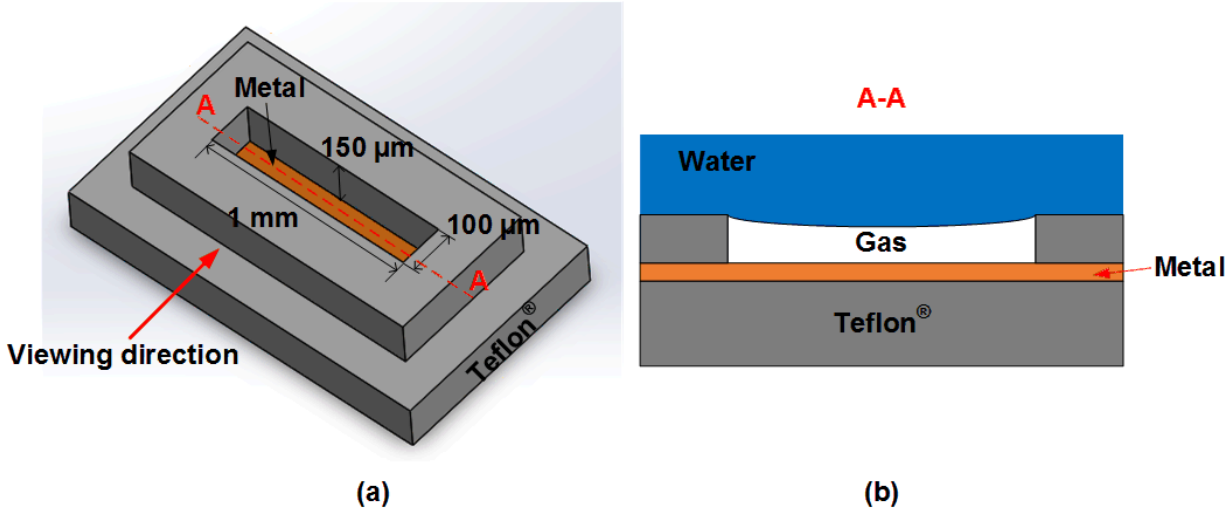

Figure 5-14 Schematic drawing of single trench semi-active SHPo surface. (a) Schematic drawing of the single trench sample and dimensions. (b) Cross section view of A-A during testing

Firstly, aluminum strip was embedded at the bottom of the single trench and tested in acid solution (hydrogen chloride solution with pH~5) to visualize the meniscus propagation inside the single trench, as shown in Figure 5-15. The single trench was initially wetted intentionally (Figure 5-15(a)). As the aluminum strip began to react with HCl solution, hydrogen was generated on the aluminum (Figure 5-15(b)) and the hydrogen bubble grew sideways (Figure 5-15(c)). Eventually, the whole trench was filled with hydrogen and the reaction stopped. As more area was covered by gas, the reaction became slower and slower, as can be seen from the time. Similar as [42], this test directly verified the gas propagation theory proposed before for active surfaces [3], which is crucial in designing SHPo surface geometry for active gas restoration. Moreover, it showed pure chemical reaction can also achieve "self-regulation" same as electrochemical process [3], where the reaction stops by itself once the dewetting process is finished.

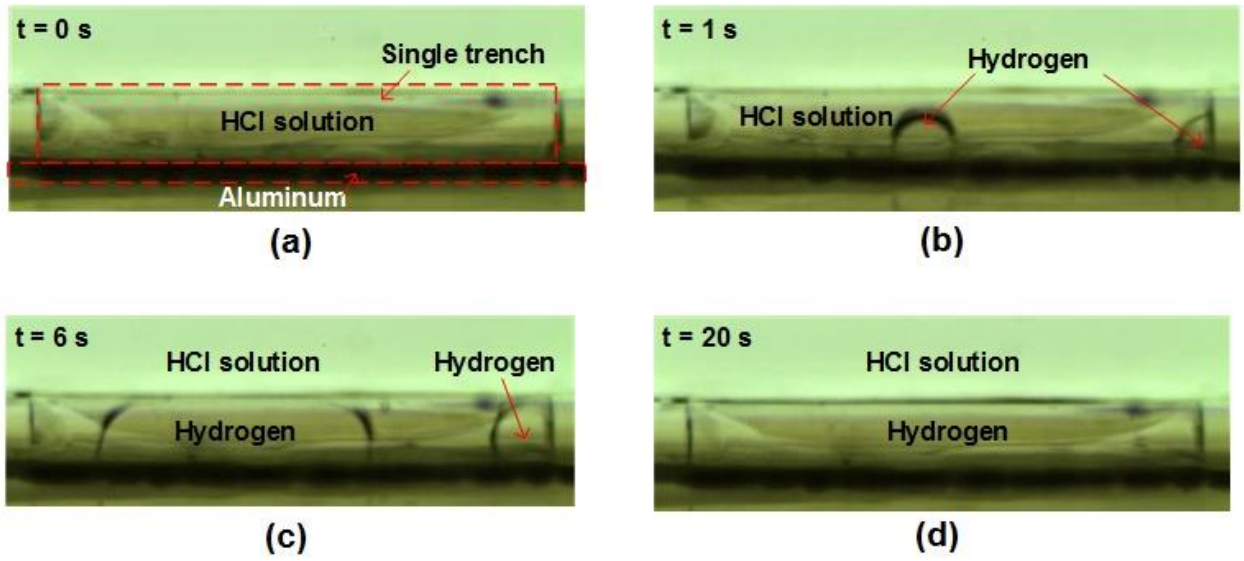

Figure 5-15 Gas restoration in Teflon FEP single trench by pure chemical reaction. (a) single trench was initially wetted (b) hydrogen bubbles began to showed up and grew (c) hydrogen began to propagate inside the single trench (d) single trench filled by hydrogen, reaction stopped

However, previous sample with aluminum can only be used in acid solutions. We then tested sample with nickel and magnesium electrodes in artificial seawater (24.53 g/L sodium chloride, 5.20 g/L magnesium chloride, 4.09 g/L sodium sulfate based on [43]), which is the main application environment for our active SHPo surfaces. As shown in Figure 5-16, nickel strip was embedded at the bottom of the single trench and connected to another magnesium strip outside the sample immersed in seawater (not shown in picture). The sample was initially dewetted, as shown in Figure 5-16 (a). At time zero, the gas in the trench was intentionally blew away (Figure 5-16 (b)). Then the gas restoration process started and quickly refilled the single trench in ~2 seconds (Figure 5-16 (c) and Figure 5-16 (d)). Compared with previous test, the reaction was much faster. This was because the large magnesium strip (~1 cm^2) outside the sample reacted fast with seawater. Meanwhile, with this self-powered process, the gas restoration was still self-regulating.

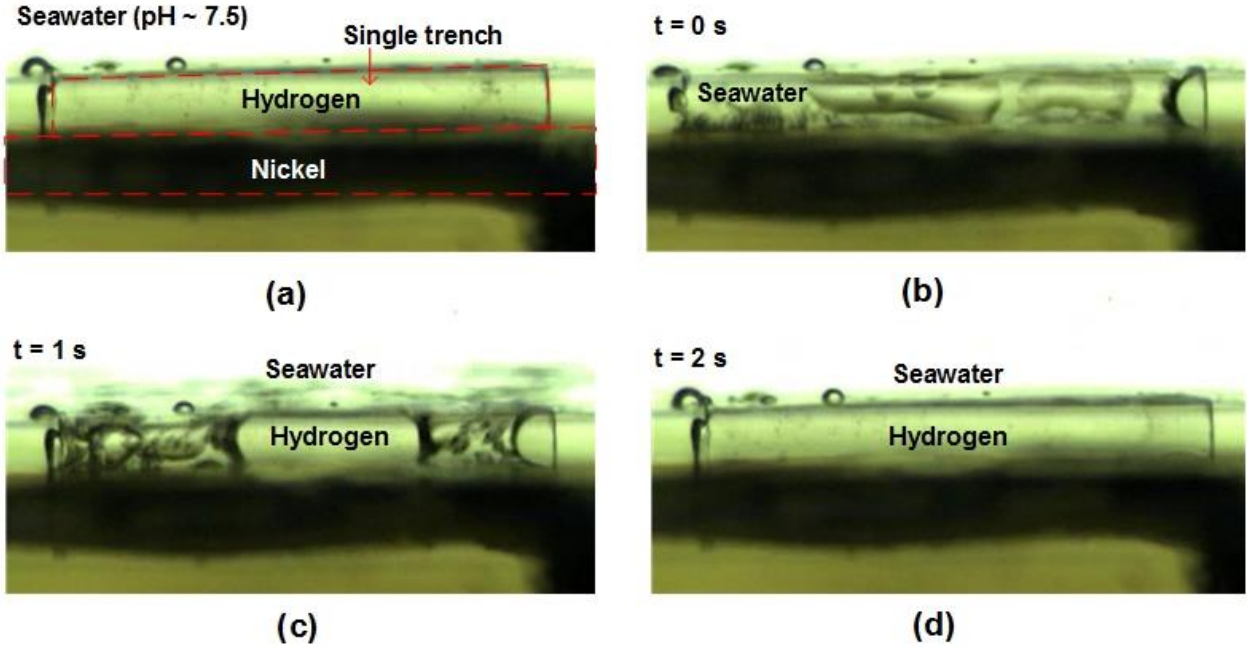

Figure 5-16 Gas restoration in Teflon FEP single trench by electrochemical reaction. (a) Single trench was initially dewetted. (b) Gas was blew out of the trench. (c) Hydrogen began to generate and propagate inside the single trench. (d) Single trench filled by hydrogen, reaction stopped.

5.4.2 Gas Generation with External Power Source

After verifying the gas restoration process in single micro trench made of Teflon, we fabricated actual semi-active SHPo surface made of micro-gratings for gas restoration test. Firstly, we only embedded one electrode underneath the SHPo surface gratings, as shown in Figure 5-17. The micro-gratings had 100 μm pitch, 50% gas fraction and 150 μm grating height without nanostructures at the bottom of the gratings. The wire was connected to outside power source with constant current (~0.1 mA). The sample was initially wetted in seawater (Figure 5-17(a)). As can be seen from the figure, the gas (dark lines) began to propagate along the gratings once the power was on (Figure 5-17(b)(c)) and eventually stopped (Figure 5-17(d)). However, the whole surface

had not fully dewetted yet. Some gas columns stopped growing before reaching the ends. This is because there were imperfections (e.g., bumps, particles) in the trench between the gratings. The imperfections caused too much resistance for gas propagation and the exposed electrodes was covered by gas and reaction stopped before the gas could overcome the resistance.

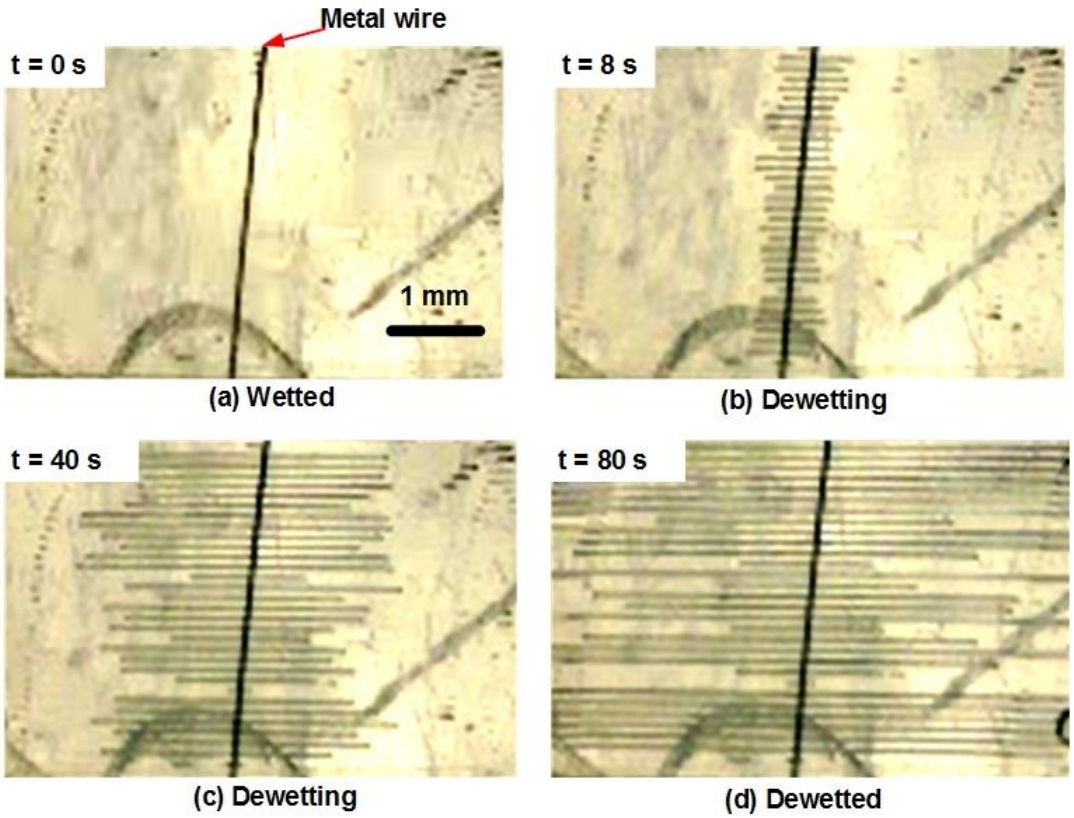

Figure 5-17 Gas restoration on whole-Teflon SHPo surface with single electrode and no nanostructure at bottom of micro-gratings.

To solve this problem, we embedded more electrodes underneath the micro-gratings, as shown in Figure 5-18. The SHPo surface had the same size and surface parameters as the one discussed above. As can be seen from this figure, gas (dark lines) started to propagate from all electrodes and different gas columns merged with each other (Figure 5-18(b)(c)). Since there were more than

one gas generating sites in each micro-trench, the final dewetted area was larger compared with that of single electrodes showed above.

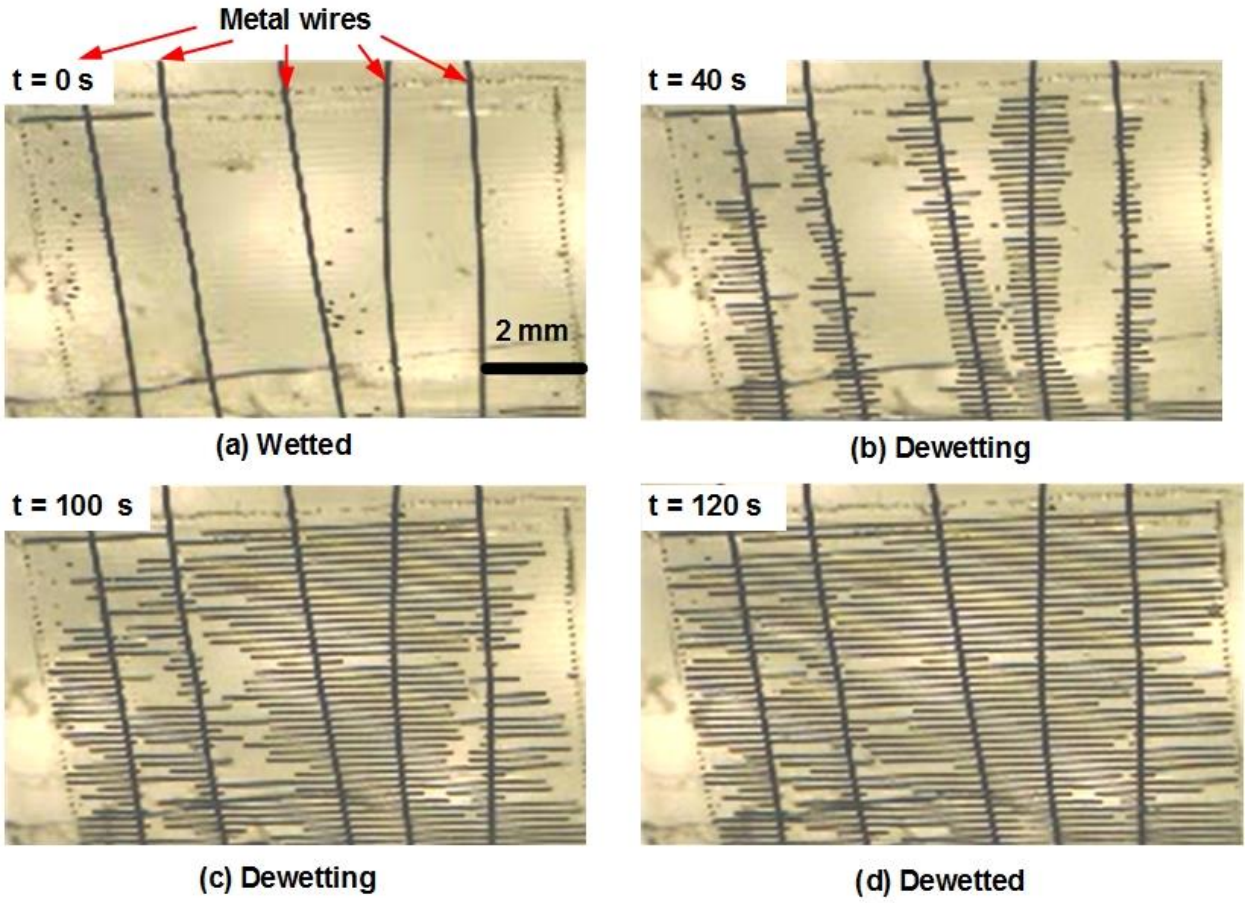

Figure 5-18 Gas restoration on whole-Teflon SHPo surface with multiple electrodes and no nanostructure at bottom of micro-gratings.

However, the multiple-electrodes sample used above still requires high aspect ratio gratings for successful gas propagation due to relatively low receding contact angle on grating sidewall and bottom. This is challenging for the fabrication process, especially the demolding process. Moreover, dirty particles in seawater were found to be left on the bottom of the grating after one run, making it less hydrophobic and hampering gas propagation. After several runs, the gas tended

to bulge out instead of propagating due to reduced hydrophobicity and increased resistance at the grating bottom. To solve these problems, we added nanostructure "nanograss" at the bottom of the gratings, as shown in Figure 5-5. The nanostructures were also fabricated during the molding process and didn`t add additional complications to the whole process. Figure 5-19 showed the performance of SHPo surface with nanostructures at the bottom with bright lines indicating gas. This SHPo surface had 100 μm pitch, 50% gas fraction and only 50 μm grating height. Constant current of ~0.5 mA was used through the single metal wire. As can be seen from this figure, much less time was needed due to reduced grating height (less gas needed) and higher current. The SHPo surface was initially wetted (Figure 5-19(a)). Once the power was on, gas started to generate all over the surface, different from previous cases. With nanostructure at bottom, we found there was usually a residual gas layer at bottom supported by the nanostructure, which was very stable [15]. Once the gas generation started at the electrodes, instead of propagating, the whole residual gas layer started to grow up since they are connected, as shown in Figure 5-19(b)(c). The whole surface was eventually dewetted (Figure 5-19(d), resulting better gas coverage than previous cases.

With nanostructure at the bottom, demolding became more difficult so a hydrophobic layer (e.g., fluoropolymer coating) is needed. However, the reduced grating height could prevent grating distortion especially when the grating gets thin with high gas fraction SHPo surfaces. Moreover, less gas was generated which led to less power consumption. Lastly, with high water-repellent "nanograss" at the bottom and a residual layer of gas, hydrophilic particles and organisms in seawater were more difficult to reside [44] at the bottom, which makes the surface more robust. The above surface was tested 20 more cycles of dewetting process without indication of fouling.

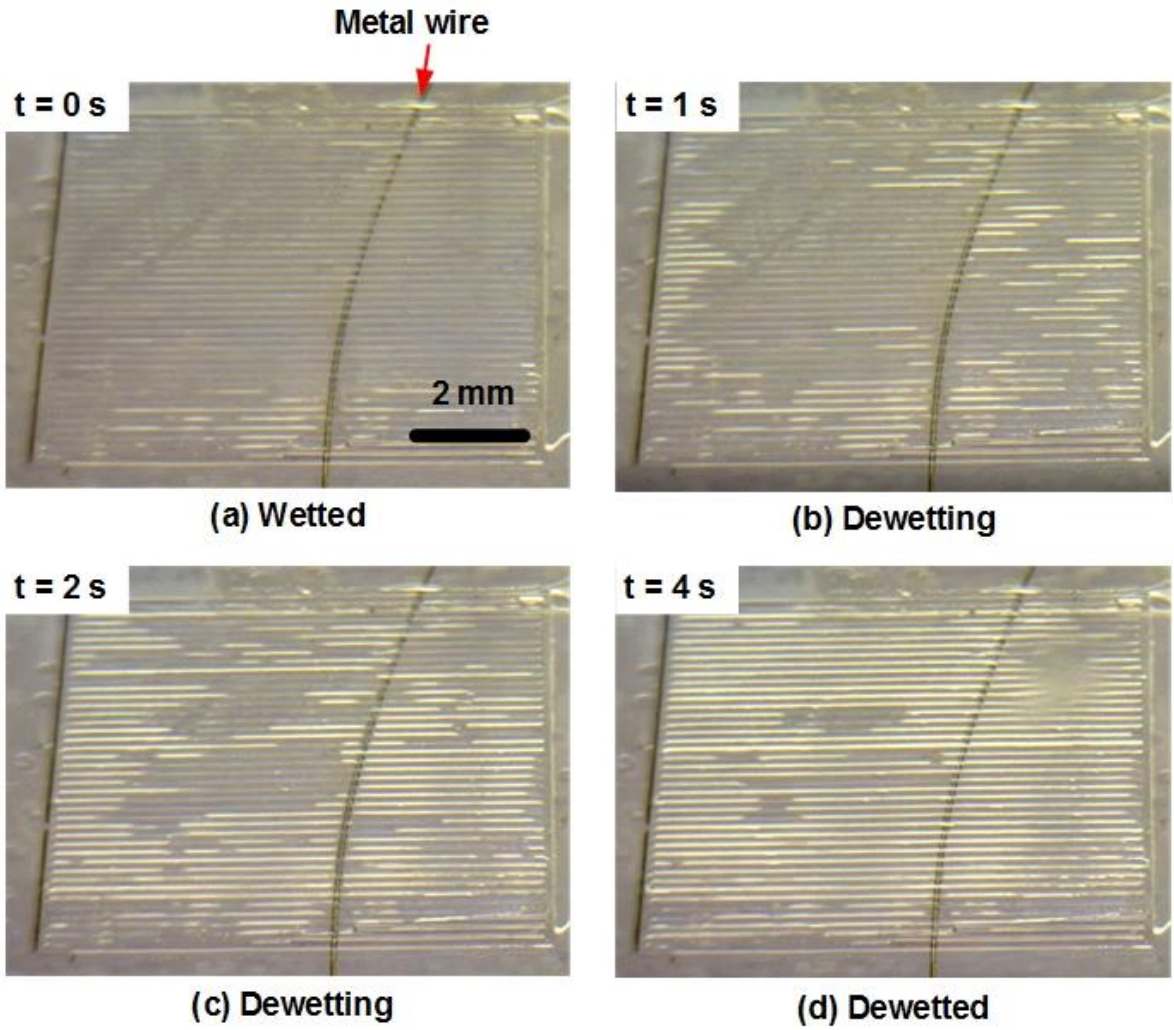

Figure 5-19 Gas restoration on whole-Teflon SHPo surface with nanostructures at bottom of micro-gratings.

5.4.3 Gas Generation with Built-in Power Sources

To verify the self-powered gas restoration mechanism, we fabricated whole-Teflon SHPo surface with built-in electrochemical reactors. As shown in Figure 5-20, two types of surfaces were tested: the first type of SHPo surface (Figure 5-20(a)(b)) had copper wires embedded underneath the gratings and connected to outside magnesium strip, which was immersed in water. The different electrode potential between these two materials will trigger electrochemical reaction once the

copper gets wet. Then gas would be generated on copper surface. The second type of SHPo surface (Figure 5-20(c)(d)) has both magnesium and copper underneath the grating which were electrically connected to each other. Once both of these two materials get wet, the electrochemical reaction will be triggered and generate gas on copper surface.

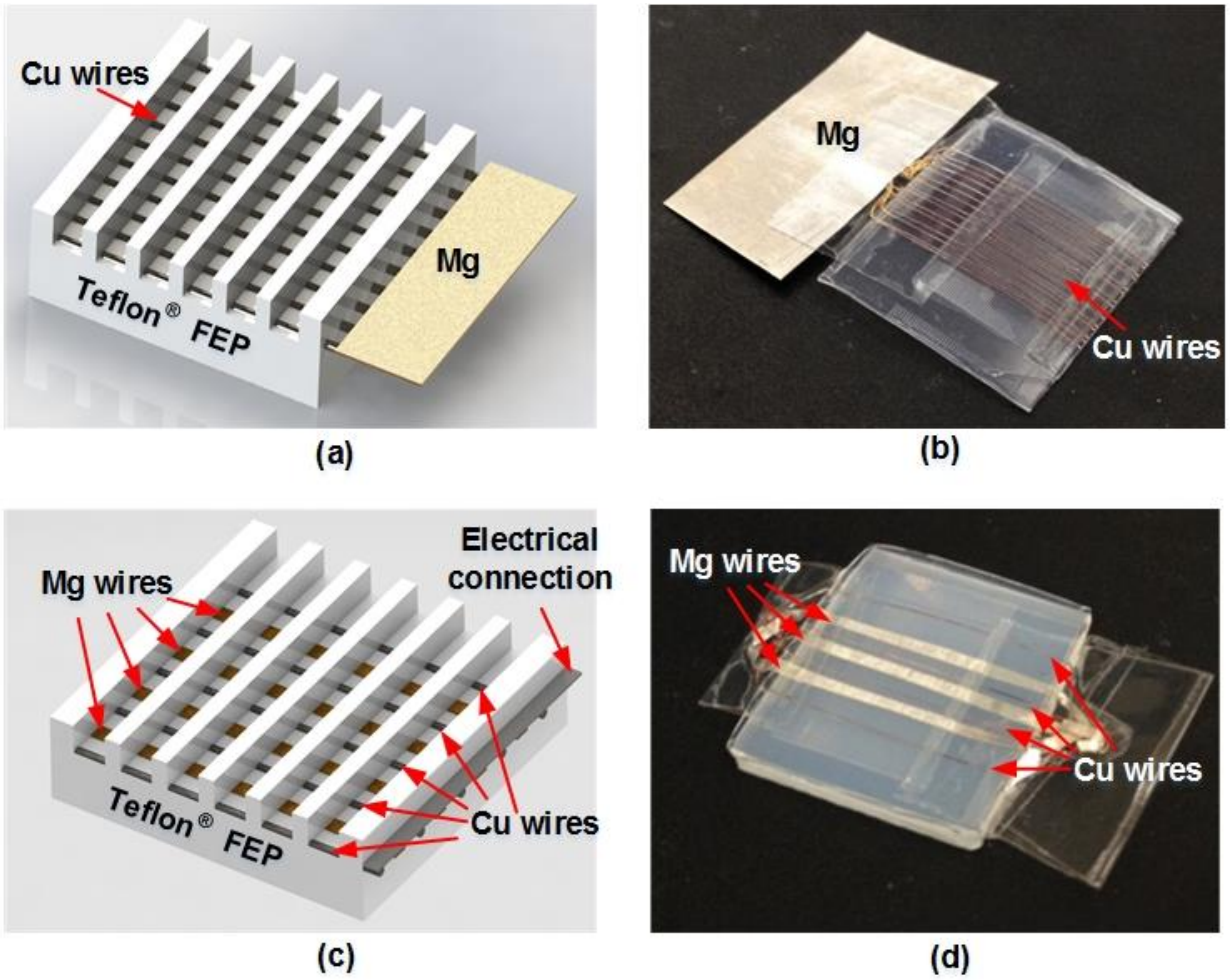

Figure 5-20 Schematic drawing and pictures of self-powered semi-active whole-Teflon SHPo surface. (a) SHPo surface with magnesium outside. (b) SHPo surface with magnesium underneath gratings.

Figure 5-21 shows the gas restoration for self-powered whole-Teflon SHPo surface with copper electrodes underneath micro-gratings and magnesium electrodes outside the sample (not shown in figure). The geometry of SHPo surface was same as the one shown in Figure 5-17. The SHPo surface was initially dewetted with gas shown as dark lines (Figure 5-21(a)). At time = 0, the gas was intentionally blow away and the reaction started (Figure 5-21(b)). The gas propagated similarly as the SHPo surface with outside power source (Figure 5-21(c)). The whole surface was eventually dewetted and reaction stopped (Figure 5-21(d)).

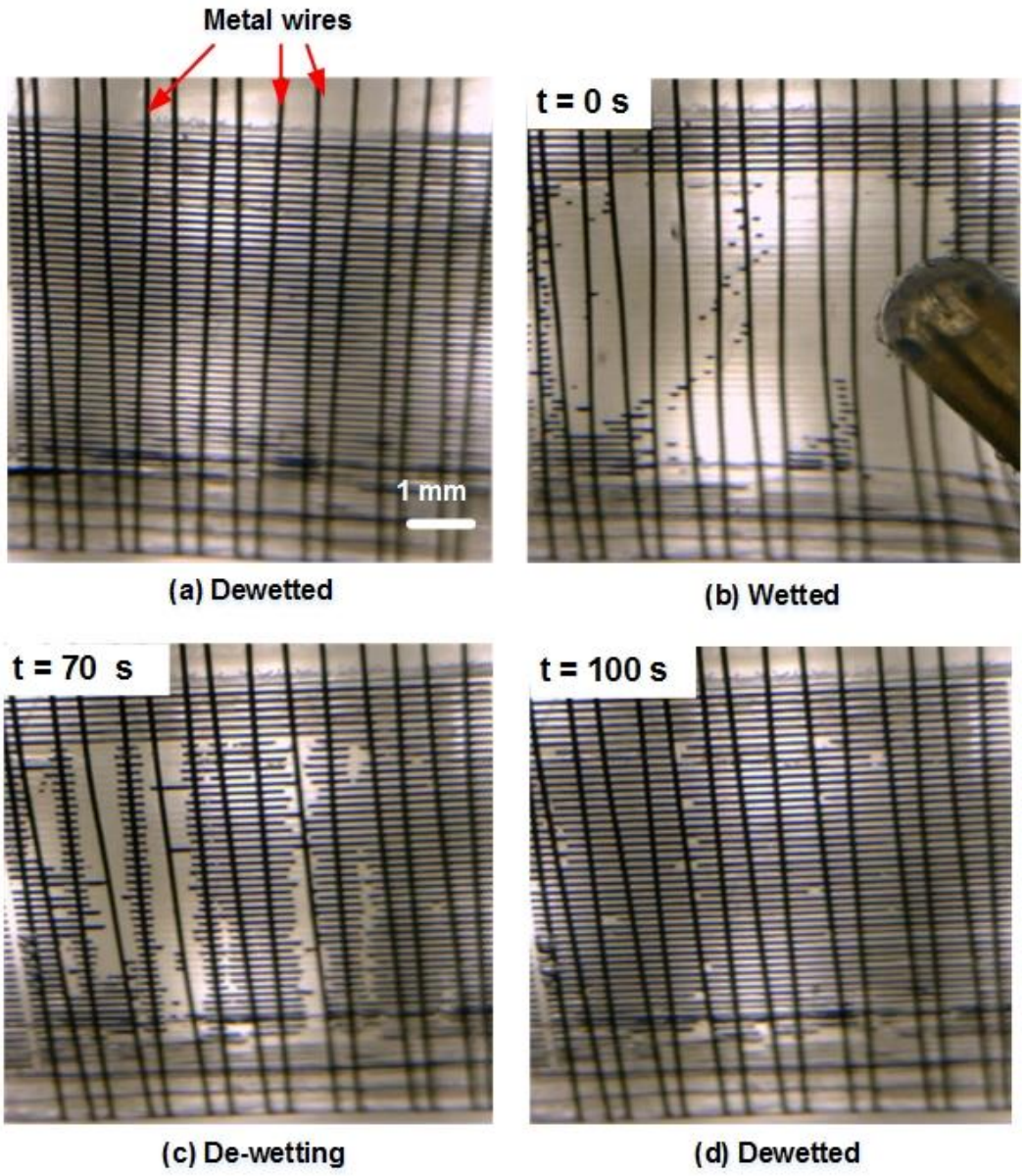

Figure 5-21 Gas restoration on self-powered whole-Teflon SHPo surface with copper electrode underneath micro-gratings and magnesium electrode immersed in seawater.

Figure 5-22 shows the gas restoration for self-powered whole-Teflon SHPo surface with both copper (thin wire) and magnesium electrode (thick wire) embedded underneath the micro-gratings. The geometry of SHPo surface was the same as previous one. Wide magnesium strips were used

due to unavailability of commercial thin magnesium wires. The SHPo surface was initially dewetted with gas shown as dark lines (Figure 5-22(a)). At time = 0, the gas was intentionally blow away and the reaction started (Figure 5-22(b)). The gas propagated much slower than previous type of surface with magnesium immersed in water. This reduced reaction speed is due to reduced magnesium reaction area. Moreover, parts of the surface were never dewetted since the copper wires were too far from each other with thick magnesium strip sitting in between. The reaction didn`t stop even after the copper wire was covered by gas. This is because the magnesium strips were too wide and hydrophilic to be covered by gas with magnesium itself reacting slowly with seawater. As a result, bulging bubbles were observed at the end of the test (Figure 5-22(d)).

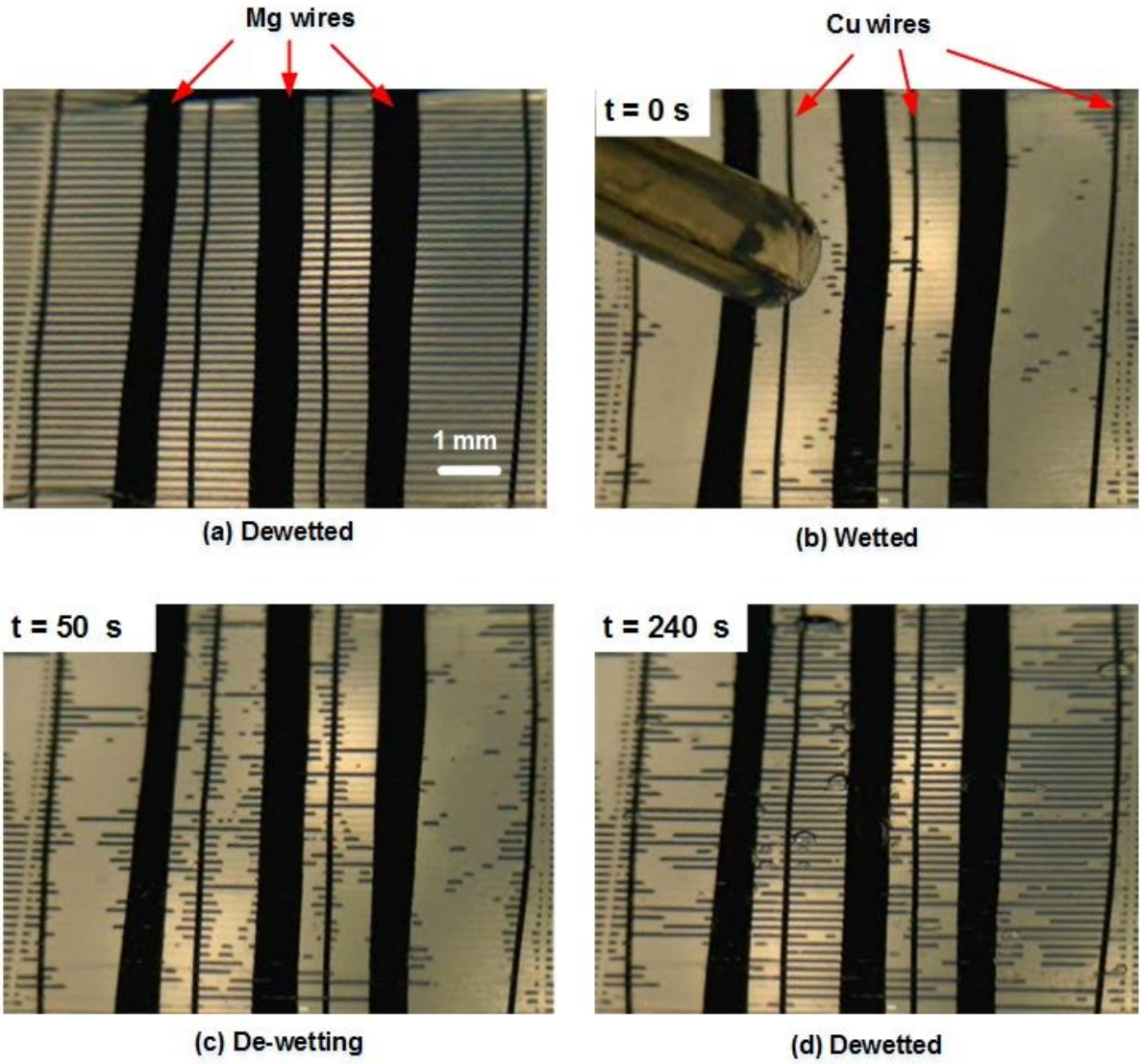

Figure 5-22 Gas restoration on self-powered whole-Teflon SHPo surface with both copper magnesium electrodes embedded underneath the micro-gratings.

5.5 Summary

In summary, we developed a novel mass-manufacturing process to fabrication whole-Teflon SHPo surfaces. The one-step hot embossing process can incorporate electrodes into the SHPo surface for self-regulating gas restoration process, which is the key technology to make the drag reduction sustainable under realistic conditions. Lastly, we developed a self-powered gas restoration

mechanism, which could dewet the SHPo surface without any external power input. The mass manufacturing process as well as the self-powered gas restoration mechanism was successfully demonstrated. The electrode geometry and material selection could be further optimized.

5.6 References

[1] K. N. Ren, W. Dai, J. H. Zhou, J. Su, and H. K. Wu, "Whole-Teflon microfluidic chips," *Proceedings of the National Academy of Sciences of the United States of America*, vol. 108, pp. 8162-8166, 2011.

[2] C. Lee and C.-J. Kim, "Maximizing the giant liquid slip on superhydrophobic microstructures by nanostructuring their sidewalls," *Langmuir*, vol. 25, pp. 12812-12818, 2009.

[3] C. Lee and C.-J. Kim, "Underwater Restoration and Retention of Gases on Superhydrophobic Surfaces for Drag Reduction," *Physical Review Letters*, vol. 106, 14502, 2011.

[4] H. Park, G. Sun, and C.-J. Kim, "Superhydrophobic turbulent drag reduction as a function of surface grating parameters," *Journal of Fluid Mechanics*, vol. 747, pp. 722-734, 2014.

[5] B. Woolford, J. Prince, D. Maynes, and B. W. Webb, "Particle image velocimetry characterization of turbulent channel flow with rib patterned superhydrophobic walls," *Physics of Fluids*, vol. 21, 085106, 2009.

[6] M. G. Pollack, R. B. Fair, and A. D. Shenderov, "Electrowetting-based actuation of liquid droplets for microfluidic applications," *Applied Physics Letters*, vol. 77, pp. 1725-1726, 2000.

[7] V. Srinivasan, V. K. Pamula, and R. B. Fair, "An integrated digital microfluidic lab-on-a-chip for clinical diagnostics on human physiological fluids," *Lab on a Chip*, vol. 4, pp. 310-315, 2004.

[8] S. K. Cho, H. Moon, and C.-J. Kim, "Creating, transporting, cutting, and merging liquid droplets by electrowetting-based actuation for digital microfluidic circuits," *Microelectromechanical Systems, Journal of*, vol. 12, pp. 70-80, 2003.

[9] A. R. Wheeler, H. Moon, C. A. Bird, R. R. Ogorzalek Loo, C.-J. C. Kim, J. A. Loo, *et al.*, "Digital microfluidics with in-line sample purification for proteomics analyses with MALDI-MS," *Analytical Chemistry*, vol. 77, pp. 534-540, 2005.

[10] M. Xu, G. Sun, and C.-J. Kim, "Infinite Lifetime of Underwater Superhydrophobic States," *Physical review Letters*, 2014.

[11] T. W. de Haas, H. Fadaei, and D. Sinton, "Laminated thin-film Teflon chips for petrochemical applications," *Lab on a Chip*, vol. 12, pp. 4236-4239, 2012.

[12] E. Aljallis, M. A. Sarshar, R. Datla, V. Sikka, A. Jones, and C. H. Choi, "Experimental study of skin friction drag reduction on superhydrophobic flat plates in high Reynolds number boundary layer flow," *Physics of Fluids*, vol. 25, 2013.

[13] R. J. Daniello, N. E. Waterhouse, and J. P. Rothstein, "Drag reduction in turbulent flows over superhydrophobic surfaces," *Physics of Fluids,* vol. 21, 085103, 2009.

[14] R. A. Bidkar, L. Leblanc, A. J. Kulkarni, V. Bahadur, S. L. Ceccio, and M. Perlin, "Skin-friction drag reduction in the turbulent regime using random-textured hydrophobic surfaces," *Physics of Fluids,* vol. 26, pp. -, 2014.

[15] M. Xu, G. Sun, and C.-J. Kim, "Infinite Lifetime of Underwater Superhydrophobic States," *Physical Review Letters,* vol. 113, 136103, 2014.

[16] L. Bocquet and E. Lauga, "A Smooth Future?," *Nature Materials,* vol. 10, pp. 334-337, 2011.

[17] C. Lee and C.-J. Kim, "Wetting and Active Dewetting Processes of Hierarchically Constructed Superhydrophobic Surfaces Fully Immersed in Water," *Journal of Microelectromechanical Systems,* vol. 21, pp. 712-720, 2012.

[18] K. B. Golovin, J. W. Gose, M. Perlin, S. L. Ceccio, and A. Tuteja, "Bioinspired surfaces for turbulent drag reduction," *Phil. Trans. R. Soc. A,* vol. 374, 20160189, 2016.

[19] C.-J. Kim and C. Lee, "Method and device for restoring and maintaining superhydrophobicity under liquid," U.S. Patent 20130122195 A1, July 22, 2011.

[20] S. Türk, G. Daschiel, A. Stroh, Y. Hasegawa, and B. Frohnapfel, "Turbulent flow over superhydrophobic surfaces with streamwise grooves," *Journal of Fluid Mechanics,* vol. 747, pp. 186-217, 2014.

[21] C. J. Teo and B. C. Khoo, "Flow past superhydrophobic surfaces containing longitudinal grooves: effects of interface curvature," *Microfluidics and Nanofluidics,* vol. 9, pp. 499-511, 2010.

[22] E. Lauga and H. A. Stone, "Effective slip in pressure-driven Stokes flow," *Journal of Fluid Mechanics,* vol. 489, pp. 55-77, 2003.

[23] C. Lee, C.-H. Choi, and C.-J. Kim, "Structured surfaces for a giant liquid slip," *Physical Review Letters,* vol. 101, 64501, 2008.

[24] H. Park, H. Park, and J. Kim, "A numerical study of the effects of superhydrophobic surface on skin-friction drag in turbulent channel flow," *Physics of Fluids,* vol. 25, 110815, 2013.

[25] T. G. Min and J. Kim, "Effects of hydrophobic surface on skin-friction drag," *Physics of Fluids,* vol. 16, pp. L55-L58, 2004.

[26] P. Papadopoulos, L. Mammen, X. Deng, D. Vollmer, and H.-J. Butt, "How superhydrophobicity breaks down," *Proceedings of the National Academy of Sciences,* vol. 110, pp. 3254-3258, 2013.

[27] S. K. Aghdam and P. Ricco, "Laminar and turbulent flows over hydrophobic surfaces with shear-dependent slip length," *Physics of Fluids,* vol. 28, 035109, 2016.

[28] E. Karatay, A. S. Haase, C. W. Visser, C. Sun, D. Lohse, P. A. Tsai, *et al.*, "Control of slippage with tunable bubble mattresses," *Proceedings of the National Academy of Sciences of the United States of America,* vol. 110, pp. 8422-8426, 2013.

[29] D. G. Crowdy, "Analytical formulae for longitudinal slip lengths over unidirectional superhydrophobic surfaces with curved menisci," *Journal of Fluid Mechanics,* vol. 791, 2016.

[30] W. Barthlott, T. Schimmel, S. Wiersch, K. Koch, M. Brede, M. Barczewski, *et al.*, "The Salvinia paradox: Superhydrophobic surfaces with hydrophilic pins for air retention under water," *Advanced Materials,* vol. 22, pp. 2325-2328, 2010.

[31] M. Worgull, *Hot embossing: theory and technology of microreplication*: William Andrew, 2009.

[32] M. Worgull, M. Heckele, and W. Schomburg, "Large-scale hot embossing," *Microsystem technologies,* vol. 12, pp. 110-115, 2005.

[33] M. Worgull, J. Hetu, K. Kabanemi, and M. Heckele, "Modeling and optimization of the hot embossing process for micro-and nanocomponent fabrication," *Journal of Micro/Nanolithography, MEMS, and MOEMS,* vol. 5, pp. 011005-011005-13, 2006.

[34] M. Worgull, A. Kolew, M. Heilig, M. Schneider, H. Dinglreiter, and B. Rapp, "Hot embossing of high performance polymers," *Microsystem Technologies-Micro-and Nanosystems-Information Storage and Processing Systems,* vol. 17, pp. 585-592, 2011.

[35] Z. Song, J. Choi, B. H. You, J. Lee, and S. Park, "Simulation study on stress and deformation of polymeric patterns during the demolding process in thermal imprint lithography," *Journal of Vacuum Science & Technology B,* vol. 26, pp. 598-605, 2008.

[36] Y. H. Guo, G. Liu, X. L. Zhu, and Y. C. Tian, "Analysis of the demolding forces during hot embossing," *Microsystem Technologies-Micro-and Nanosystems-Information Storage and Processing Systems,* vol. 13, pp. 411-415, 2007.

[37] M. E. Dirckx and D. E. Hardt, "Analysis and characterization of demolding of hot embossed polymer microstructures," *Journal of Micromechanics and Microengineering,* vol. 21, 085024, 2011.

[38] M. E. Dirckx, "Demolding of Hot Embossed Polymer Microstructure," Ph.D. Thesis, Mechanical Engineering, Massachusetts Institute of Technology, Cambridge, Massachusetts, 2010.

[39] V. Trabadelo, H. Schift, S. Merino, S. Bellini, and J. Gobrecht, "Measurement of demolding forces in full wafer thermal nanoimprint," *Microelectronic Engineering,* vol. 85, pp. 907-909, 2008.

[40] D. Zhang, R. Jia, C. Chen, W. Ding, Z. Jin, X. Liu, *et al.*, "Reflectance and minority carrier lifetime of silicon nanoholes synthesized by chemical etching method," *Chemical Physics Letters*, vol. 601, pp. 69-73, 2014.

[41] G. Y. Sun, H. Park, and C. J. Kim, "Development of a Miniature Shear Sensor for Direct Comparison of Skin-Friction Drags," *Journal of Microelectromechanical Systems*, vol. 24, pp. 1426-1435, 2015.

[42] R. Freeman, A. C. Houck, and C. J. Kim, "Visualization of self-limiting electrochemical gas generation to recover underwater superhydrophobicity," in *Solid-State Sensors, Actuators and Microsystems (TRANSDUCERS), 2015 Transducers - 2015 18th International Conference on*, 2015, pp. 1818-1821.

[43] "Standard Practice for the Preparation of Substitute Ocean Water," ASTM D 1141-98, 1998.

[44] C. H. Choi and C. J. Kim, "Droplet Evaporation of Pure Water and Protein Solution on Nanostructured Superhydrophobic Surfaces of Varying Heights," *Langmuir*, vol. 25, pp. 7561-7567, 2009.

Chapter 6 Summary and Outlook

6.1 Summary

In this dissertation, we systematically explored the idea of using superhydrophobic (SHPo) surfaces for drag reduction in realistic turbulent flows. Our research has focused on three critical issues in achieving practical drag reduction using SHPo surfaces: robustness and lifetime of the plastron, i.e., the gas layer on SHPo surface under water; drag reduction amount at high Reynolds number turbulent boundary layer (TBL) flows; and mass manufacturing of SHPo surfaces.

We began with the study of plastron robustness on immersed SHPo surface, since the plastron is the foundation of SHPo drag reduction. By varying the SHPo surface geometry and sample immersion depth, we unveiled the relationship between the lifetime of underwater superhydrophobicity and geometric parameters, as well as immersion depth. An analytical model was built to predict the lifetime, as well as the "critical depth", above which the plastron could last infinitely. With experimental data matching analytical model well, infinite underwater superhydrophobicity was obtained on artificial SHPo surface for the first time. However, this study showed this infinite lifetime is not possible for the SHPo surfaces capable of providing a significant drag reduction. Active gas replenishing is necessary.

After understanding the gas robustness for underwater SHPo surfaces, we started to quantify the drag reduction of SHPo surfaces in TBL flow, which reported large discrepancies in previous studies. Due to the lack of reliable and compact sensors that are compatible with a variety of flow facilities, novel shear stress sensors with superior performance was developed first. Using the new sensor, single SHPo surface sample with different surface geometries could be tested repeatedly and accurately at different flow facilities (e.g., towing tank, water tunnel). Drag reduction as high

as ~25% was observed for the first time at high-speed towing tank facility, which holds the closest resemblance to actual marine vessels. The Reynolds number effect, predicted in numerical studies but never observed in large flow facilities, was confirmed in both high-speed water tunnel and towing tank. Moreover, the very first seawater field test with SHPo surfaces on actual marine vessels was conducted and ~20% drag reduction was achieved with more reduction at higher speeds.

Finally, we explored the mass manufacturing technologies, which pose the main roadblocks preventing large-scale application. Maintaining the simplicity of one-step hot embossing process, our novel process managed to obtain hierarchical SHPo surfaces with electrodes embedded at the bottom of the microstructures. The embedded electrodes allowed us to use electrolysis for gas restoration to realize realistic infinite lifetime and minimum energy consumption. The whole SHPo microstructure was monolithically made of Teflon, known for its superior hydrophobicity and chemical resistance. Moreover, a self-powered gas restoration mechanism was developed with SHPo surface sample fabricated using the developed mass manufacturing technology. This new type of SHPo surface could restore dewetted state without external power input and terminate the reaction by itself after the surface dewetted. All in all, with demonstrated drag reduction in high Reynolds number turbulent flow and mass manufacturing technology to fabricate robust SHPo surface that could actively maintain gas layer, we expect this study will accelerate the progress towards realistic drag reduction.

6.2 Outlook

Passive SHPo surfaces have shown ~25% drag reduction at high Reynolds numbers but also experienced wetting transition in significant portions of the surface. Semi-active SHPo surface developed using the new mass manufacturing technology should be tested at high Reynolds number with the expectation of higher drag reductions. With semi-active SHPo surface that stays in the Cassie state and the advancement in numerical studies, the discrepancies between numerical and experimental results may be finally eliminated. This will greatly help understand SHPo drag reduction mechanism in turbulent flows with reliable drag reduction predictions.

For practical applications, with the successful demonstration of drag reduction in field condition, it is time to test larger-scale applications on larger marine vessels. To do this, machineries that could implement current hot embossing process and fabrication large-scale SHPo surfaces need to be developed. Current hot embossing technique also needs to be improved for better electrode exposure. Meanwhile, current testing boat has shallow immersion depth with large waves, creating bubbles in favor of the drag reduction. Larger and deeper marine vessels are desired to test the drag reduction performance without being assisted by the bubbles, especially for the semi-active surfaces. Overall, to realize the decades-long dream of covering the entire vessel with SHPo surfaces to reduce energy consumption or increase speed, much work still needs to be done.